GEOMETRY AND KINEMATICS OF THE SOUTH LEADER FAULT; INSIGHTS FROM THE 2016 MW 7.8 KAIKŌURA EARTHQUAKE

A thesis submitted in partial fulfilment of the requirements for the

Degree

of Master of Science in Geology

in the University of Canterbury

by Natalie T. Hyland-Brook

University of Canterbury

June, 2018

ABSTRACT

The Leader Fault was one of at least 17 faults that ruptured the ground surface across the northeastern South Island of New Zealand during the Mw 7.8 2016 Kaikōura Earthquake. The southern ~6 km of the Leader Fault, here referred to as the South Leader Fault (SLF), ruptured the North Canterbury (tectonic) Domain and is the primary focus of this study. The main objective of the thesis is to understand the key factors that contributed to the geometry and kinematics of the 2016 SLF rupture and its intersection with The Humps Fault (HF).

This thesis employs a combination of techniques to achieve the primary objective, including detailed mapping of the bedrock geology, geomorphology and 2016 rupture, measurement of 2016 ground surface displacements, kinematic analysis of slip vectors from the earthquake, and logging of a single natural exposure across a 2016 rupture that was treated as a paleoseismic trench. The resulting datasets were collected in the field, from terrestrial LiDAR and InSAR imagery, and from historical (pre-earthquake) aerial photographs for a ~11 km^2 study area.

Surface ruptures in the study area are a miniature version of the entire rupture from the earthquake; they are geometrically and kinematically complex, with many individual and discontinuous segments of varying orientations and slip senses which are distributed across a zone up to ~3.5 km wide. Despite this variability, three main groups of ruptures have been identified. These are: 1) NE-SW striking, shallow to moderate dipping (25-45°W) faults that are approximately parallel to Cenozoic bedding with mainly reverse dip-slip and, and for the purposes of this thesis, are considered to be part of the SLF. 2) N-S striking, steeply dipping (~85°E) oblique sinistral faults that are up to the west and part of the SLF. 3) E-NE striking, moderate to steeply dipping (45-68°N) dextral reverse faults which are part of the HF. Bedding-parallel faults are interpreted to be flexural slip structures formed during folding of the near-surface Cenozoic strata, while the steeply dipping SLF ruptured a pre-existing bedrock fault which has little topographic expression. Groups 1 and 2 faults were both locally used for gravitational failure during the earthquake. Despite this non-tectonic fault movement, the slip vectors for faults that ruptured during the

earthquake are broadly consistent with NCD tectonics and the regional ~100-120° trend of the principal horizontal stress/strain axes.

Previous earthquake activity on the SLF is required by its displacement of Cenozoic formations but Late Quaternary slip on the fault prior to 2016 is neither supported by pre-existing fault scarps nor by changes in topography across the fault. By contrast, at least two earthquakes (including 2016) appear to have ruptured the HF from the mid Holocene, consistent with recurrence intervals of no more than ~7 kyr, and with preliminary observations from trenches on the fault farther to the west. The disparity in paleoearthquake records of the two faults suggests that they typically do not rupture together, thus it is concluded that the HF-SLF rupture pattern observed in the Kaikōura Earthquake rarely occurs in a single earthquake.

ACKNOWLEDMENTS

Many people helped make this project possible. First and foremost, I would like to profusely thank and acknowledge the Kelly Family of Woodchester Station, particularly David and Rebecca. Without your cooperation, this research would not have been possible; thank you for welcoming me (and so many others students and scientists) on to your land in good faith during a very trying and difficult time. As a family, you embody the definition of resilience.

Thank you to EQC, who funded this research via the EQC Capability Grant, and to Mason Trust for additional funding for field work. Thank you to GNS for the use of terrestrial LiDAR and to Ian Hamling for liberally sharing his InSAR data. These avenues have significantly aided my research.

The UC geological technical staff administered two departmental shifts this year, while simultaneously helping us with research. Big ups to Rob Spiers for generally just being the man, Sacha Baldwin for logistics, Matt Cockroft for drone wizardry and teaching me how to process GPS data, and Anekant Wandres for the photogrammetry and model of the Leader River.

Fieldwork can be hard if you are on your own for prolonged periods, and even more so if you are pregnant. Thank you to Dr. Paul Ashwell, Andrea Barrier, Sam Davidson, Tom Brough, James Smith, Mark Gray, Tabitha Bushell, Sarah Smithies and Dr. Kate Pedley for support and company on my many field outings.

Special shout out to all my fellow MSc. comrades of 2018 (particularly my office mates Kristie-Lee Thomas and Gabby Watson); thank you for all the commiseration, comradery, and support you have given me these past two years. Thank you for helping to make them some of the best years of my life.

Sincere thanks and gratitude to the top calibre advisory team/tectonics team. Thank you to: Prof Jarg. Pettinga, Dr. Tim Stahl for always making time for me when he had very little, and to my primary supervisor, Prof. Andy Nicol, a man who is as kind as he is cunning (just check his publishing record), for the opportunity, funding, and

guidance during this project. And to my other supervisors, thank you to Dr. Clark Fenton for all of the time, reassurance, laughs, and help given to me in the field/uni/ and with culinary decisions/recommendations, and to my friend and role-model, Dr. Narges Khajavi for teaching me how to process LiDAR, for all help in the field, and for encouraging me on the hard days.

Thank you to my heroes/ parents, who gave me the world, instilled the value of hard work, and supported me throughout each chapter of my life. You both have set a very high bar in terms of parenting. Most of all, thank you to my husband, Euan, for encouraging me to go back and get my MSc. /chase my dreams, and supporting me in every sense of the word while I do so. This thesis is for the baby I am carrying; you have been the greatest inspiration to work hardly and efficiently. Now I can (finally) nest in peace.

TABLE OF CONTENTS

LIST OF FIGURES

LIST OF TABLES

1.0 INTRODUCTION AND REVIEW OF CURRENT KNOWLEDGE

1.1 Background, Relevance of Study, and Research Objectives

At approximately three minutes past midnight on the night of November 14th, a complicated multi-fault rupture struck the north eastern South Island in what is now referred to as the Kaikōura Earthquake (Kaiser *et al.*, 2017). Two people were killed, 57 were injured, and it is estimated the total cost including insurance claims could be north of three billion $NZD (Bayer, 2016). The earthquake had a magnitude of Mw 7.8 and ruptured approximately 180 km across the plate boundary zone (Hamling *et al.*, 2017; Wang *et al.*, 2018). At the ground surface onshore, slip >~1m (horizontal or vertical) accrued on at least 17 active faults during the earthquake (Kearse *et al.*, 2018; Langridge *et al.,* 2018; Litchfield *et al.*, 2018; Nicol *et al.*, 2018; Fig. 1.1). These surface ruptures displayed differing orientations from north-northwest to east with displacements varying from strike-slip to reverse slip to normal slip. Faulting was predominantly dextral strike-slip and oblique reverse slip, the combination of which is reflected in the composite focal mechanism (USGS; https://earthquake.usgs.gov/earthquakes/eventpage/us1000778i#executive; Geonet; https://www.geonet.org.nz/earthquake/2016p858000; Fig 1.2). In addition to the faults that ruptured the ground surface, varying degrees of slip have been proposed for the subduction thrust and an offshore thrust fault (Clark *et al.*, 2017; Hamling *et al.*, 2017; Hollingsworth *et al.,* 2017; Wang *et al.,* 2017) although the role of these thrusts remains a point of debate.

While large, complex rupture processes are common for faults straddling subduction zones, the reasons for the rupture complexity of the Kaikōura event remain unclear. Fault geometries and co-seismic kinematics produced by large earthquakes provide a basis for understanding the properties of seismogenic faults and the factors that contribute to their co-rupture (Xu *et al.*, 2002; Fu *et al.*, 2005; Jiwen *et al.*, 2017). In the case of the Kaikōura earthquake, the results of these analyses may advance understanding of the current kinematic models of fault deformation across the complex plate boundary of the South Island (Nicol *et al.,* 2018). In addition, fault specific studies are paramount if we are to recognize and quantify seismic hazards in

the region of the Kaikōura earthquake. In the North Canterbury region, the seismic potential of individual faults had been recognized (Pettinga *et al.*, 2001; Barrell and Townsend, 2012; Litchfield *et al.*, 2014) however, many of the faults that ruptured were previously unknown or poorly defined. Therefore, seismic sources (i.e. faults) in the present seismic hazard model are incomplete, and in many cases, the potential for multi-fault rupture or slip on the subduction thrust not explicitly included.
The Leader Fault was one of the faults that ruptured the ground surface in the Kaikōura earthquake in the North Canterbury region (Fig. 1.1, 1.3 &1.4). The South Leader Fault (SLF) in the area south of the Leader River at Woodchester Station is the focus of the current thesis (Fig. 1.4). The SLF produced a highly irregular surface rupture pattern comprising multiple discontinuous traces (at the scale of resolution of the mapping). The SLF is further complicated in the northern part of the study area where it intersects The Humps Fault (HF). Parts of the SLF and the HF were previously included on existing geological maps (Rattenbury *et al.,* 2006) however, neither were mapped as active in the study area due to the apparent absence of pre-existing fault scarps. Therefore, no neotectonic or paleoseismic data (e.g., recurrence intervals, single event displacement or slip rate) were available for the fault prior to the 2016 earthquake. The lack of paleoseismic data on the SLF suggests that it is likely to be characterised by a low slip rate (e.g., <0.5 mm/yr) and long average recurrence interval (e.g., >5000 yr). Historically, a number of low slip rate faults worldwide (e.g. the Darfield earthquake, Quigley *et al.*, 2012; The Dasht-e-Bayaz earthquake, Tchalenko and Ambraseys, 1970; the El Asman Earthquake Philip and Meghraoui, 1983; The El Mayor Cucupah Earthquake, Fletcher *et al.*, 2016), resulted in complex surface rupture patterns which challenge the one-fault one-earthquake paradigm. Events that activate complex fault networks are capable of large rupture lengths and displacements (e.g., >100 km and 5 m, respectively), and are more difficult to interpret from the geological record than on individual ruptures of mature faults, such as the San Andreas fault or the Alpine fault (Sieh and Jahns, 1984; Yetton, 1998).

It is widely accepted that the deformation and geometry of earthquake ruptures are reflected in the surface morphology of the fault and the landscape that it displaces, and depend on the structure of the upper crust as well as the pre-existing tectonics (Jiwen *et al.,* 2017). To anticipate better the future earthquake behaviour of complex

fault networks, we need to understand processes that control the surface rupture geometries and slip distribution. The present MSc thesis describes the geometry and kinematics of the SLF together with the factors that influenced its complex rupture geometry and slip distribution. The data collected in this thesis from the SLF are among the first to characterize this newly recognized structure. This thesis has essentially been a year of post-earthquake reconnaissance, and the primary objective was to learn as much as possible about the 2016 surface ruptures of the SLF and its geological history. To achieve these overarching goals, a wide range of methods and data were employed, including:

- Bedrock/geological unit distribution with respect to fault traces,
- Detailed surface trace mapping,
- Horizontal and vertical displacement profiles along the SLF,
- Kinematic vector analyses where striation data were available,
- Interpretations of historic aerial photo imagery,
- A single, natural exposure that was logged and treated as a paleoseismic natural trench.

The resulting datasets were used to address a number of key questions including:

- What are the relationships between the 2016 surface rupture and bedrock faulting and bedding (Cenozoic and Mesozoic)?
- Does the interplay between geology, topography, and rupture geometry indicate whether the 2016 event is a typical rupture pattern for the SLF?
- Why was the deformation zone associated with the 2016 so wide and complex?
- How does the orientation of the surface ruptures affect displacement distributions during the 2016 event?
- What do the displacement variations reveal about the deformation along the SLF?
- How much of the displacement produced along the SLF in 2016 was tectonic, and how much was gravity driven?
- How do the slip vectors and strain axes for the 2016 event compare with regional stress/strain field?

- Is there evidence for prehistoric seismic events or geomorphological structures for the SLF and the HF in the study area, and if so, what do these observations indicate about the paleoseismic histories of these faults?

1.2 Kaikōura Earthquake

1.2.1 Overview

The Mw 7.8 Kaikōura Earthquake is the largest historical earthquake to have ruptured in the onshore of the northeast South Island (Clark *et al.*, 2017; Hamling *et al.*, 2017; Litchfield *et al.*, 2018). The surface faulting cannot be resolved by using a single model of strike-slip, reverse, or normal faulting mechanisms and is among the most complex surface ruptures documented in modern history (Hamling *et al.*, 2017; Wang *et al.*, 2018). The main shock occurred in the North Canterbury Domain (NCD) at a focal depth of 14.1 km and propagated to the NE for ~180 km (Fig 1.1).

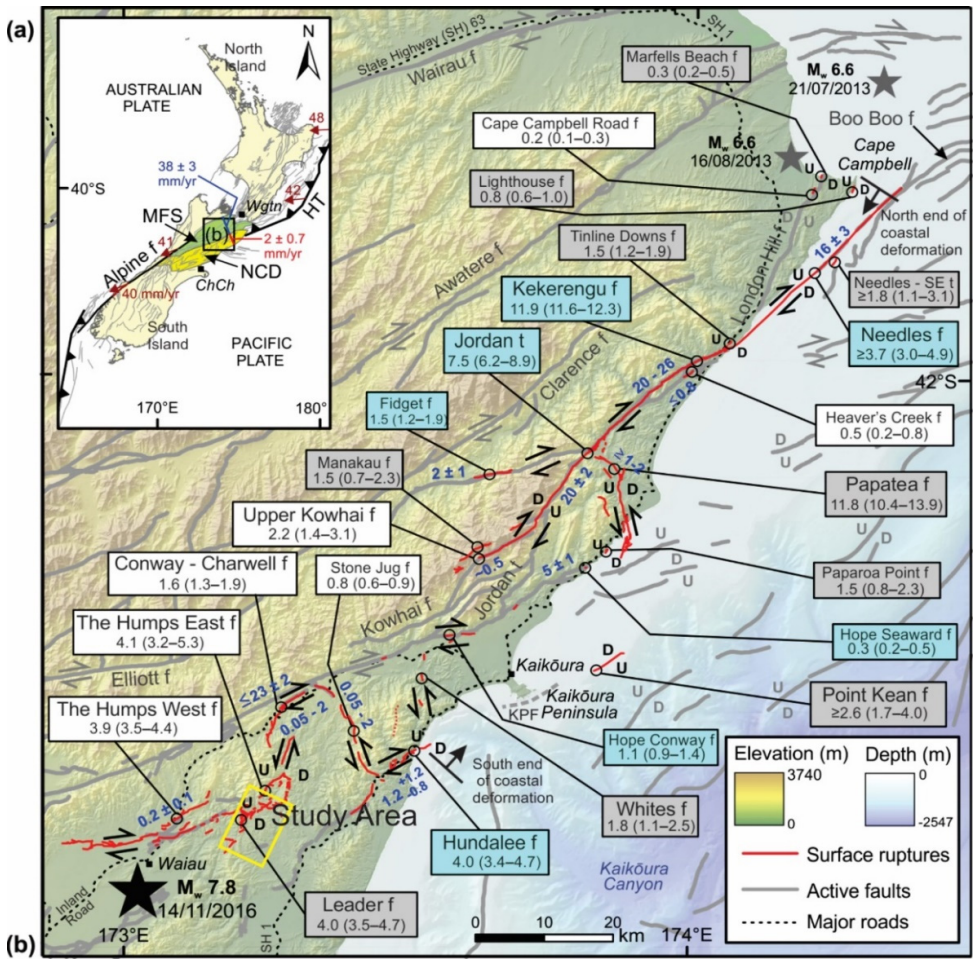

Figure 1.1: A: Overview of tectonic setting highlighted the area for the MFS and NCD (Litchfield *et al.*, 2014). B: Surface ruptures and their highest recorded displacements (m). Italicized faults indicate minor displacements. The study area is shown in the yellow box. Modified Figure after Litchfield *et al.*,(2018).

The earthquake initiated on the HF with an epicentre on the Emu Plains, 5km west of Waiau, and activated an intricate network of (a minimum of) 17 faults over six sub-events which propagated to the north-east and ruptured across two distinct seismotectonic domains; the Malborough Fault System (MFS), and the North Canterbury Domain (NCD) (Hamling *et al.*, 2017; Kaiser *et al.*, 2017; Litchfield *et al.,* 2018; Nicol *et al.*,2018). The ruptures that occurred in the MFS are referred to as the "northern ruptures" and faults that ruptured south of the Hope Fault in the NCD are called the "southern ruptures". The faults that ruptured had varying recurrence intervals, slip senses, surface displacements, orientations, and slip rates (Langridge *et al.,* 2018; Litchfield *et al.,* 2018; Kearse *et al.,* 2018; Nicol *et al.,* 2018). Of the 17 faults that ruptured the ground surface or seabed, five were considered inactive, or were unmapped entirely in geological records prior to the earthquake. Three of these faults are situated in the NCD and include the Leader, Stonejug and Whites faults. Incomplete information were available for the active fault lengths and paleoearthquake histories of the remaining faults that ruptured in this domain (see Nicol *et al.*, 2018).

It is perplexing that the main shock occurred on the HF, rather than the Hope Fault (the fastest slipping fault in the northeastern South Island), which is situated just 10 km north and accommodates up to 60% of the plate motion (Van Dissen and Yeats, 1991; Langridge *et al.*, 2016). Although a small segment of the Hope Fault exhibited negligible surface displacement, much higher amounts of surface displacement occurred on the unknown or less active faults to the south. In addition to significant displacement on the onshore faults (maximum of ~12 m on the Kekerengu; Fig. 1.1), field surveys, satellite geodesy, and LiDAR differencing revealed a maximum of 6.5 m of uplift along ~110 km of the Kaikōura coastline (Clark *et al.*, 2017), where ~4m crest-to-trough waves were observed (Bai *et al.*, 2017). The ruptures generated tsunamis that were recorded on tide gauges along the eastern coasts of both North and South islands, and in the Chatham Islands. The occurrence and spatial extent of coastal uplift and subsequent tsunamis may indicate slip on the subduction interface; however, the precise boundaries of slip on the subduction interface in 2016 are unclear and will be discussed briefly in section 1.3.1

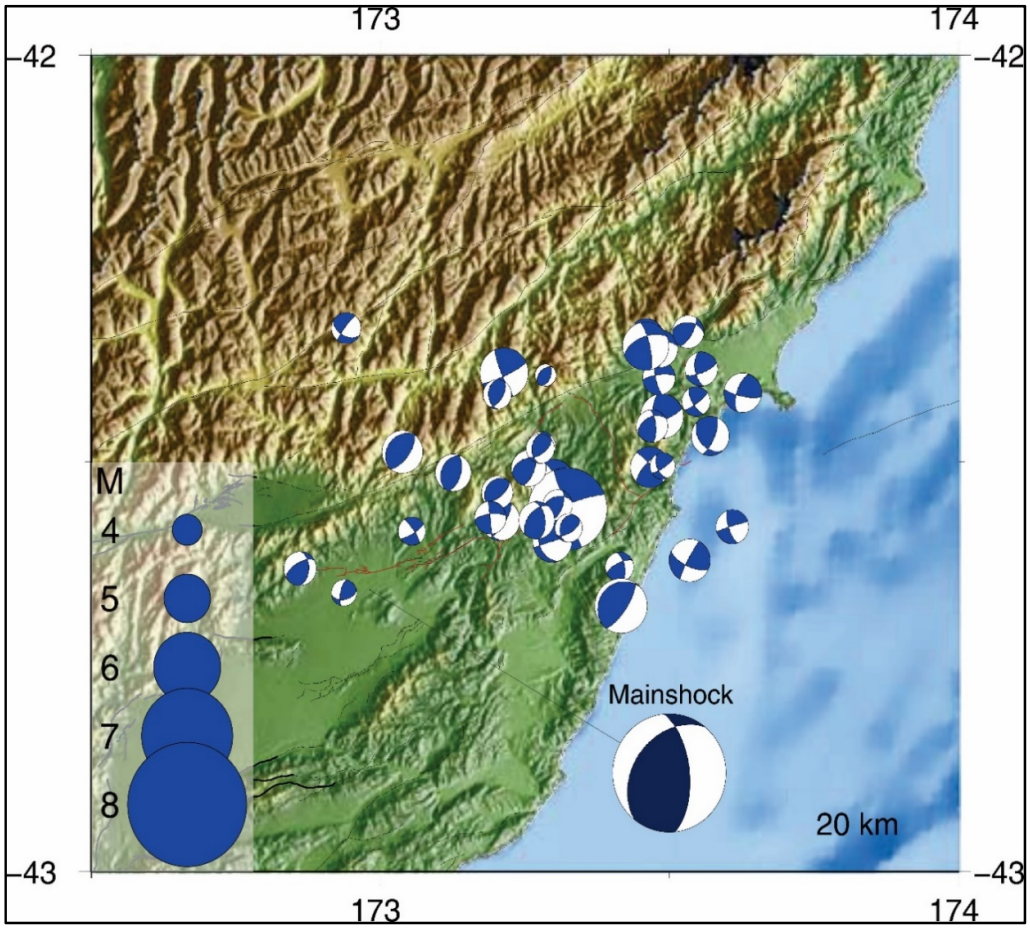

Figure 1.2: Automatically generated aftershocks from 14 November 2016- February 2017 and focal mechanisms from Geo-Net regional moment tensor solution catalogue. Modified figure from Nicol *et al.,* 2018

1.2.2 Northern Ruptures

The northern ruptures constitute a nearly continuous zone of deformation over a distance of 83 km (Kearse *et al.*, 2018) although locally, they exhibit step-over zones. The northern ruptures accrued the highest amount of slip (~12 m on the Kekerengu, 7 m on the Jordan Thrust, and ~7.4 m on the Papatea Fault; Kearse *et al.,* 2018; Litchfield *et al.,* 2018; Fig 1.1). The 12 m of dextral slip on the Kekerengu fault is among the five largest surface displacements ever documented (Sieh, 1978; Baljinnyam, 1993; Lin *et al.*, 2001; Rodgers and Little, 2006; Lin and Nishikawa, 2007; Wesnousky, 2008). The Kekerengu Fault ruptured its entire onshore length, as well as 30 km on its offshore component called the Needles Fault (Kearse *et al.*, 2018; Litchfield *et al.*, 2018). The Jordan Thrust and Upper Kowhai Faults also ruptured 30 km lengths on shore. The Kekerengu, Jordan Thrust, and Upper Kowhai faults displayed predominantly dextral strike-slip with subordinate reverse (Kekerengu and

Needles) or normal (Jordan Thrust and Upper Kowhai) components (Kearse *et al.*, 2018; Litchfield *et al.,* 2018). High displacements were also observed on the N-NW striking Papatea Faults and NE striking Fidget faults (Kearse *et al.*, 2018; Litchfield *et al.,* 2018), and subsidiary displacements occurred on short sections of the Marfells Beach, Cape Campbell, Lighthouse, Heaver's Creek, and the Tinline Downs faults (Litchfield *et al.,* 2018). Prior to the Kaikōura Earthquake, the Jordan Thrust, Kekerengu, and Needles fault were fully mapped and recognized as active structures, however the Upper Kowhai fault was mapped as possibly active by Van Dissen and Yeats (1991), and the Papatea Fault was not mapped as active.

1.2.3 Southern Ruptures

Unlike the relatively continuous and linear geometry of the northern ruptures, the southern ruptures are complex, comprising many short (< 4 km) and discontinuous traces that form zones of faulting up to 3.5 km wide (Litchfield *et al.,* 2018; Nicol *et al.,* 2018). Despite the discontinuous form of ruptures in the southern zone, The Humps, Conway-Charwell and Hundalee faults, with their general E-NE strikes, are hard-linked by the NNW-NNE striking Leader and Strone Jug faults to form a fully connected system (Nicol *et al.,* 2018). These faults form a complex array of both dextral and sinistral strike-slip and reverse or thrust faults that accommodated net surface displacements of ~ 5.5 m in the 2016 event (Stirling *et al.*, 2017; Nicol *et al.*, 2018; Litchfield *et al.,* 2018). The focal mechanisms presented in figure 1.2 reflect the variety of slip senses across the NCD. Dextral faults generally strike E-ENE (e.g., the HF western section, Conway Charwell Fault, and parts of the Hundalee Fault), oblique reverse faults strike NE (e.g., the HF eastern section and parts of the Hundalee Fault) and sinistral faults strike N-NW (e.g., Leader and Stone Jug faults) (Nicol *et al.*, 2018).

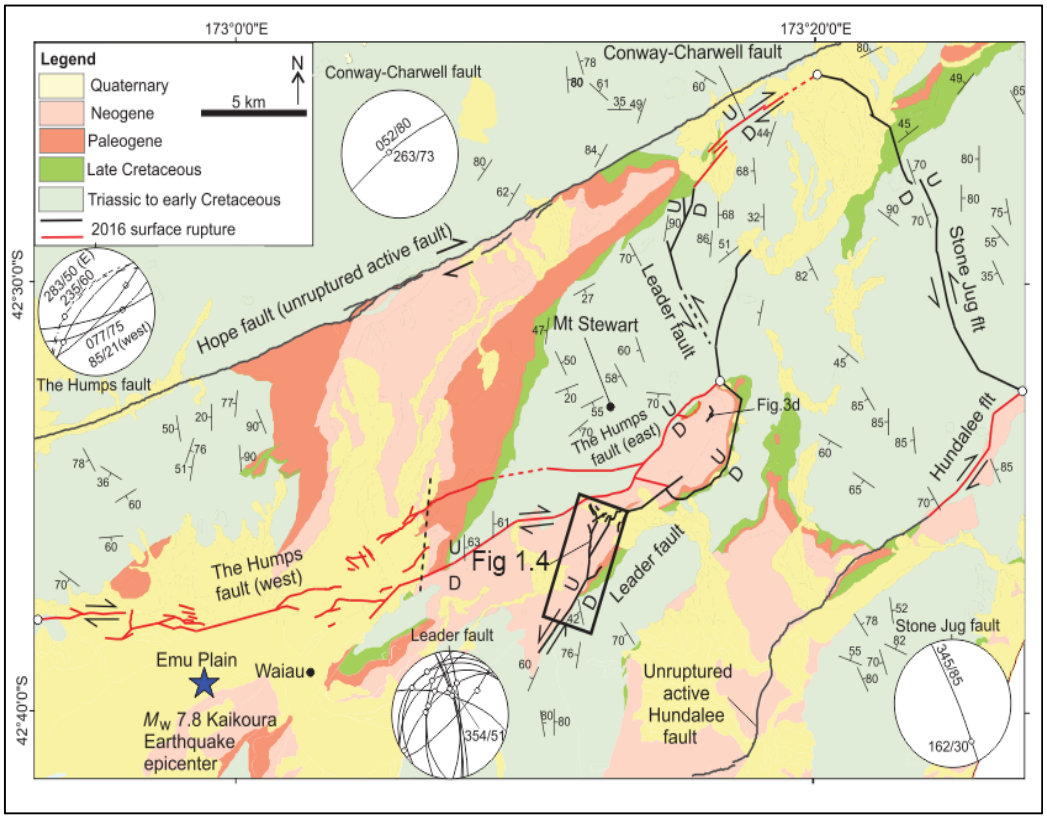

Figure 1.3: Fault trace and geologic map of the southern ruptures where the study area boxed in black. Original Figure from Nicol *et al. (*2018).

The Humps Fault (HF)

The epicentre of the Kaikōura Earthquake initiated 2.5 km south of the township of Waiau on the western segment of the HF on the Emu Plains (Nicol *et al.*, 2018, Fig 1.3). Prior to the earthquake, the HF was recognized as an active structure 2 km east of Waiau, and "likely active" further east (Barrell and Townsend, 2012) but was not previously mapped to the west of Waiau. The HF strikes E-NE and extends 36 km from a free tip to an intersection with the Leader Fault at the base of the Mt. Stewart Range (Fig.1.3;1.4). During the Kaikōura Earthquake, it accommodated predominantly dextral slip with varying thrust/reverse and normal components, which were accommodated by pop-ups and pull apart structures between *en echelon* fault segments. As the HF approaches the SLF towards the Mt. Stewart Range, it changes slip sense from predominantly dextral to mainly oblique slip with dextral and reverse components (further discussed in Chapters 4 and 5). Maximum displacements observed on The Humps Fault are ~ 4 m dextral, and ~ 3.5 m vertical (Nicol et al, 2018).

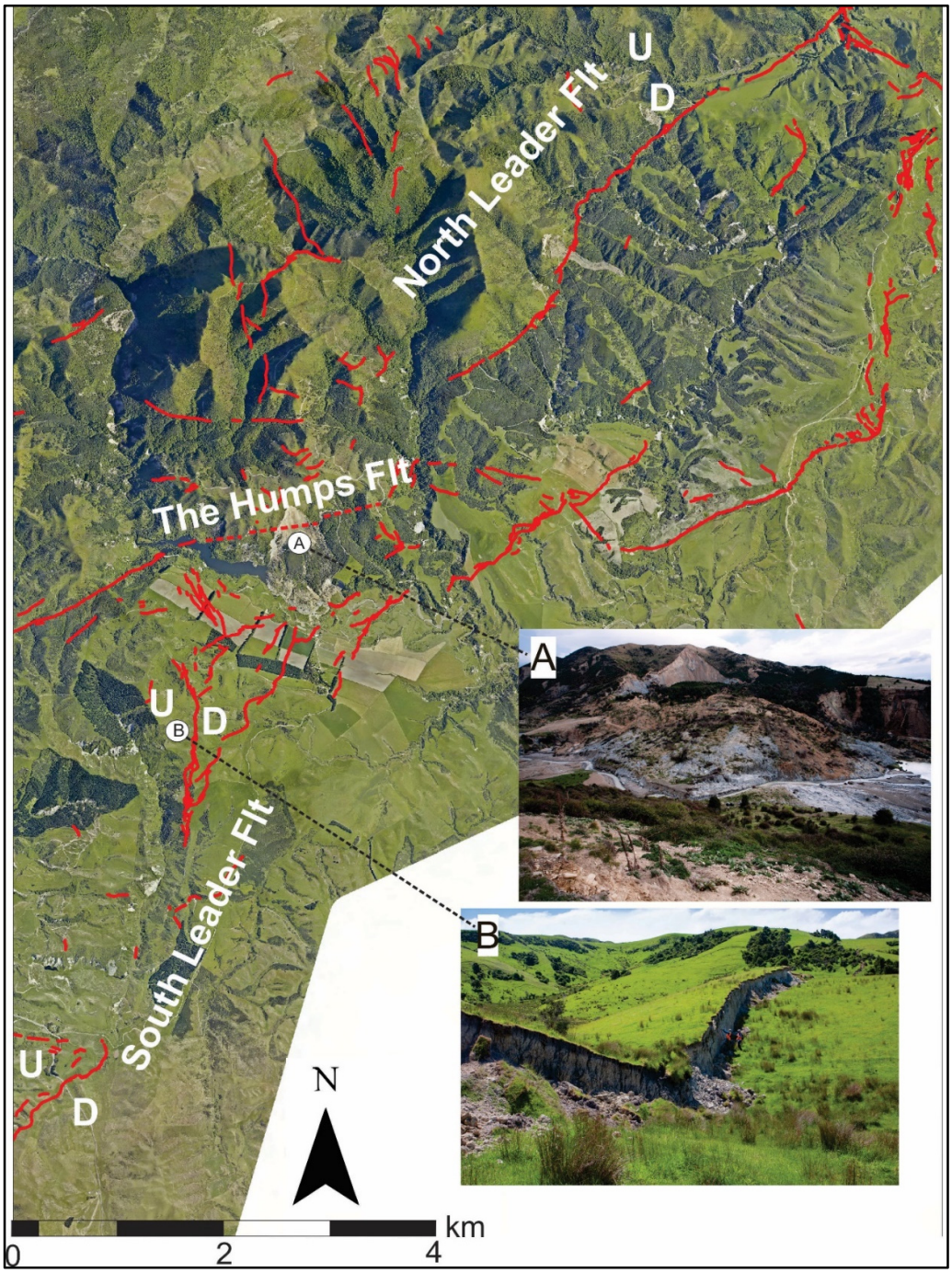

Figure 1.4: Annotated orthophoto of the study area and the immediate surrounding regions. The focus of the current thesis is along the 6km from the lower left hand fault trace to the Leader Landslide (marked A). B indicates the location of the 3m scarp of The Waiau Wall. U and D indicate upthrown and downthrown sides of each fault. Both photos taken by Dr. Kate Pedley.

Where the HF intersects the SLF in the study area, traces are discontinuous, and most often dip 50-68° NW approximately sub-parallel to bedding. Figure 1.4A depits a picture of the Leader Landslide, where the HF defines the boundary between the

basement Torlesse and Greta Siltstone Formation. At this locations, the Torlesse has been thrusted over the Miocene Greta Siltstone

The Leader Fault

The Leader Fault is a NW-NNE trending oblique sinistral fault that links the HF and Conway-Charwell faults. The end to end strike length of the Leader Fault is approximately 22 km from a free tip in the south and an intersection with the Conway-Charwell fault in the north (Nicol *et al.*, 2018). Rupture traces on the Leader Fault are discontinuous, vary in strike, and form a zone up to 3.5 km wide (Fig 1.4). Presently, little is known about the Leader Fault north of its intersection with the NE termination of the HF (Fig. 1.4, here referred to the northern segment), due in part to the presence of remote and mountainous topography. North of the intersection with the HF, the Leader Fault is contained entirely within the Torlesse basement, where it appears to strike sub-parallel to bedding (Nicol *et al.*, 2018). LiDAR (Light detection and Ranging) mapping indicates that vertical offset of the northern segment of the Leader Fault is up to ~ 4 m (Nicol *et al.*, 2018). This segment of the fault was unmapped before the Kaikōura Earthquake, despite the presence of the range-front. This thesis focuses on ~6km of the southern segment of the Leader Fault (which is here referred to as the South Leader Fault, SLF) at Woodchester Station (Fig 1.4). In the study area, the SLF comprises a zone of up to 3.5 km wide at the intersection with the HF. The SLF comprises a series of broadly *en echelon* NE-striking thrusts (dips 35-45°) linked by near-vertical N-S striking faults which are primarily contained within, or bound, Cretaceous-Cenozoic strata and dip steeply (~85°). Fault traces formed during the surface rupture are discontinuous with predominant upthrow to the west of up to ~3.5 m. Further details of the geometries and displacements of 2016 ruptures within the SLF are presented in Chapters 3-5 of this thesis.

In addition to complex fault rupture geometries, Woodchester Station experienced at least 42 co-seismic landslides or rockfalls of varying sizes (Smith, 2017). Often, faults and landslides share a failure plane and/or are co-located (e.g., the Leader Landslide). The Leader Landslide is the largest slope failure in the study area with an aerial extent of 600,000 m^2 (Gray, 2017). The Leader Landslide headwall scarp is approximately 400 m wide and up to 200 m high (Fig. 1.4A), with landslide debris obstructing the flow of the Leader River, creating a landslide dam and lake which

remains to the present day. The influence of gravity on fault ruptures is discussed in Chapter 4, and the methodology for differentiating gravitational and tectonic fault slip presented in Chapter 2.

Prior to the Kaikōura Earthquake, the SLF was partly mapped as a single, inactive fault surface on the basis of an inferred faulted contact between the Miocene Greta (Siltstone) Formation and Mesozoic Torlesse basement along the Leader Road at the southernmost extent of the field area (Warren, 1995; Rattenbury *et al.,* 2006). However, many of the N-S striking structures in Figure 1.4 (which include The Waiau Wall) were not included in geological maps prior to the 2016 event (see Chapter 3).

1.3 Regional Tectonic Setting

The South Island of New Zealand sits astride the boundary between the Pacific and Australian plates which are obliquely converging at 39-50 mm/yr in this region (Beavan *et al.*, 2002; Demets *et al.,* 2010; Fig. 1.1a). In central New Zealand, the plate boundary transitions from Pacific plate subduction along the Hikurangi margin beneath the North Island to continental collision along the dextral transpressive Alpine Fault in the South Island (e.g., Walcott, 1998; Beavan and Haines, 2001; Wallace *et al.*, 2012). This transition and the associated transfer of relative plate motion is facilitated in the northern South Island by the predominately strike-slip faults of the Malborough Fault System (MFS) (Wallace *et al.*, 2012). Although the geometries, kinematics and slip rates of the main faults within the MFS are well documented, the southern extent of the subduction thrust and its relations with the upper-plate faults are not (Eberhart-Phillips and Bannister, 2010).

The MFS comprises dextral strike-slip faults which accommodate the majority (>80%) of the relative plate motion (Wallace *et al.,* 2012; Litchfield *et al.*, 2014). The four main strike-slip faults in the MFS are the Hope Fault (13-27 mm/year), the Clarence Fault (~4 mm/yr), the Awatere Fault (4-8mm/yr) and the Wairau Fault (~4 mm/yr; Wallace *et al.*, 2007), and strike approximately parallel to the Australia/Pacific relative plate motion vector (Wallace *et al.*, 2012). Despite these high slip rates, none of the main faults of the MFS ruptured during the Kaikōura Earthquake with surface displacements >1.5 m (Litchfield *et al.,* 2018); although preliminary field observations suggest that the eastern Hope Fault may accommodate

more displacement than first thought (Khajavi and Pettinga, pers comm., 2017). Approaching the east coast in Marlborough, displacement is transferred from the Hope Fault onto the Kekerengu Fault via the Jordan Thrust (Van Dissen and Yeats, 1991) while further east offshore displacement may be transferred onto reverse faults within the accretionary complex (Wallace *et al.,* 2012). The north-eastern extent of the MFS and degree to which the Wairau, Awatere, Hope, and Clarence faults connect across the Cook Strait with regional strike slip faults in the lower North Island has not been resolved (Wallace *et al.*, 2007).

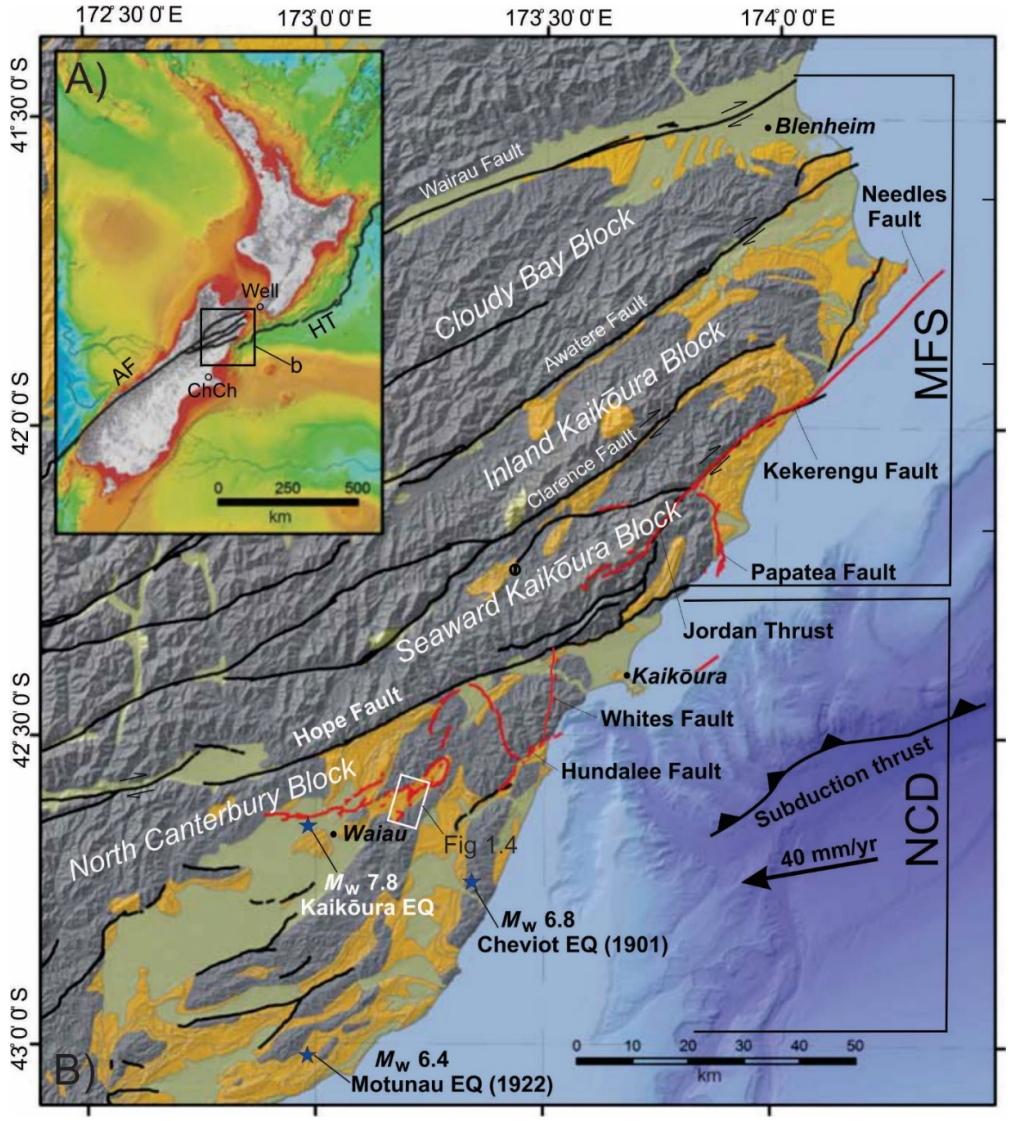

Figure 1.5: Map displaying the block settings between the major faults of the MFS (faults shown in black) with those that ruptured in the 2016 event (red). A) New Zealand plate boundary where AF, Alpine Fault; ChCch; Christchurch, HT; Hikurangi trough; Well, Wellington. B) Faults that ruptures in 2016 with respect to geology after Rattenbury *et al., (*2006), where Torlesse basement is shown in gray, Cretaceous-Cenozoic strata is shown in orange, and Quaternary deposits are shown in green. Modified figure after Nicol *et al.* (2018). The white box indicates the current study area.

The North Canterbury (tectonic) Domain (NCD) is bound by the Hope Fault to the north and the Canterbury Plains to the south (Fig 1.5). The NCD straddles the transition from oblique subduction along the Hikurangi margin to oblique continental convergence in the central South Island (Walcott, 1978; Nicol and Wise, 1992; Reyners and Cowan, 1993; Barnes, 1996). The region accommodates transpression on largely NE striking oblique reverse faults and associated asymmetric folds which collectively accommodate about 2-4 mm/yr of NW-SE shortening (Nicol *et al.*, 1994; Barnes, 1996; Pettinga et al., 2001; Litchfield *et al.*, 2003). Faulting and folding has produced range and basin topography, with ranges mainly comprised of Mesozoic Torlesse basement, and the intervening basins of Pleistocene gravels and Cretaceous-Cenozoic strata.

Prior to the 2016 earthquake, no strike slip faults had been identified in the NCD.

1.3.1. A disputed Subduction interface

At present, there is no strong consensus whether the Kaikōura Earthquake produced slip on a continental thrust in the accretionary prism, or on the subduction interface (e.g., Bai *et al.,* 2017; Clark *et al.*, 2017; Furlong and Herman, 2017; Wang *et al.,* 2018). The seismological and tsunami models indicate a significant portion of the slip in the 2016 earthquake occurred on the subduction interface (Duputel and Rivera, 2017; Hollingsworth *et al.,* 2017; Wang *et al.*, 2018) whereas the geodetic data and field observations favour a model of shallow crustal faulting as the predominant mechanism for the Kaikōura Earthquake (Clark *et al.,* 2017; Hamling *et al.,* 2017).

Subduction of the Pacific plate could be occurring beneath the study area. Seismicity in the down-going Pacific plate and velocity data indicate that the subduction interface extends to at least to the latitude of the study area (i.e. ~42.4° S) near where thick continental crust of the Chatham Rise intersects the margin (Anderson and Webb, 1994; Barnes *et al.*, 1998; Eberhart-Phillips and Bannister, 2010; Wallace *et al.*, 2012; Wlliams *et al.,* 2013). This area also coincides with a reversal of reverse fault dip directions from NW in the north to SE in the south; this reverse approximately coincides with the location of the HF. The north-eastward verging folds and thrusts are considered to be part of the Hikurangi subduction complex which extends into Marlborough and North Canterbury (Nicol, 1991; Nicol *et al.,* 1994;

Barnes, 1996). However, the northwest dipping top of the Pacific plate can be identified up to a further 70 km south of Kaikōura into North Canterbury (Reyners and Cowan, 1993), although it seems unlikely that slip on the interface is occurring this far south.

While the precise location of the plate interface beneath North Canterbury cannot be constrained precisely, it is certain that the Kaikōura Earthquake ruptured two distinct seismogenic domains (the MFS and NCD) at or near the subduction interface (Litchfield *et al*., 2018). The resulting complicated geometry and array of faults in the upper plate may in part reflect this unique position astride the plate boundary and the proximity of these faults to the subduction thrust.

1.4 Thesis Organization

This thesis contains 6 chapters and appendices A, B, C, D, E, and F. The key questions outlined for the thesis earlier in this chapter are examined in Chapters 3-5. Chapter 2 presents the methods and data together with their uncertainties and Chapter 6 presents the conclusions of this research. Detailed contents for each chapter are provided below.

Chapter 1 presents a brief overview of the Kaikōura Earthquake and background of the study, why fault-specific studies along the SLF are valuable, and the wider context of plate boundary and North Canterbury tectonics.

Chapter 2 describes the data and methods utilised for Chapters 3, 4, and 5 of the thesis, and the associated uncertainties.

Chapter 3 explores the geology of the region enclosing the SLF and the relationship that the fault ruptures have to locations and geometries of pre-existing faults and bedding planes. Previous studies and nomenclature of geological units are also presented. The observations and interpretations are conditioned with regional observations in the North Canterbury region. The chapter considers surface (geological and fault ruptures maps) and sub-surface information (interpreted cross-sections) for the SLF.

Chapter 4 presents kinematic observations from the SLF, including vertical and lateral displacements and striation data for the 2016 earthquake. Slip vectors and

strain axes are developed from the displacements and striation data, and are compared with regional trends from previous studies in North Canterbury.

Chapter 5 presents the results from logging a natural trench exposure along the HF in the Leader River in an attempt to learn more about the faults paleoseismic history. The results of the trench are compared to other ongoing trenching observations in the western segment of the HF. Historical aerial photos are also examined in an attempt to determine whether pre-existing fault scarps existed in the study area prior to the 2016 event.

Chapter 6 summarizes all the key findings from each of the chapters, and explores areas for future work.

Appendix A contain a map of townships in the surrounding area,

Appendix B contains the master spreadsheet used to make displacement graphs,

Appendix C contains the spreadsheet provided by Andy Nicol and Narges Khajavi to calculate rakes where fault orientation and horizontal and vertical displacement is known,

Appendix D contains the raw trench log,

Appendix E contains the original OSL dating lab report from Victoria University, and,

Appendix F contains the drone accuracy and spec report.

The text and Figures have been prepared as a thesis document (rather than a series of manuscripts), although it is hoped that components of the work may form the basis for a future publication. Elements of the present thesis have already been published in Nicol *et al.* (2018) which I contributed to as a co-author.

2.0 METHODS

2.1 Introduction

The key questions for this study outlined in Chapter 1 require examination of the slip distribution and geometries of the rupture traces, mapping of the bedrock stratigraphy and faulting (and their spatial relationships to the surface ruptures), and the characterisation of paleoseismic histories of faults in the field area. A broad array of methods and techniques were required to collect the data used to describe the geometries and kinematics of the surface ruptures and to constrain their prehistoric displacement histories.

Over the last 10 years there have been significant advances in types of data available for analysing coseismic displacement including, interferometric synthetic aperture radar (InSAR), light detection and ranging (LiDAR), and high-resolution satellite data. However, there remains significant value in field-based investigations (particularly where fault displacements are low, for example < 1 m). The majority of the data collected for this thesis was done so directly from the field, with the aid of hand-held GPS instruments that were subsequently uploaded onto an active database in ArcMap. In the following sections, the methodologies used to collect and analize the data presented in Chapter 3-5 of this thesis are described.

2.2 Field Procedures

Fault-trace, displacement, and geological mapping were completed over a 40-day period. Most these tasks were accomplished within 6 months of the earthquake, thus, most of the fault scarps were still clearly visible and had not been removed by land remediation works (Fig 2.2E). Following this initial more intense phase of fieldwork, sporadic field checks continued until January of 2018. In addition, paleoseismic trench logging and analyses were completed over a 9-day period over November-December 2017.

2.2.1 Fault rupture Trace Mapping

The surface ruptures during the 2016 earthquake are recorded in Figure 2.1. Fault scarp mapping and displacement measurements commenced in November 2016 days after the earthquake and for the fault ruptures south of the Hope Fault (excluding the Hundalee Fault), were primarily collected by a large group (~15 people) from the

University of Canterbury (including the author of this thesis). In the field area approximately half of the displacements and surface ruptures data used in this thesis were mapped during this initial phase of work.

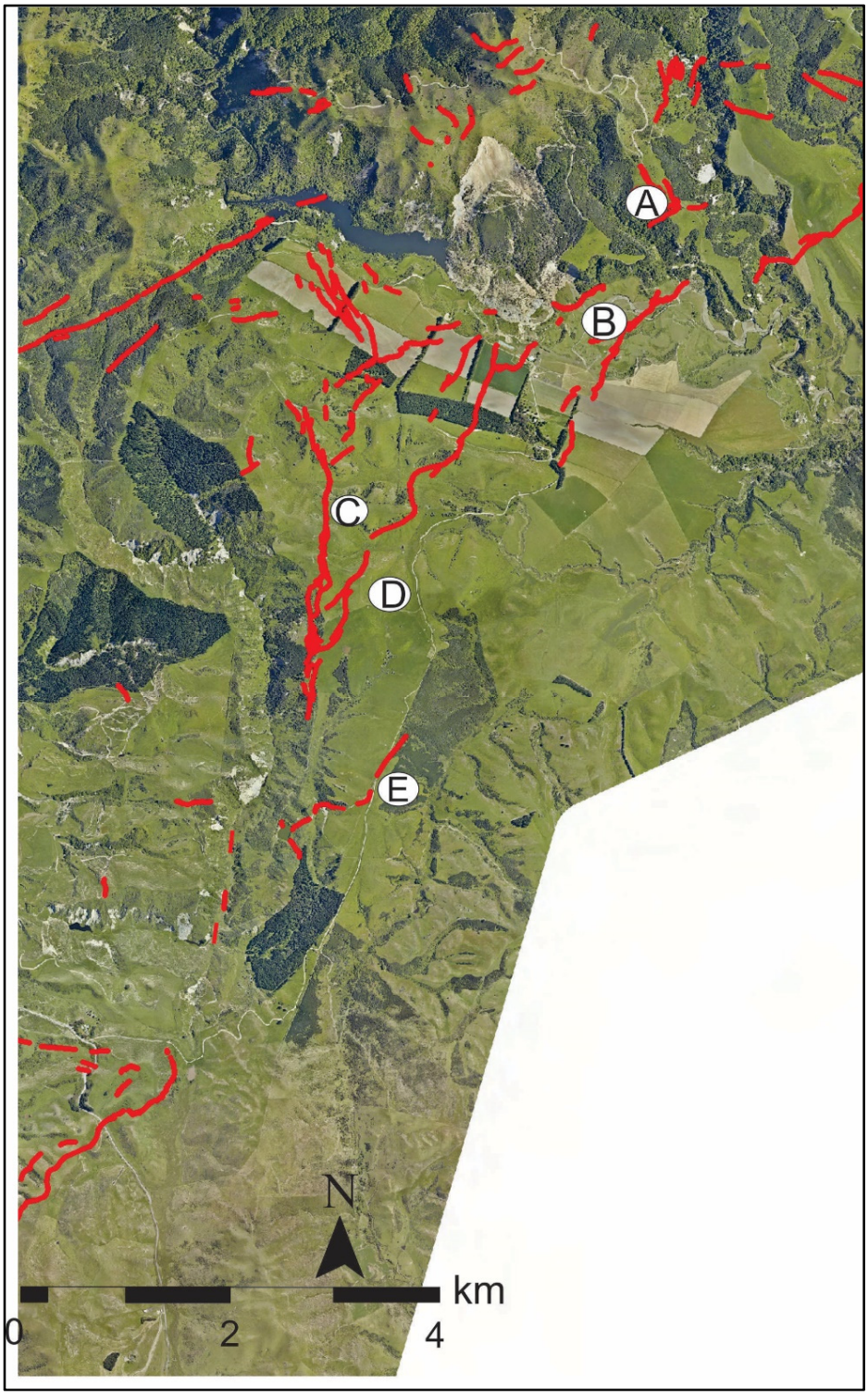

Figure 2.1: Fault trace map where letters A-E correspond to locations in figure 2.2

These initial observations were rechecked and augmented as new data in the field were collected. Field-based mapping of fault traces and displacement measurements were accomplished in this thesis using post-earthquake LiDAR orthophotos and Google Earth imagery, tape measure, compass, and a Trimble GEOXH GeoExplorer 2008 series GPS unit. Fault trace mapping was conducted primarily using the hand-held GEOXH explorer. The hand-held GPS was adjusted to collect data at an elevation of 1.2 m above the ground surface, so it could be held approximately at hip-height during data acquisition. When it was receiving sufficient ephemerides (a minimum of four satellites), the hand-held GPS was held steadily recording latitude-longitude and altitude locations as the operator walked along the fault trace. When these circumstances were met, location accuracy ranged from 15-30 cm in X, Y and Z directions. Many fault scarps, fractures, and subsidiary structures were logged as they were found in the field. In some cases, fault ruptures initially missed in the field were later identified using LiDAR hillshade models. In these cases, the locations were noted in the LiDAR and subsequently they were subsequently surveyed in the field using the GEOXH unit.

Orientations of faults were measured as strike and dip, where strike reported the azimuth of the fault from 0-360°, and dip reported from 0-90° (Benson *et al.,* 2013; Coe, 2013). In a number of instances fault strike and dip were measured in the field from outcrops or using the 'v' pattern of traces as they crossed valleys (e.g., Leader Road fault in Chapters 3 and 4). In the case of the Quarry fault, described in Chapter 3 and 4, the strike and dip was calculated using three locations on the fault surface and the three-point problem technique which uses trigonometry to estimate the true strike and dip of a plane. The method for solving the orientations of planes using three-point problems is described by Benson *et al.* (2013).

2.2.2 Ground Displacement Measurements

At Woodchester Station, strike slip and vertical displacements were generally measured in the field using cultural features such as roads, farm tracks, fences, and drainage ditches that crossed the fault rupture at high angles (>60°; Fig. 2.2B). Each displacement value was measured multiple times (~3) using a tape measure and/or by surveying the displaced marker using the GPS. In both cases uncertainties on the measured displacements were ±15%. For the purposes of this study, field

measurements were all assigned a ±15% uncertainty which is assumed to be approximately equivalent to the 2σ values.

Figure 2.2: Photograph depicting fault measurement procedures. A) Example of a dextrally offset fence. In this scenario, one member stands where the fence is straight and directs another person to where they should stand if the fence were to continue in a straight segment. Offset in this area is approximately 1 m. B) Depicts a sinistrally offset fence where the scarp height is present as a roll ~0.6 m, and dextral offset is nearly the same. C) Fault scarp of The Waiau Wall, where the vertical displacement could be measured directly. D) Toe thrusts that intersect The Waiau Wall, where a fence has been displaced dextrally. E) and E') Display a scarp ~0.90 m that was quickly levelled following the 2016 event. Photos C-E' by Dr. Kate Pedley.

All displacement field measurements were subsequently uploaded to an ArcMap database and along-strike profiles plotted using an Excel spreadsheet, which is provided in appendix B.

Measurement of horizontal displacements of linear markers (e.g., fences or roads) typically required projection of the marker to the fault trace along a line parallel to the far field trend of the marker. These projections (and the associated displacement measurements) were more reproducible when twine or rope was used to extend the marker to the fault trace. Alternatively, (or in addition to in some cases) the GEOXH hand-held GPS was used to survey points along the linear marker, and these data were later used in ArcMap software to projected the marker to the fault scarp. For such measurements it was assumed that the marker used estimate the displacement was straight prior to the earthquake. In the two years before the 2016 event, most of the fences at the Woodchester Station were straightened or replaced, and provided high quality markers for strike-slip displacement during the November 2016 event (Rebecca Kelly, pers comm., 2017). These measurements were also assigned a 15% uncertainty. In limited examples, laterally offset streams, roads, or sheep tracks were visible on orthophotos and could be used to measure displacement (Fig 2.3). Where accessible, these measurements initially found on orthophotos were then measured in the field and also assigned a 10-15% uncertainty. This technique was used after scarps had experienced significant degradation, and as tracks and roads were repaired in the months following the 2016 event.

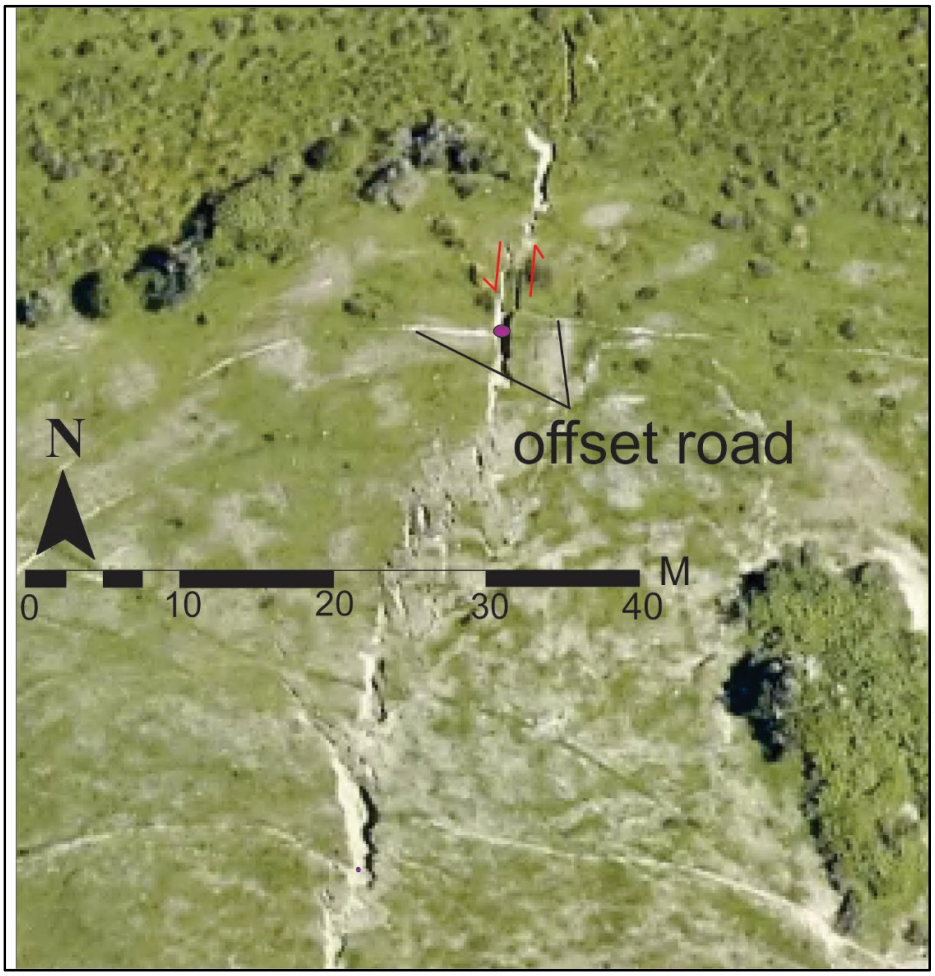

Figure 2.3: Annotated orthophoto of The Wall scarp which has offset a road ~2 m.

Vertical displacements (throw) were determined by measuring scarp heights in the field using a tape measure (Fig 2.2C). In other cases, they could be measured by creating topographical transects on the LiDAR model (Fig 2.4). The use of the LiDAR is discussed in more detail in sections 2.3 and 2.4. Digital elevation models (DEMs) data from LiDAR and uplift estimates from InSAR were used to estimate vertical displacements across fault scarps. These estimates were generated in ArcMap using topographical transects constructed across fault scarps (Fig. 2.4).

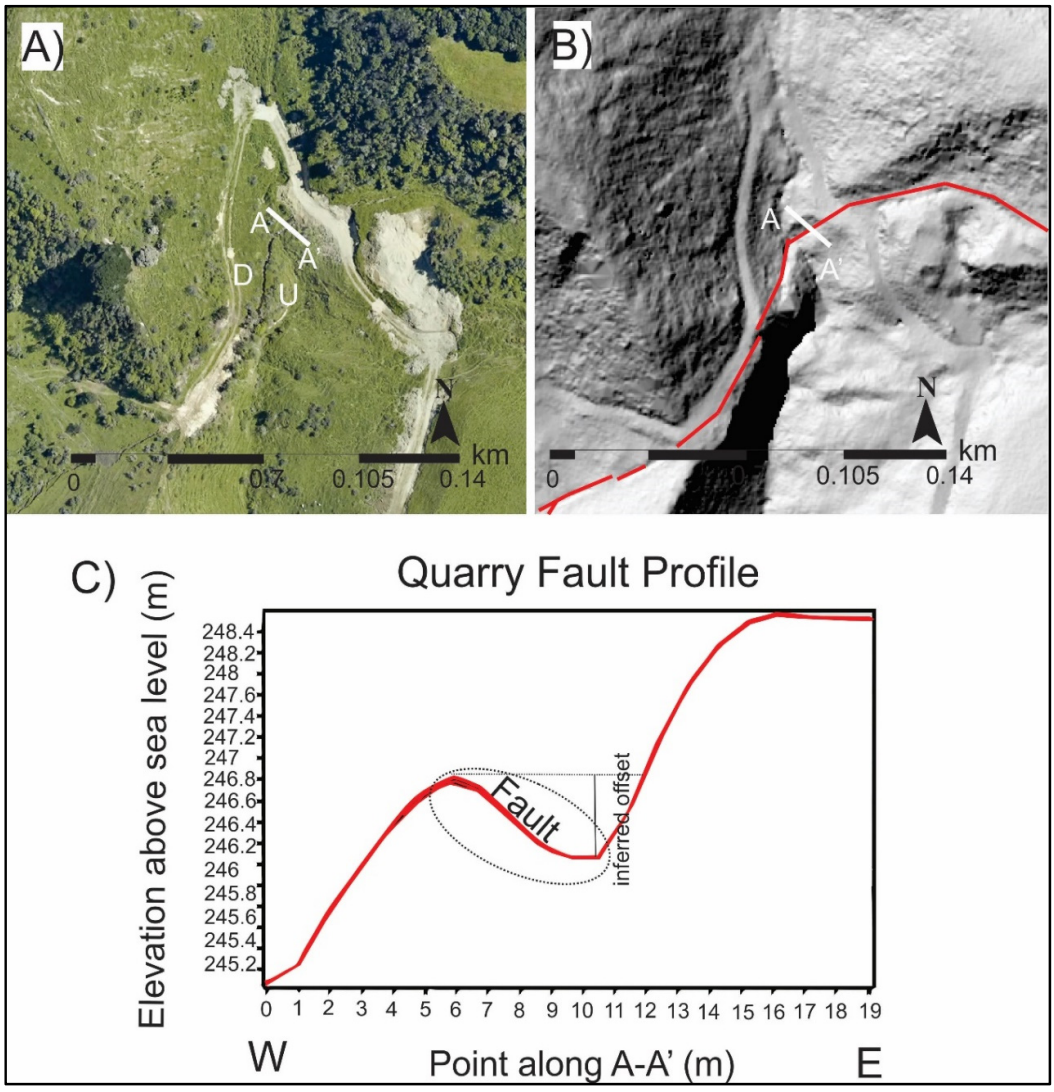

Figure 2.4: Topographic transect used to measure scarp height. A) Shows the orthophoto, where the scarp is visible without annotation. B) Shows the hillshade model with the fault marked in red. The Transect A-A' is plotted with elevation data from a DEM (0.25 m resolution). The discontinuity in the graph depicts the fault scarp, where the eastern side is up thrown. Inferred offset here is estimated to be 0.80 m, which is consistent with field-based measurements along this fault.

Vertical displacements as small as 20-30 cm were routinely measured using field and LiDAR data. These measurements were also assigned an uncertainty of ±15%. Fault scarp heights measured from LiDAR and in the field produced comparable results. Scarp-height measurements were more frequent than strike slip measurement, in large part because strike slip was more difficult to measure from LiDAR (than vertical). In addition to inferring vertical displacements, transects produced from the InSAR and LiDAR DEMs were plotted against each other to investigate a possible correlation between long-term uplift, as indicated by topography, and uplift during the Kaikōura

Earthquake. The method and reasoning for this comparison is described in Nicol *et al.,* (2018), and the results of this type of topographical analyses are discussed in Chapter 3.

2.2.4 Differentiation of tectonic vs gravitational forces

A primary challenge for interpreting the origin of fault kinematics in the field area (and in many other hill-dominated regions subject to surface rupture in 2016), was confidently differentiating tectonic faults from landslide or sackung failures along ridges. As indicated in Chapter 1, the field area and Woodchester Station are located on mostly hilly topography and underlain by weak grey mudstone of Miocene-Pleistocene age (Chapter 3). Due to the topography and the weak bedrock, ground shaking and surface rupture produced widespread slope failures. In some cases these slope failures utilised bedding surfaces and fault rupture surfaces from the 2016 event. In particular, the low-angle thrust faults discussed in Chapters 3 and 4 snake and curve through topography, especially around ridges, and in places appear to have accommodated down-slope dilation. Often, these faults shared a failure plane with landslide features (Fig. 2.5). The influence of gravity on the fault kinematics is further explored in Chapter 4 of this thesis.

The criteria for differentiating tectonic from gravitational movement is shown in the logic tree (Fig. 2.5C from Smith, 2017). In particular, tectonic faults are more continuous, linear, and have a consistent slip sense across hilly topography, whereas landslides may be more curved (often concave downslope), occur parallel to ridges, and often have graben, tension cracking, or antiscarp morphologies along hilltops, ridge lines, or headwall scarps (Smith, 2017). In addition, the sense of movement for landslides is consistent with downslope migration of near-surface stratigraphy. Where possible two of more of these criteria have been identified before are positively identified as gravitational slope failures.

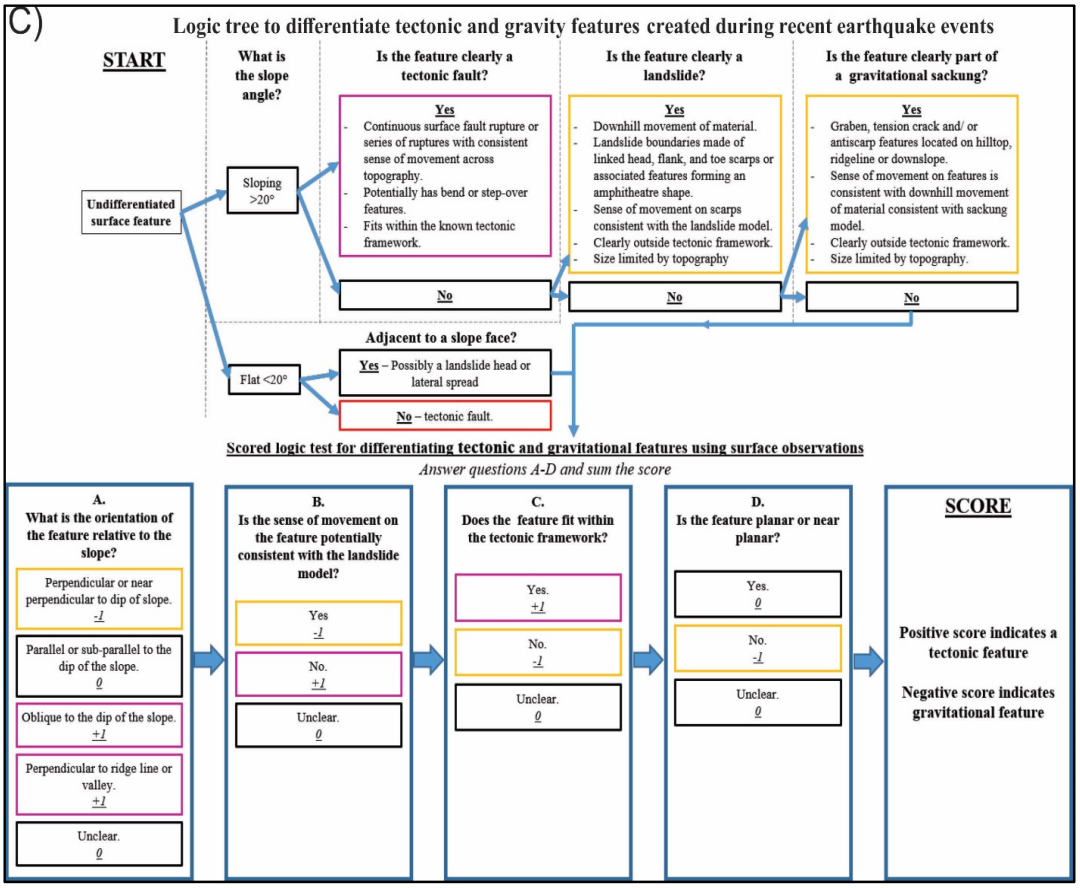

Figure 2.5: The interplay between faulting and hilly topography. A) Depicts sackung features and slumping with a likely fault which triggered movement, photo by Dr. Kate Pedley. B) Depicts a fault that is clearly thrusting uphill; but this example is unique, as many fault traces that triggered activity on a slope simply looked like landslide features. C) Depicts the reasoning employed behind the differentiation of tectonic and gravitation features taken from Smith (2017).

2.2.4 Striation Data

Striae were observed on three fault planes in the field area (Fig 3.6), which are described in Chapter 4 of this thesis. Where striae were visible in outcrops of the 2016 ruptures, their trend (from 0-360°) and plunge (0-90°) was measured directly from the fault scarp using a Silva compass as per the method described by Benson *et al.*, 2013 and Coe, 2013. These measurements were subsequently plotted on stereonets, and were used to inform slip vectors for the SLF presented in Chapter 4. In addition, some slip vectors were calculated using basic trigonometry in cases where the strike and dip of the fault, and vertical and horizontal displacement were known. These calculations were performed by Narges Khajavi and Andy Nicol and provided to the author in a spreadsheet, available in appendix C.

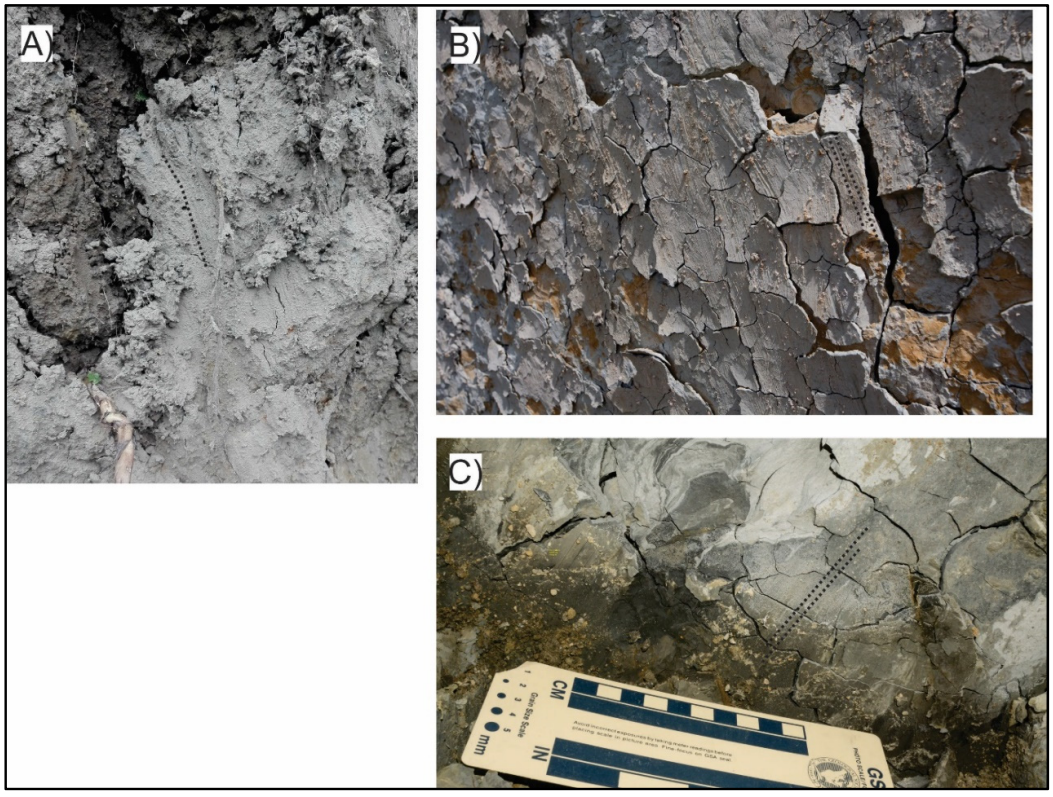

Figure 2.6: Compiled photographs showing the three locations where striae could be measured in the field. Select lineations have been traced in a dotted black line for the viewer to see, but most of the striae are visible to the naked eye in photographs. A) Striae found along the Quarry fault, B) Striae preserved well on The Waiau Wall, and C) Striae found on the Trench Fault.

Chapter 4 describes striae over The Wall surface at The Waiau Wall locality. At this locality, striae were well preserved along ~9 x 3 m of the fault surface which exposes a 'wall' of Greta Siltsotne Formation across rolling fields. Striations were mapped

over the fault surface using black plastic straws (stuck to the fault surface with blue tac) to define the local orientations of striae. The orientations of the straws were photographed and analysed to show a systematic change in the striation trends over the fault surface (also presented in Chapter 4).

2.2.5 Geological Mapping and Cross Section Construction

The field area is covered by rolling grasslands and trees. Therefore, geological exposures of bedrock were limited to stream beds, a man-made quarry, several road cuttings, and the Leader River bed. If exposures and bedding were present, the geological unit was recorded along with the orientation. Bedding was reported in the conventional form of strike and dip, and measured with a compass (Benson *et al.*, 2013; Coe, 2013). Stratigraphic nomenclature used in this thesis was adopted from Browne and Field (1985). The field mapping presented in this thesis was augmented by geological information from previous maps of Warren (1995) and Rattenbury *et al.* (2006).

Cross sections were prepared using the method described by Geiser and Boyer (1989). Due to the sparsity of outcrops, structural data was extrapolated to form inferred geological contacts. Bedding dips were adjusted to their true dip using the equations provided by Benson *et al., (*2013). The results, assumptions, and interpretations of these cross-sections are explored in Chapter 3.

2.3 LiDAR Analyses

LiDAR refers to a type of data acquisition where a manned aerial vehicle uses a pulsed laser light attached to a side of the aircraft and measures the altitude of the earth's surface through the returns of the laser. To determine the altitude of the ground surface time interval measurements of the laser returns are converted to distances and corrected with respect to the orientation of the aircraft. The resulting point clouds of X, Y, and Z data are used to generate 3D models of the land surface. Both digital terrain models (DTMs) and digital elevation models (DEMs) can be produced from a LiDAR dataset (Chu *et al.*, 2014).

Many recent publications on ground deformation during the Kaikōura Earthquake have used LiDAR data collected in the 2 months following the event (Clark *et al*., 2017; Hamling *et al.*, 2017; Kaiser *et al*., 2017; Kearse *et al*., 2018; Nicol *et al*., 2018;

Litchfield *et al.*, 2018). The LiDAR data used for this thesis was provided to the University of Canterbury by GNS science for the purposes of conducting fault rupture research. The interpretations from the LiDAR and orthophotos supported both the fault-trace mapping and the measurement of vertical displacements (see section 2.2.1 and 2.2.2). All LiDAR data processing were completed using ArcMap data management tools at the University of Canterbury. Raw LiDAR files were supplied as an LAS dataset, which was converted into a raster DEM with a 0.25 pixel size (this provided ground resolution accuracy to 0.25 m). The DEM was then used to create a hillshade model for a sun azimuth of 315°. The hillshade model was used to analyse the topography, and the DEM was used for topographic analyses (Fig. 2.4B).

2.4 InSAR Data

Satellite- based synthetic aperture radar (SAR) signal contains amplitude and phase information which can be used to determine the distance between the satellite and the ground. In circumstances where two SAR images are available for the same area it is possible to the estimate ground deformation in the time interval between acquisition of each image using InSAR (interferometric SAR; Hamling *el al,* 2017). InSAR uplift estimates for this study were derived from the Sentinel-1A ascending (03/11/2016-15/11/2016 and descending 05/09/2016-16/11/2016) azimuth and range offsets analysed by Hamling *et al.* (2017). For further information on the derivation of the InSAR uplift the reader is referred to the supplementary material associated with the Hamling *et al*. (2017) paper. The resulting uplift ranges from -0.5 to 3.5 m in the study are area (see map and analysis in Chapter 3).

2.5 Historical Aerial Imagery

Two sets of historical imagery were examined to investigate the form of the landscape before the 2016 earthquake. The primary reason for examining these photographs was to search for fault scarps formed during prehistoric earthquakes.

The first set of imagery was a set of ortho photographs produced by NZ Aerial Mapping in 1950 (run 1800/ 40-49 and run 1799/ 40-50) at a scale of ~1:17,000. These photographs were viewed as pairs with a stereoscope as per the method described by Allum, (1966). It is estimated that these photographs would permit fault scarps as little as 0.5-1 m in height could be resolved if present.

The second set of imagery was provided by Zekkos *et al.,* (2018) and comprises along-track stereo satellite imagery from March 23, 2015 that were used to produce surface models processed to a resolution of 0.25-0.5m (Zekkos *et al.,* 2018). Surface Extraction with TIN-based Search-space minimization (SETSM) methodology was created by (Noh and Howat, 2015; 2017) to transform over-lapping stereo swaths into terrestrial models, and were optimized using tools from the Ames Stereo Pipeline (Shean *et al.*, 2016). The set of imagery prepared by Zekkos *et al.* (2018) is estimated to resolve topographic scarps <0.5 m in height. Results for both sets of imagery are discussed in Chapter 5.

2.6 Drone Imagery

High resolution drone imagery provides the same benefits as LiDAR data and when combined with GPS surveying can be used to locate objects and generate DEMs with centimetre-scale resolution. Aerial photography was captured using an unmanned aerial vehicle (UAV) DGI Phantom 4Pro drone over the Leader River following the breach of the landslide lake in October and November of 2017. Using Agisoft PhotoScan, images were used to produce a DEM and 3D terrestrial model of the Leader River that is presented in Chapter 5. This model aided in the geomorphic mapping of the river following the breach of the landslide dam as well as the elevation difference of strath surface near the trench site (described in Chapter 5). The strath terrace was exposed where the fault plane was scoured which was thoroughly surveyed, and included a 223,929 point cloud which allowed an accuracy of 0.05-0.10cm. The specs of the DGI Phantom as well as the full AgiSoft Model report are provided in appendix F.

2.7 Trenching Procedures

Following breach of the landslide dam, the Leader River began to scour and carve through a fault rupture in the river bed (described in Chapter 5). Down-cutting produced a natural exposure of the fault plane and associated stratigraphy. Over a two-week period in November and December of 2017, this exposure was cleaned, logged, and the log was digitized to interpret the paleoseismic history.

A ten meter length of the natural exposure was cleaned using sedimentary scrapers, brushes, and brooms. Sections of the bedrock had not been properly exposed by the river, and were dug out using shovels. Subsequently, these walls were gridded into

one-meter squares along the depth and length of the trench wall using string and a level. Stratigraphic units, fissures, fault-related features, and large clast orientations were marked using a combination of spray paint or coloured tape that was nailed to the trench wall (flagging). Trench logging was completed on graph paper overlain with a mylar sheet and at a 1:10 scale. Many photographs were taken of the trench to provide an additional record of the trench characteristics. Raw trench logs were digitized using CorelDRAW X7, and are available in appendix D.

2.8 OSL Dating

As logging progressed, possible sample locations for optically stimulated luminesce (OSL) dating were noted and marked on the trench log. Initial interpretations of the trench were discussed and agreed upon by the advisory team for this thesis before the extraction of samples. Samples were taken by hammering stainless steel tubes into stratigraphic layers selected for dating. Before the tubes were hammered into the sediment horizon, the end that was not inserted into the ground was stuffed with paper and duct-taped over to ensure that the sample was not exposed to sunlight. Once the sample tubes were removed, they were bagged and labelled before they were sent off to the OSL dating lab at Victoria University of Wellington. Two samples were taken from the Leader River Trench (described in Chapter 5) and sent to the luminescence dating laboratory at Victoria University (VUW), Wellington, New Zealand. The full technical report provided by the VUW laboratory is available in appendix E.

The dating method for OSL is a form of geochronology that can measure the energy of released photons of Quaternary sediments. The calculated age record the last time feldspar grains were exposed to sunlight. Therefore, silt grains need to be exposed to sufficient sunlight during transport and deposition to reset the luminescence 'clock'. Age is determined by stimulating and expelling the stored ionizing radiation from sunlight in the crystal lattice structure during sediment transport, deposition and burial. The resulting released radiation is called luminescence (Preusser *et al.,* 2006; Srivastava *et al.*, 2008; Rhodes, 2015)

3.0 GEOLOGICAL CONTROLS ON RUPTURE GEOMETRIES

3.1 Introduction

Surface ruptures from the 2016 earthquake in the study area are contained within a number of rock types and produced slip on faults that were previously mapped as inactive or not mapped at all (Rattenbury *et al.*, 2006; Barrell and Townsend, 2012; Fig. 3.1). In the literature there is an established link between the geological fabric in bedrock and fault orientation (Anderson, 1951; Donath, 1961; Peacock and Sanderson, 1992; Scholz, 2002). Bedrock anisotropy such as layering or bedding, which produce contrasts in mechanical strength, may in part control the geometry and propagation of fault ruptures. For example, figures 3.1 and 3.2 show a clear connection between the orientations and locations of formation contacts in the Cenozoic cover sequence and faulting. This chapter of the thesis will examine the relationship between surface ruptures and bedrock fabric (bedding and pre-existing faults) and attempt to answer the following questions:

- How do Cenozoic and Mesozoic bedding and pre-existing faults influence the geometry of the 2016 surface ruptures?
- What does the relationship between fault orientation and geology indicate about the origin of the surface ruptures?
- Does the interplay between geology, topography, and surface ruptures indicate whether the 2016 event is a typical rupture pattern for the SLF?

3.2 Previous Work and Study Area Stratigraphy

3.2.1. Previous Work

There have been many detailed geological surveys throughout North Canterbury, starting with the work of Buchanan (1868). In the 20th century geological studies in North Canterbury included Speight (1918), Fyfe (1936), Wilson (1963), Gregg, (1964) and Mason (1949) around the Waipara, Culverden and Waikari Basins. There were limited structural studies south of the Hope Fault until Powers' (1962) examination of terraces in the Hurunui River Valley. However, in the last 30 years, there have been numerous theses on active deformation in the wider North Canterbury region including research by Cowan (1989) and McMorran (1991) on the Hope Fault,, as well as the active faults in the northwest corner of the Culverden Basin (Mould, 1992; Noble, 2011) and examination of Cenozoic deformation in the Waipara and

Lowry Peaks area (Litchfield, 1995; Nicol, 1991). Despite a concerted research programme on North Canterbury active deformation over the last 30 years, no thesis studies have included The Humps or Leader faults and no research has been conducted on the structures in the study area.

Despite the lack of detailed structural studies, field mapping (and geological map preparation) near the study area was undertaken by Fyffe (1936, unpublished maps), Warren, 1995; Parnassus geological map), and Begg (2002, geology of the Waipara region). Warren describes the area around Woodchester as "a shallow syncline/ fault angle depression that is truncated to the north by the basement-bounding NE striking Woodchester Fault which juxtaposes Torlesse Supergroup basement and Greta (siltstone) Formation". Rattenbury *et al.,* (2006) include Woodchester in the 1:25,000 scale Kaikōura geological map from the QMAP series. Only four bedding measurements were presented immediately outside the study area in the Kaikōura geological map, with these data sourced from Fyffe (1936), Warren (1995), and Begg (2002). The geological map presented in this Chapter has used the Kaikōura geological map for reference, but has modified the locations of the lithological boundaries and added structural data wherever outcrop exposure permitted. In all cases descriptions of these map units in this thesis follow the nomenclature of (Browne and Field, 1985).

Outcrop data at Woodchester Station study area is limited, and confined to a few road cuttings, a man-made quarry, streams, and along the Leader River. Stratigraphic contacts and structural data were recorded at these outcrops, and inferred beneath Quaternary terrace surfaces common in the study area.

3.2.2 Basement Rocks and Faults

The basement rocks in the study area form part of the Mesozoic Torlesse Supergroup (Ktp, Fig. 3.1 and Rattenbury *et al.,* 2006), a suit of interbedded quartzo-feldspathic sandstones and mudstones that dominate the eastern South Island and grade westwards into schist (Browne and Field, 1985; Rattenbury *et al.*, 2006).

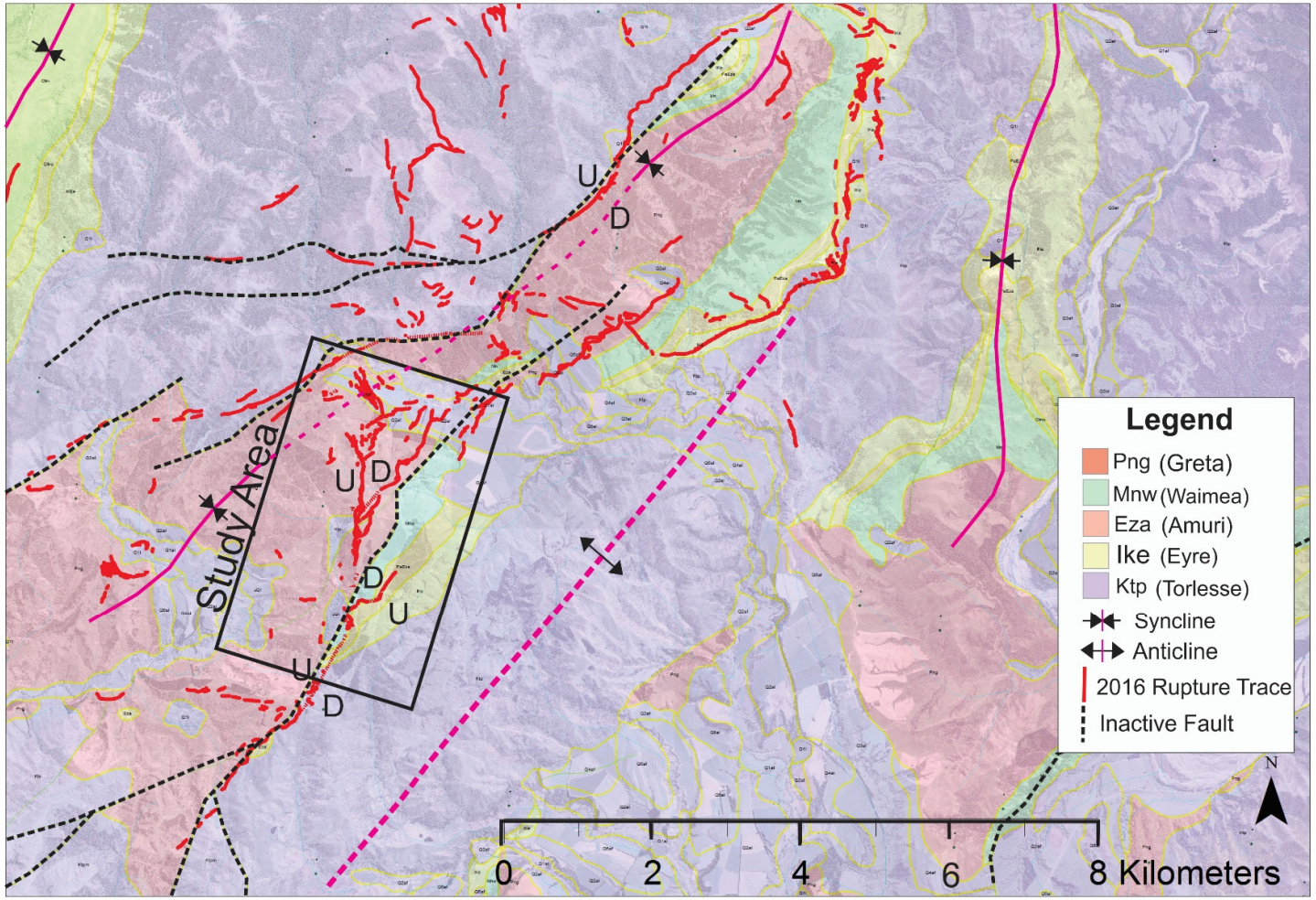

Figure 3.1: Original geological contacts after Rattenbury *et al.* (2006) showing the study area (black line rectangle) with added 2016 rupture traces from Nicol *et al.,* (2018), this study, and unpublished data. U and D indicate upthrow/downthrow fault direction on faults.

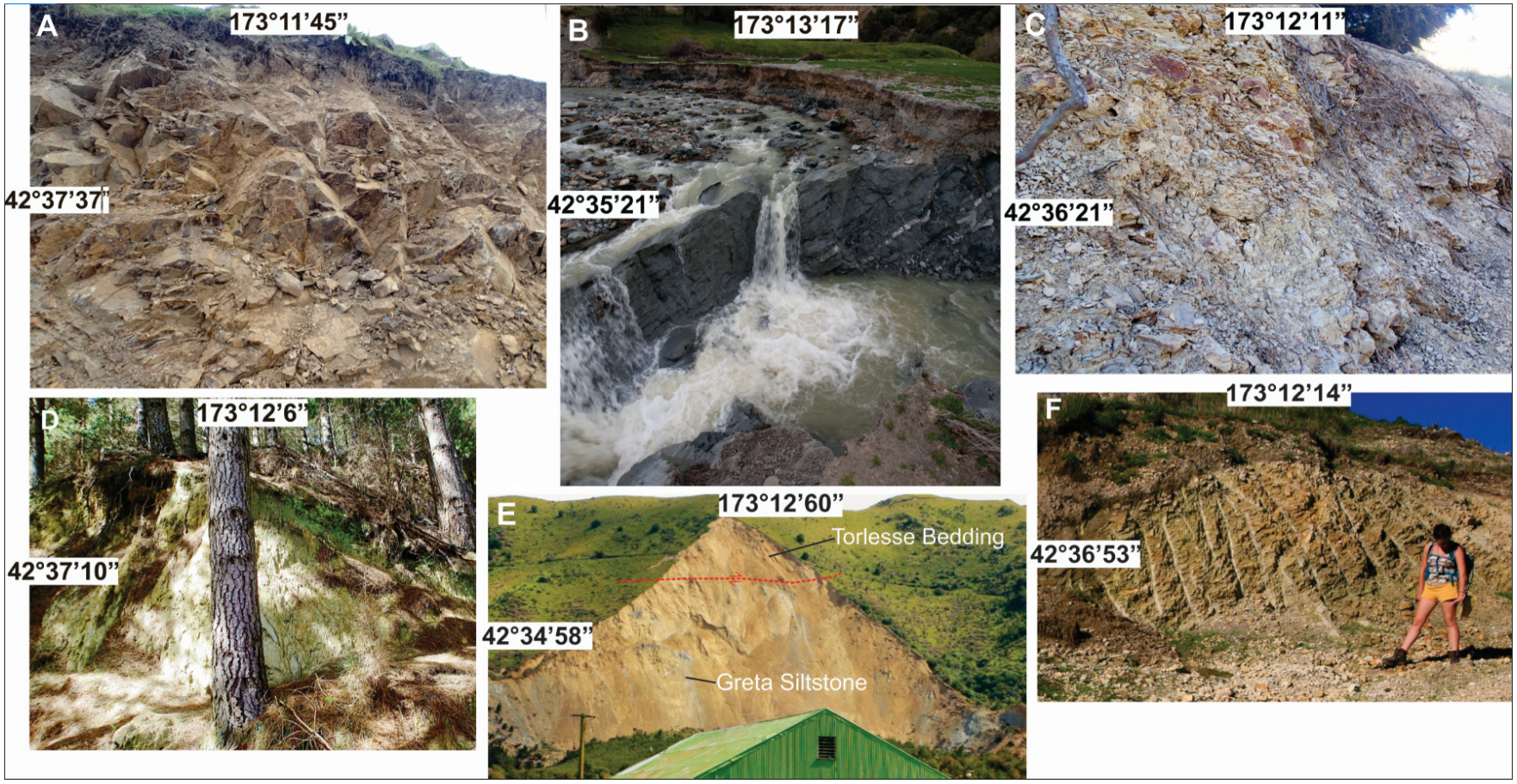

Figure 3.2: Field photographs with latitudes and longitudes of rock outcrops in the study area. A: Highly fractured Torlesse outcrop along road cuttings, B: Massive Greta expsoures in the Leader River, C: Jointed and bedded jarositic Loburn mudstone, D: Small exposure of Waimea Formation north east of location 3; Figure 3.3, E: The Leader Landslide which highlights Torlesse bedding atop blue-grey Greta outcrops separated by a segment of the HF; the main strand of The Humps Fault separates the two rock types, and F: Amuri Limestone exposed at quarry.

The Torlesse Supergroup (hereafter referred to as "Torlesse" or "Torlesse basement") is heavily fractured, and complexly deformed by faults and folds. Outcrops of Torlesse in the study area are mostly limited to road cuttings (Fig 3.2A), where bedding is rarely traceable more than 2-3 m. The dips along the road cutting range from ~30-75°, with values of 40-50° locally most common. The Torlesse is in fault contact with Neogene Greta Siltstone Formation in two key areas (Fig 3.2E, Fig 3.4, location 1). At the southern part of the field area (i.e., immediately south east of location 1, Fig 3.3) the Torlesse lies beneath and is being overthrust by the Greta Formation. However, the Torlesse/Greta Formation contact is best exposed in the scarp of the Leader Landslide, where Torlesse rests on Greta Formation along the rupture the of the HF (Fig 3.2E).

Throughout Woodchester Station and North Canterbury, the Torlesse occurs topographically higher than all other geological units (except for Quaternary deposits), and is well preserved along topographic ridges. This topographic relationship occurs because Torlesse is exposed at anticline hinges which typically form the highest parts of the landscape.

3.2.3 Cover Sequence Rocks and Faults

The Late Cretaceous-Early Pleistocene cover sequence includes the Eyre Group (Ike), the Amuri Limestone (Eza), the Motunau Group (Mn), and the Greta Siltstone Formation (Png), and is likely no more than a kilometre in thickness in the study area.

The Eyre Group in North Canterbury unconformably overlies the Torlesse basement, and is Late Cretaceous- Early Eocene in age. It has been interpreted as a transgressive shelf unit (Browne and Field, 1985), and consists of at least 17 individual sandstones and mudstones ranging in age from Piripauan to Whaingaroan. In the Parnassus area (see appendix A), sandy rocks fine upwards into 240 m and consist of jarositic, grey siltstone to very fine-grained sandstone (Rattenbury *et al.*, 2006). At Woodchester Station, the Eyre group outcrops (up to 8 m in height) were limited to two localities (one exposed in a stream bed, and a second exposed along the Leader River; marked where there is structural data), that were adjacent to Torlesse. These outcrops were characterized by glauconitic sandy siltstone and jarositic sandy mudstone, and are likely members of the Loburn or Ashley Mudstones. However, for the purposes of this thesis, they are simply referred to as the Eyre Group. In the northern section of the field area where an outcrop is exposed along the Leader River, there is a fault that runs along the contact of the Eyre Group and the Greta Siltstone Formation, and is

inferred to be approximately bedding parallel; the specifics of this fault will be addressed in 3.3.1. The other exposure occurs south of The Wall locality, where the contact between Torlesse and Eyre Group is exposed in a stream. In map view, the Eyre group is a maximum of 175 m wide.

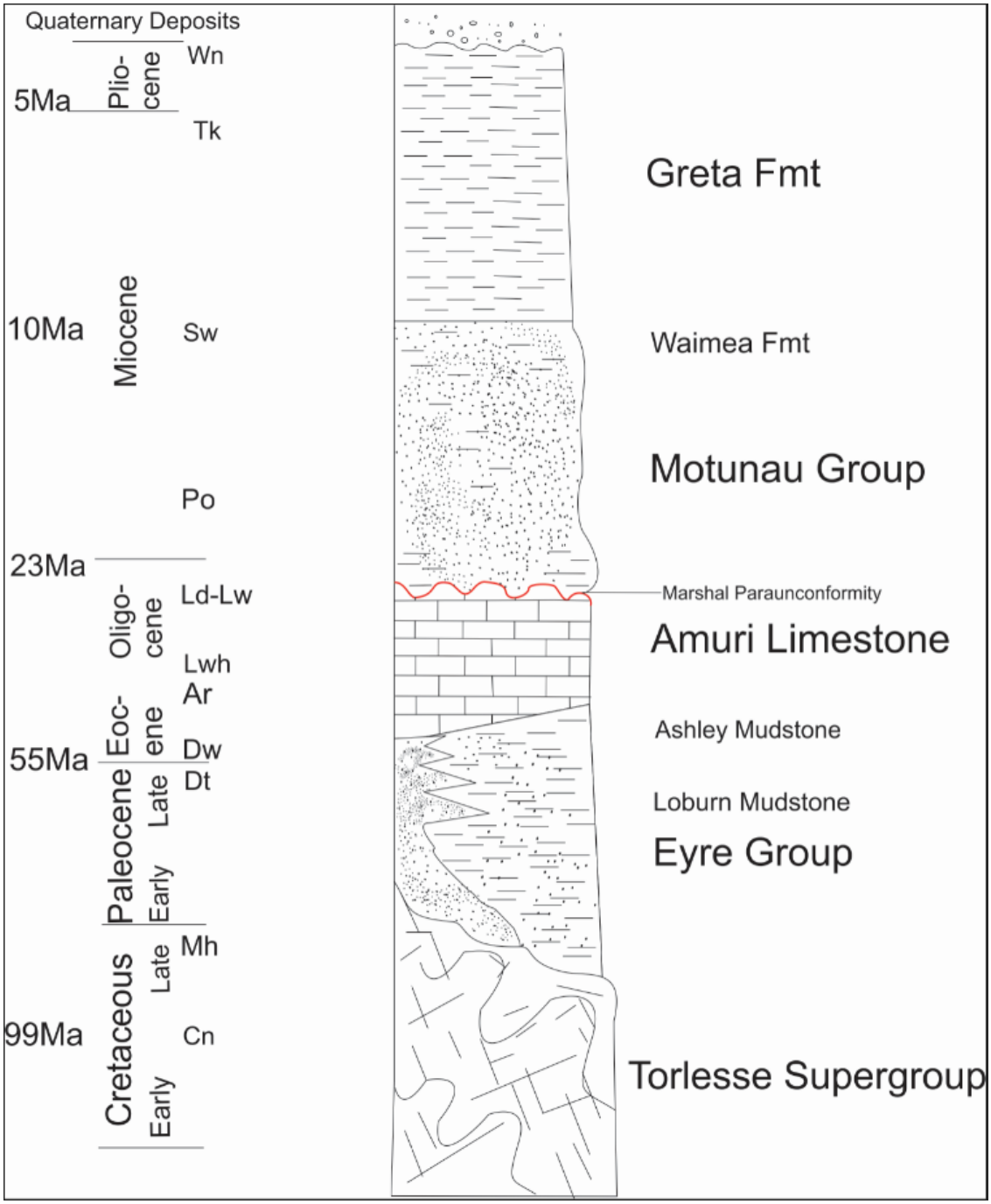

Figure 3.3 Generalized stratigraphic column of units found in Woodchester. Stratigraphic column is not to scale and does not indicate thickness. Ages and names follow conventions from Browne and Field (1985).

The Amuri Limestone rests on Eyre Group and is an argillaceous limestone that is white to light cream in colour, well indurated and fractured. It is Oligocene in age, and composed mainly of cocoliths and foraminifera with extensive bioturbation. Inland exposures of this unit in North Canterbury are all of Whaingaroan age (Browne and Field, 1985), and rest conformably on Eyre Group. There is some debate over the specific environment of deposition, but in North Canterbury the Amuri Limestone is likely an offshore pelagic limestone formed in soft bottom conditions (Finlay, 1946).

The thickness of the Amuri Limestone is highly variable over short distances, likely due to erosion associated with syn-depositional channelization, post-depositional uplift and/or Late Cenozoic faulting. At Woodchester Station, the Amuri Limestone is well exposed at a quarry (Fig 3.2, location F), where The Wall s are approximately ~15 m high, and in the banks of the Leader River which are ~10 m high. The Amuri Limestone does not exceed 100 m width in map view. At the quarry location the top of the Amuri Limestone is defined by a fault which ruptured in 2016 and, again, is oriented sub-parallel to bedding (section 3.2.1 will describe this fault in more detail).

The Motunau Group rests on Amuri Limestone and was first described by Browne and Field (1985). The Marshal Paraunconformity forms the contact between the top of the Amuri and the base of the Motunau Group. The Motunau Group includes nine formations that encompass a diverse range of sediments in North Canterbury of late-Eocene to mid-Miocene age of largely shallow marine sedimentation. At Woodchester, it is represented primarily by the Waimea Formation, and consists of blue grey, moderately indurated calcareous, poorly bedded, massive, very fine to fine sandy siltstone that sit disconformably on the Amuri Limestone. The best exposures also occur in the quarry, where a fault defines the Amuri Limestone and the Waimea Formation contact, however it is also exposed along the Leader River. Its maximum thickness in a single outcrop is ~20 m, but can locally exceed 300 m of thickness immediately south of Parnassus (see appendices A for a map of surrounding townships). In map view, it has a maximum width of ~285m in the study area.

Finally, the mid-Miocene to early-Pleistocene Greta Siltstone Formation (also referred to in this thesis as “Greta Siltstone” or “Greta Formation”) dominates the bedrock of Woodchester, and has many exposures along road-cuttings, riverbeds, and landslide headwall scarps. It is dominated by blue-grey massive fine-grained, moderately to well bedded siltstones likely

deposited in quiet continental shelf or slope environments, and is estimated to be up to 800 m thick near Waiau (Browne and Field, 1985). In map view, Greta Siltstone can be as wide as 6 km across strike in the Woodchester Station region (Fig. 3.1). It lies conformably atop the Waimea Formation, and in places, rests on Torlesse Supergroup across an angular unconformity.

3.2.3 Folding of Cenozoic Strata

The Cenozoic sequence in North Canterbury is deformed by a series of NE trending, gently plunging (<25°), steeply inclined (axial planes >60°) and gentle-open (interlimb angles ~160-80°) folds (Nicol, 1991; Nicol *et al.,* 1994). The study area is located on the limb between a syncline to the west and an anticline to the east, with bedding most often dipping at 20-50° west (Fig. 3.1). These folds trend ~40° with plunges NE and SW at shallow angles (<20°). The syncline was first described by Warren (1995), while the anticline approximately 2 km west of the study area has been inferred for this study based on outcrop patterns, topography and bedding orientation measurements from previous work (Fyffe, 1936; Warren, 1995; Begg, 2002). The kinematic significance of this anticline is further explored in Chapter 4.

3.3 Surface Rupture Geometry

The southern ruptures of the Kaikōura earthquake are among the most intricate and complex recorded for a historical earthquake (Litchfield *et al.,* 2018). The SLF seems to be no exception at a local scale, as the ruptures across the study area are variable with respect to their geometries, continuities, and displacements. The 2016 surface ruptures in the study area form short (<3km) and discontinuous traces with variable fault strikes and dips that accommodate sinistral reverse, reverse dextral, normal sinistral, and sinistral normal displacements. Although the SLF has been broadly characterized as an oblique left-lateral fault upthrown to the west with an N-NW strike (Nicol *et al.,* 2018), this classification fails to convey the complexity of the individual fault traces. In this chapter, three groups of faulting have been identified based on their geometries and kinematics, with each fault category being indicative of the underlying geology. These fault groups include:

1. NE-SW striking (210-245°) and moderately dipping (25-40°) oblique thrusts with approximately bedding-parallel orientations (referred to as bedding-parallel faults),
2. N-S (350-360°) striking, steeply dipping (70-85°) faults with sinistral normal displacements, and
3. ENE-WSW (250-260°) striking, moderately dipping (50-68°) faults that are interpreted to be part of the HF.

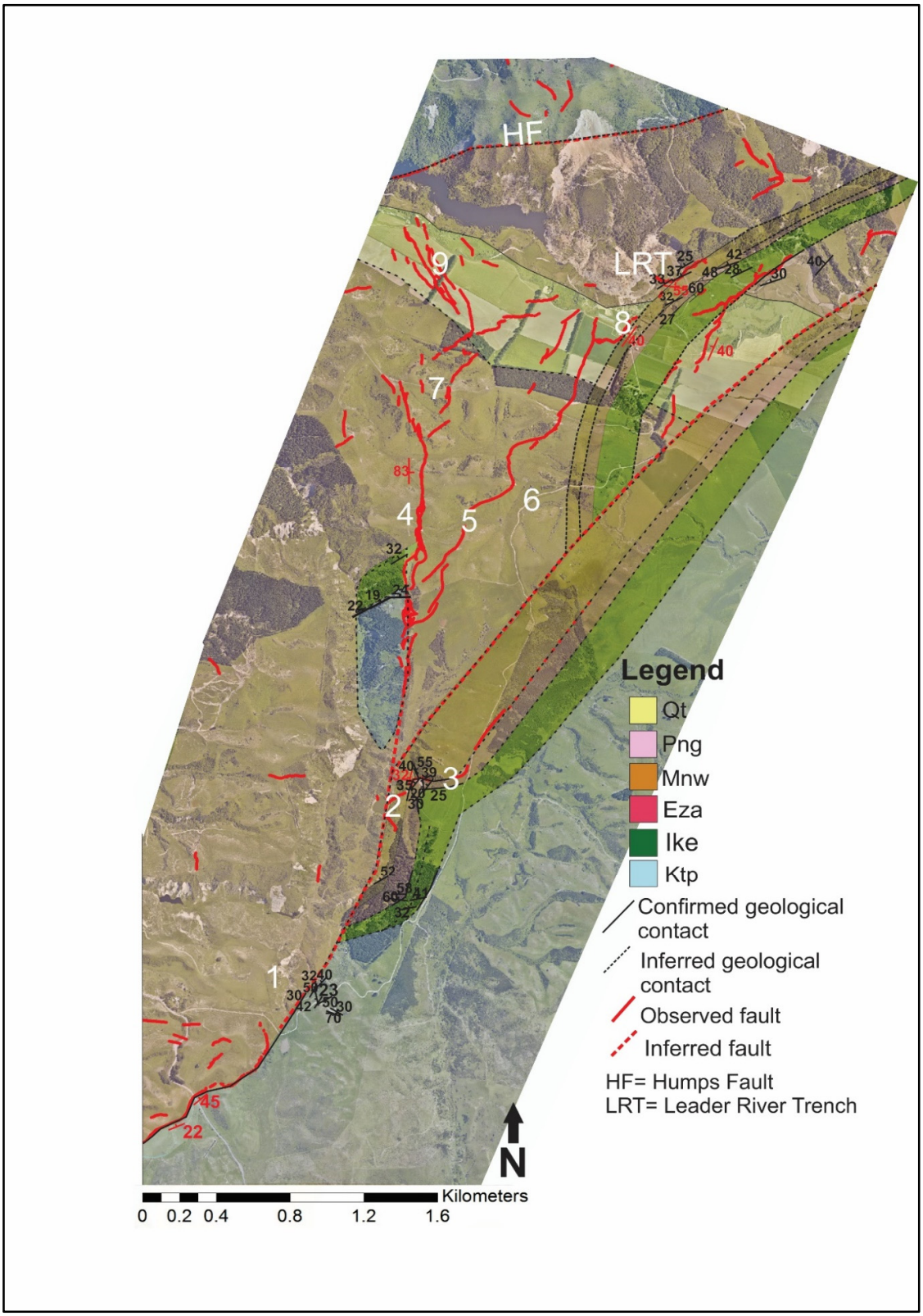

Figure 3.4: Fault trace map atop geological units in the study area. White umbers correspond to photos shown in Figure 3.5. The Waiau Wall runs from 4-7; HF= Humps Fault LRT= Leader River Trench.

3.2.1 Bedding-Parallel Ruptures

Bedding-parallel fault traces are irregular, short, and discontinuous, with steps of up to 2 km between well-established traces. In general, the bedding-parallel fault traces in the study area are upthrown and dip to the west, with the exception of the fault atop of the Amuri Limestone at the quarry (upthrown to the east; locations 2 and 3; Fig 3.4 & 3.5). Bedding-parallel faults upthrown to the west are interpreted to be tectonic, while the fault upthrown to the east (Fig 2.4 depicts a transect showing the east up orientation) is inferred to have a strong gravitation overprint which is discussed in Chapter 4. The rationale for characterizing slope movement vs. tectonic fault activity is addressed in Chapter 2.

Bedding-parallel faults are observed or inferred at four locations along the SLF with each site described separately below:

- The Leader Road fault (Fig. 3.4, immediately SW of location 1): Here the ruptured fault forms the contract between the Greta Siltstone and Torlesse basement. Based on the v-pattern across the valley and the apparent dip of the rupture trace as it climbs the southern side of the valley the fault strikes ~068° and dips at 45° NW. This fault orientation is approximately parallel to the 034/42°W orientation of Torlesse bedding 800 m NW, and is interpreted to have utilised the Torlesse-Greta Siltstone unconformity surface.
- The Quarry fault (Fig. 3.4 location 4): The fault forms the contact between Amuri Limestone and Waimea Formation. At this location, the fault forms a surface rupture that can be mapped for 510 m which ruptures across existing topography and forms the contact between the Amuri Limestone and Waimea Formation. The fault forms a v pattern across a small valley and has a calculated fault strike of ~200° and dip of ~33°W (using the three point problem; see Chapter 2). Strike and dip of Amuri Limestone bedding immediately beneath the fault is ~240/28° and sub-parallel to the estimated fault orientation. The fault appears to have formed along the boundary between highly indurated Amuri Limestone and lower strength (than Amuri) Waimea Formation. The fault dips towards a deeply incised valley 400m west of the quarry and immediately after the earthquake was marked by large fissures up to 0.3 m width and 1 m depth (see Chapter 4 for further discussion). This fault trace is lost as it propagates to the NW.
- The Shearer's Quarters and Leader River Pumphouse faults: The Shearer's Quarters fault (Fig 4.3; location 8) is inferred bedding parallel, and has a strike of 225°/40°W.

At this location the Waimea Formation dips from, 48-55° W and strikes from 240-255°. Four hundred and thirty m to the west of this location is referred to as the Pumphouse fault (named so because the fault destroyed a pumphouse during the 2016 event). It is also inferred bedding sub-parallel between the Eyre Group and Greta Siltstone, and is oriented at 210/40°W. Both the Eyre Group and Greta Siltstone are oriented approximately 250/30°W/NW. Roll-over structures are characteristic of both these faults, and immediately after the earthquake, they were visible as large 0.5-1 m thrusts on the high terrace surface and river bed with right-trending stepovers.

3.2.2. Steeply dipping SLF faults

The steeply dipping faults that formed The Waiau Wall are the single most identifiable and continuous structure in the study area (Fig 3.2, location 4-7). The Waiau Wall was a single, continuous trace of approximately 500 m length before it was bull-dozed. The Wall traces can be seen clearly on aerial photography, Google Earth, LiDAR, and in the field for 2.3 km before they reach the intersection zone with the HF to the north or disappear in steep valleys to the south. This fault surface is oriented N-S with a strike of 354° and a maximum dip of 85° to the east. On the scale of meters to 10's of meters, the fault is segmented and contains thrust and strike-slip dominated fault strands. Within step-over zones right-stepping reidel shears are often observed. The Wall scarp records the highest vertical displacement in the study area (and along the entire length of the Leader Fault, Nicol *et al.,* 2018), and is classified as a normal fault with a sinistral component. This will be further discussed in Chapter 4. East of The Wall , a toe thrust was identified which broke the surface as a series of rolls, and is traceable in map-view as a discontinuous curved feature, sometimes forming two or three individual fault strands. The toe thrust curves and bends through topography, which indicates a low dip (e.g., <40°;Fig 3.4 and 3.5; location 6; Fig 3.6).

The Wall structure is completely contained within the Greta Siltstone, and appears to cut across Cenozoic bedding at a high angle. As The Wall fault extends to the north it changes in strike to NNW and bifurcates into several short (<1 km) strands on the Quaternary terraces of the Leader River. These strands are accompanied by tensions crack and roll-over features with up to 60% shortening (Fig 3.3 and 3.4; locations 7 and 8).

3.2.3 The Humps Fault (HF)

The SLF intersects with the HF in the northernmost extent of this study. Here, The HF strikes from 255-280°, dips from 45-68°, and runs parallel to slope contours around the Leader Landslide. In the intersection zone of the SLF and the HF, fault traces are irregular and discontinuous with dextral-reverse and oblique normal displacements. Strands of the HF are largely contained within Greta Siltstone, but at the trench locality intersect a bedding-parallel fault which defines the Greta Siltstone and Waimea Formation contact. This fault is located immediately SE of the toe of the Leader landslide, ~300 m NE of location 8 on figure 3.4, and contains a natural trench (known as the LRT on Fig 3.4) that was logged and interpreted in Chapter 5 of this thesis. The kinematics of the displacements along this section are discussed in Chapter 4.

The Leader River Trench fault forms part of the HF (Fig 3.4, called LRT). This area is characterized by highly segmented, discontinuous fractures that are part of the damage zone between the SLF and HF with varying slip senses, though the trench fault is classified as dextral-reverse, strikes at ~285° and varies in dip from 55-68°. As Chapter 5 will explore in further detail, the fault initially is contained within the Greta Siltstone where it is assumed bedding sub-parallel; the Greta Siltstone here varies in strike at this location from 237-245°, and dips from 37-45°. However, the fault swings ~45-50° and dips ~45° between the contact of the Greta/Waimea Formation where it is assumed bedding parallel. Figure 3.5 location 9 depicts a highly fragmented trace at the intersection of the HF and SLF, where many discontinuous fractures exhibit both reverse and antithetic structures.

The main fault strand of the HF in this study area crosses the headwall scarp of the Leader Landslide where Torlesse has been thrust over Greta Siltstone (Fig 3.2E). Gray (2017) mapped and characterized the Leader Landslide and found fault gouge, separating Torlesse and Greta Siltstone which was oriented at 250/39°N. This fault plane orientation is broadly consistent with the orientation of Greta Siltstone in the Leader River bed (Fig 3.7) and suggest that fault movement and development has locally utilized the fabric of the Greta Siltstone Formation.

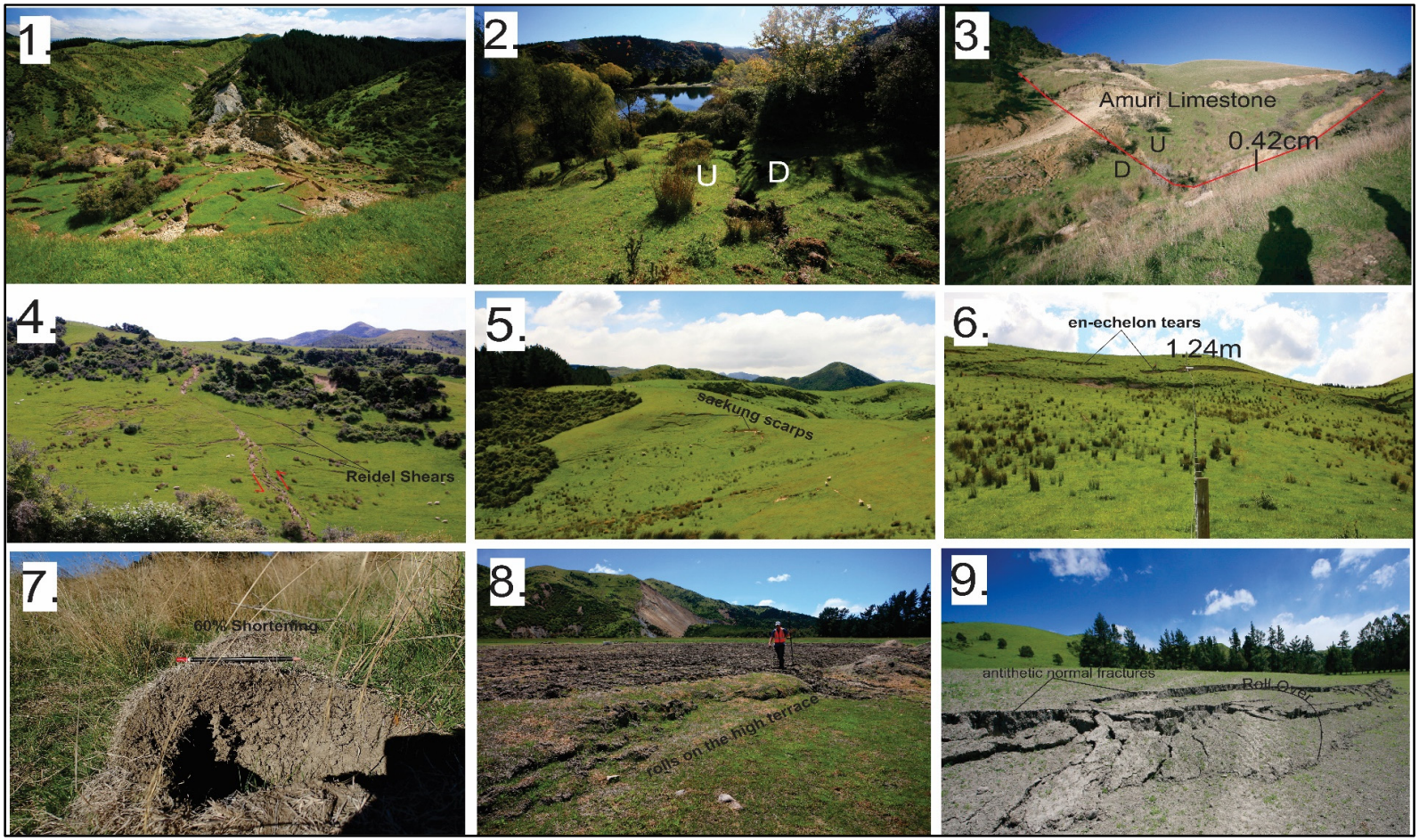

Figure 3.5: Fault and landslide deformation styles along the SLF. 1.) Landsliding and sacking features atop an inferred fault at location 1. Greta siltstone is exposed amidst landsliding. 2.) View looking SE as the Quarry fault cuts up- a hill at location 2. 3.) Quarry fault straddling the boundary between the Amuri Limestone quarry and Waimea Formation, with a scarp height of 0.42 cm at location 3. 4.) Annotated Reidel shears along The Wallat location 4. 5.) Sackuung features atop ridges at location 5. 6.) Bedding parallel fault traces within en echelon tears and sinistral offset of 1.24 m at location 6. 7.) Roll-over relay ramp between fault segments at location 7. 8.) Thrust fault on the high terrace at location 8 expressed as rolls, and 9.) Thrust rupture with antithetic normal faults on the high terrace at location 9, where the Humps Fault Zone begins to intersect. Photographs 1-6, 8 and 9 by Kate Pedley and photograph 7 taken by the author.

Fig 3.6: Surface geometry of the toe-thrust of The Waiau Wall. Photo by Dr. Kate Pedeley.

3.4 Relationship between Surface Ruptures and Geology

3.4.1 Bedding-Parallel Faults

Geological map and cross sections have been used to illustrate the three-dimensional geometry of bedding-parallel faults (see Chapter 2 for description of cross section construction).

The Eyre Group, Amuri Limestone, and Waimea Formation in the study area form the eastern limb of a syncline with average bed dips of ~35° west and maximum values of ~45°. Several of the faults in the cover sequence strike and dip parallel to bedding to form thrusts with varying degrees of strike-slip motion (Chapter 4 will further examine their slip senses and kinematics). Bedding-parallel faults are shown in two cross sections (Figs 3.7 and 3.8), which are presented at true scale (i.e. with no vertical exaggeration). The data and assumptions underpinning the cross sections are provided below.

In Figure 3.7, the fault dips for the two westernmost faults are about 40°W, however the easternmost fault that straddles the contact between the Greta Siltstone and the Waimea Formation is inferred from stratigraphy. The bedding-parallel faults that ruptured all

produced slip along formation boundaries and in all cases the bedding-parallel faults do not appear to locally cut across stratigraphy (as suggested by the outcrop patterns).

The interpreted cross sections shown in Figure 3.7 contain a number of assumptions;

1. The inferred fault between the Waimea Formation and Greta Siltstone to the east in Figure 3.7 also dips at ~40° is parallel to bedding. This inference is supported locally by the outcrop pattern which is consistent with the fault not cutting across stratigraphy,
2. Faults in the subsurface, also occupy the formation boundaries and are parallel to bedding (as they appear from outcrop observations; Figs 3.7 and 3.8),
3. The bedding dips used to create the cross-section in figure 3.7 were adjusted to account for the obliquity between bedding strike and the trend of the section line (on average 45° in Fig. 3.7). For construction of the section, average bed dips of 32°, 40° and 34° were used for the Greta Siltstone, Waimea Formation and Amuri Limestone, respectively. These dips produced apparent dips in the plane of the section of ~24°, ~31° and ~26°,
4. The bedding dips used to create the cross-section in figure 3.8 trends at a high angle to the strike of bedding (~60°) and apparent dips are approximately equal to true dips. The bed dips used to construct Figure 3.8 are: Torlesse and Loburn Mudstone contact west of the steep fault ~26°, Greta Siltstone, Waimea Formation and Amuri Limestone east of the fault ~34-45° dip.

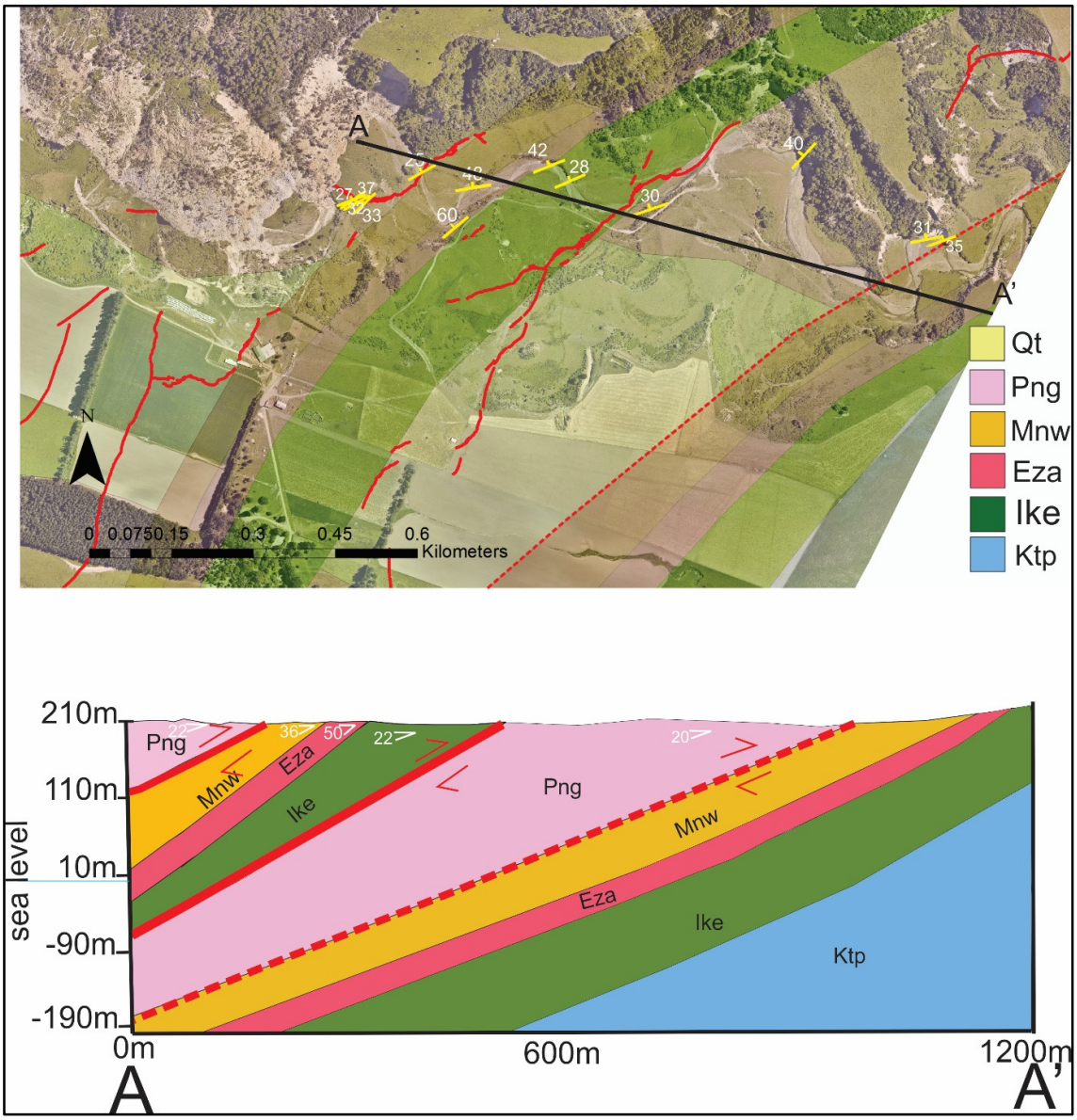

Fig 3.7: Interpreted cross-section along the Leader River bed. See Fig. 3.1 for legend and text for descriptions of units Ktp, Ike, Eza, Mnw, Png and Qt.

In the northern section A-A' the inferred bedding parallel faults occupy the base of the Greta Siltstone and the base of the Eyre Group, while in the southern section the 2016 ruptures are primarily along bedding within the Greta Siltstone and along the top of the Amuri Limestone. From the available data it appears that not all bedding planes accommodated slip during the 2016 earthquake and that bedding-plane slip was discontinuous (i.e. the same formation contact did not rupture everywhere). The observations made in the field and from cross sections seem to support the hypothesis that bedding-plane faulting reflects flexural slip (Fig 3.10). In a model of flexural-slip faulting, slip occurs along layer interfaces during tightening

of folds (Fossen, 2016). This mechanism is discussed further in Chapter 4 on fault kinematics.

3.4.2 Steeply Dipping Faults (The Waiau Wall)

As Chapter 4 will explore in greater detail, The Waiau Wall is a very complicated structure. While it had the highest amount of slip along the SLF, it was entirely unknown prior to 2016, and seemingly ruptured across Cenozoic bedding. Unlike most of the other faults that ruptured in 2016 across the field area, The Wall fault is contained within the Greta Siltstone (at the ground surface), and dips steeply (~85°) to the east. The underlying reason(s) for the northerly strike and steep dip of the fault at The Wall are not entirely clear, however, it remains possible that The Wall fault utilizing pre-existing fabric in the Torlesse below the Cenozoic cover sequence. While the dip of The Wall fault at depth remains speculative, the cross section in Figure 3.8 provides clues to its geological history.

As interpreted in Figure 3.8 the steeply dipping fault vertically displaces Eyre group by ~800 m and the basal Greta Siltstone by ~650 m. Given the uncertainties associated with cross section construction, which could produce uncertainties on vertical displacements of ±200 m the values of displacement on the two horizons could be the same or similar. Therefore, the available outcrop data suggests that The Wall fault has likely accommodated 100's of meters of displacement since deposition of the Greta Siltstone in the mid-Miocene to Early Pleistocene. The precise period over which this displacement accrued remains uncertain, however, given that the fault ruptured in 2016 it seems likely that some of the displacement recorded in cross section B-B' accumulated during the last 1-2 Myr when accelerated faulting and folding is estimated to have commenced throughout North Canterbury (Barnes, 1996; Nicol *et al.,* 1994). If this is the case then it is probable that the fault responsible for the generation of The Wall ruptured repeatedly during the Pleistocene. If, for example, the total vertical displacement on the fault is 600 m and this displacement accumulated in earthquakes with 3 m of vertical slip, then about 200 slip events would be required. Interestingly, these slip events have not produced a significant topographic expression at the ground surface.

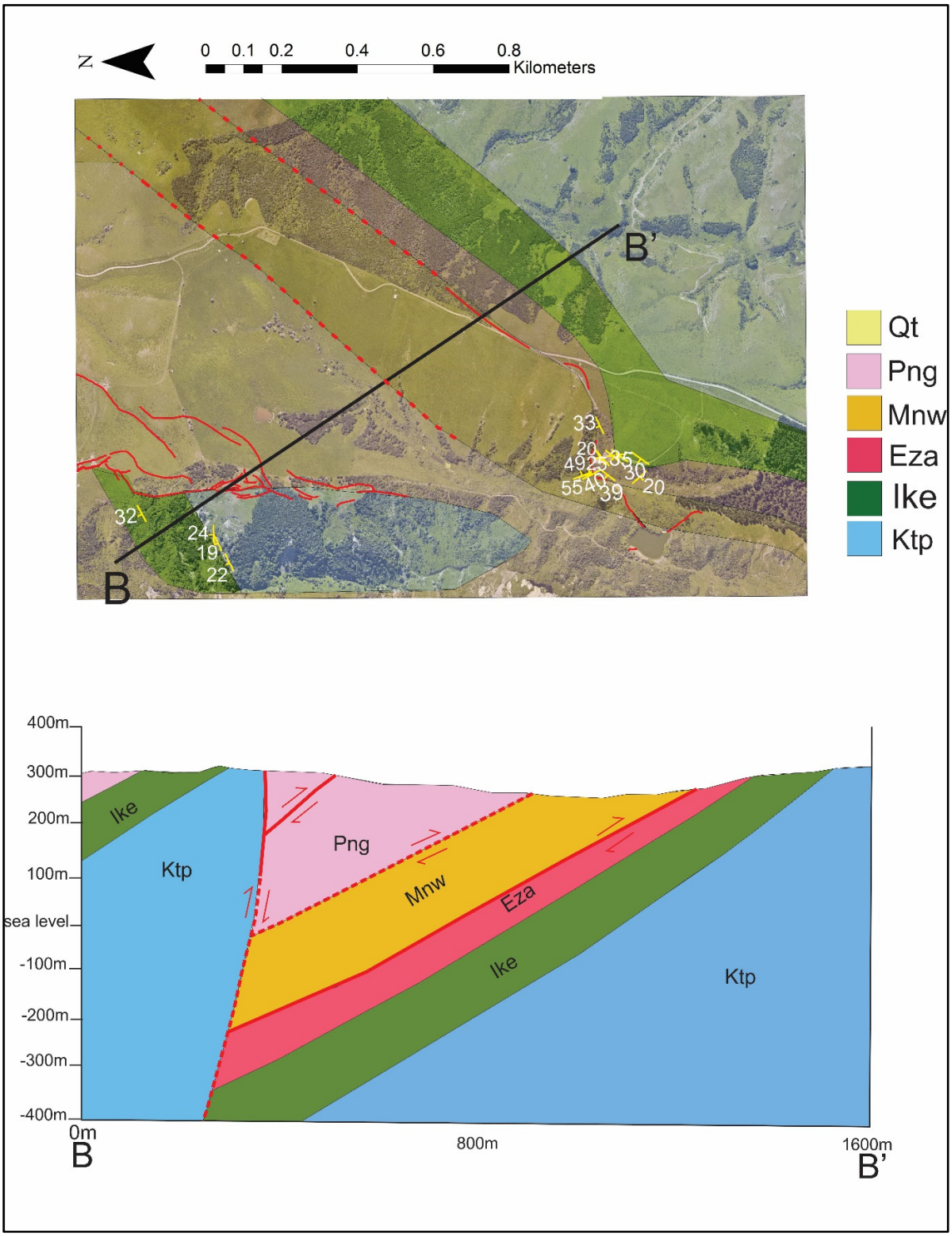

Figure 3.8: Interpreted cross-section across the southernmost extents of The Waiau Wall fault and its intersection with bedding-parallel faults. See Fig. 3.1 legend and text for descriptions of units Ktp, Ike, Eza, Mnw, Png and Qt.

In Figure 3.8 the rise in topography from east to west across the fault is 50 m, with the highest topography occurring towards B' and distal to The Waiau Wall fault that ruptured in

2016. This lack of topography across the fault suggests that the vertical displacement rates are low compared to the rates of erosion (see next section for further discussion).

3.5 Topographical Correlation of Surface Ruptures and Implications for long-term Rupture Pattern

Topography is often interpreted to reflect long-term patterns of fault-related deformation (e.g., Nicol *et al.,* 2018). In such cases comparison of topography with the deformation during earthquakes can provide insights into the long-term repeatability of the earthquake deformation. In this thesis, estimates of uplift during the 2016 earthquake generated from InSAR by Hamling *et al.* (2017) have been compared to long-term topography and fault deformation. The assumption that underpins this analysis is that, if variations in topography are comparable to the changes uplift during the 2016 earthquake, then it can be inferred that the spatial pattern of deformation during the Kaikōura event occurred repeatedly during the Quaternary.

Nicol *et al.,* (2018) used this method to compare long-term deformation with topography, and found that the uplift of the Mt. Stewart Range (which sits immediately to the north of the study area) and that the HF were well correlated with topography. They suggested that the patterns of displacement and uplift associated with the HF during the 2016 earthquake are comparable with topography, and concluded that this fault could have ruptured repeatedly during the Quaternar, and in a similar manner to the 2016 event (i.e., strike slip on the western fault and associated oblique slip in the east with associated uplift of the Mt Stewart range). This accordance of topography and uplift is not observed along the SLF. Figure 3.9 depicts a transect of deformation derived from InSAR (after Hamling *et al.,* 2017) with the topography across a section of The Waiau Wall, where vertical deformation is ~1.7m. Although there is an accordance between the location of The Waiau Wall and a topographic gradient, in general the two curves show significant differences in shape. The disparity of the two curves suggests that either the uplift pattern in 2016 across the SLF was not indicative of the long-term pattern, and/or Kaikōura type events occur infrequently providing topography the opportunity to be reset by erosion of the western side of the fault. In either case, Kaikōura type events on the SLF would be rare.

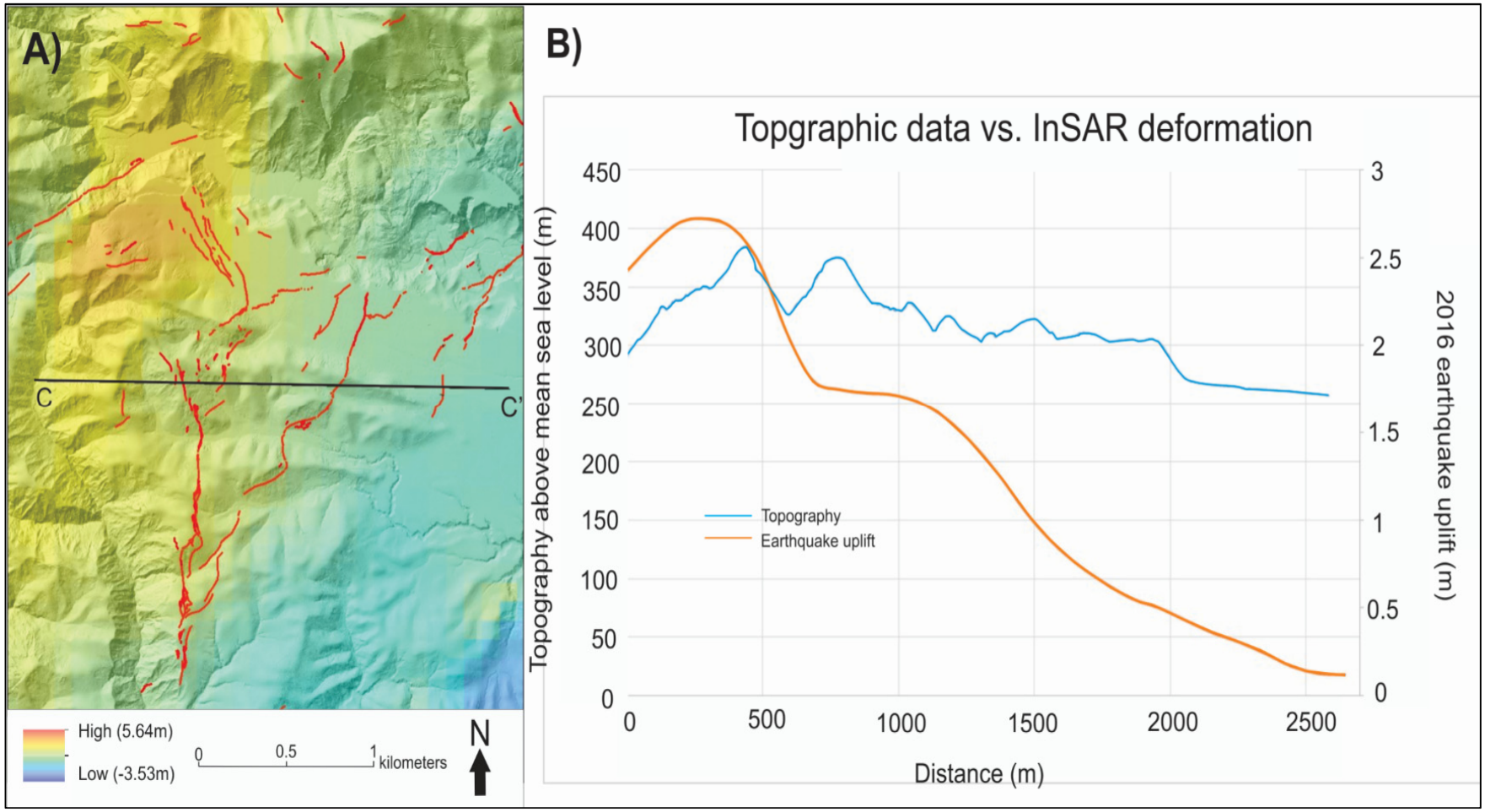

Figure 3.9: W-E transect across fault traces with profiles of topography (blue line) and uplift (orange line) during the 2016 earthquake. A) Map showing colour contours of uplift derived by Hamling *et al.* (2017) from INSAR data, with location of 2016 surface ruptures shown as red lines. B) Topographic (blue line) and 2016 earthquake uplift (red line) data profiles (m).

3.4 Discussion

This chapter presents evidence for faulting accommodated bed flexural-slip folding for bedding-parallel faults. The contractional regime in North Canterbury favours a model where principal shortening (~120°; Nicol *et al.,* 2018*,* ~115°; Sibson *et al.,* 2011; 2012) occurs nearly perpendicularly to the azimuth of the regional anticline and orientation of faults along Cenozoic bedding. North Canterbury stress trends and their comparison with those observed along the SLF will be addressed in Chapter 4 of this thesis.

In the Woodchester area, some of the faulting seems evidenced by folding accommodated by displacement via flexural-slip faults. This was first described in detail by Suggate (1957), wherein low dipping planar or fluvial sequences over lie the steep limb of a fold with an angular unconformity. Flexural-slip occurs when the deforming medium is layered, or has a strong mechanical anisotropy (Fossen, 2016). The anisotropy present along the SLF are weakly consolidated mudstones, sandstones, and siltstones (e.g., Waimea Formation and Greta Siltstone) occur in-between limestones or stronger tensile materials (e.g., Amuri Limestone and Torlesse). These bedding surfaces act like faults, and accommodate slip which allows the folds to tighten in response to shortening. Maximum slip occurs at inflection points and dies out towards hinge, and the sense of slip is opposite on each limb (Fig 3.10; Fossen, 2016). Coincidentally the inflexion line for folding at Woodchester is probably within the study area.

Contractional regimes such as North Canterbury often have many blind thrust faults (Nicol and Nathan, 2001), and in these cases, fold analysis may be the best way to gather seismological insights about fault growth history or earthquake potential (Stein and King, 1984; Stein and Yeats, 1989). Slip on underlying faults, fold geometry and uplift rate of active fault-related folds can be used to infer the slip rate from an assumed kinematic relationships (Johnson, 2018). Factors including rock-strength properties, thickness, stiffness and layering, and fault geometry all contribute to the resulting folding produced by flexural slip. It appears that the geology of the cover sequence controls fault slip and fault geometry in bedding-parallel faults. The reasons for the resulting orientation and geometry along The Waiau Wall are much less clear. It is possible that the steep nature of The Wall is caused by steep fabric in the Torlesse bedding. A possibility could be The Wall ruptured after slip on

the bedding-parallel faults to accommodate more slip, however this is speculative and this idea will be addressed further in Chapter 4.

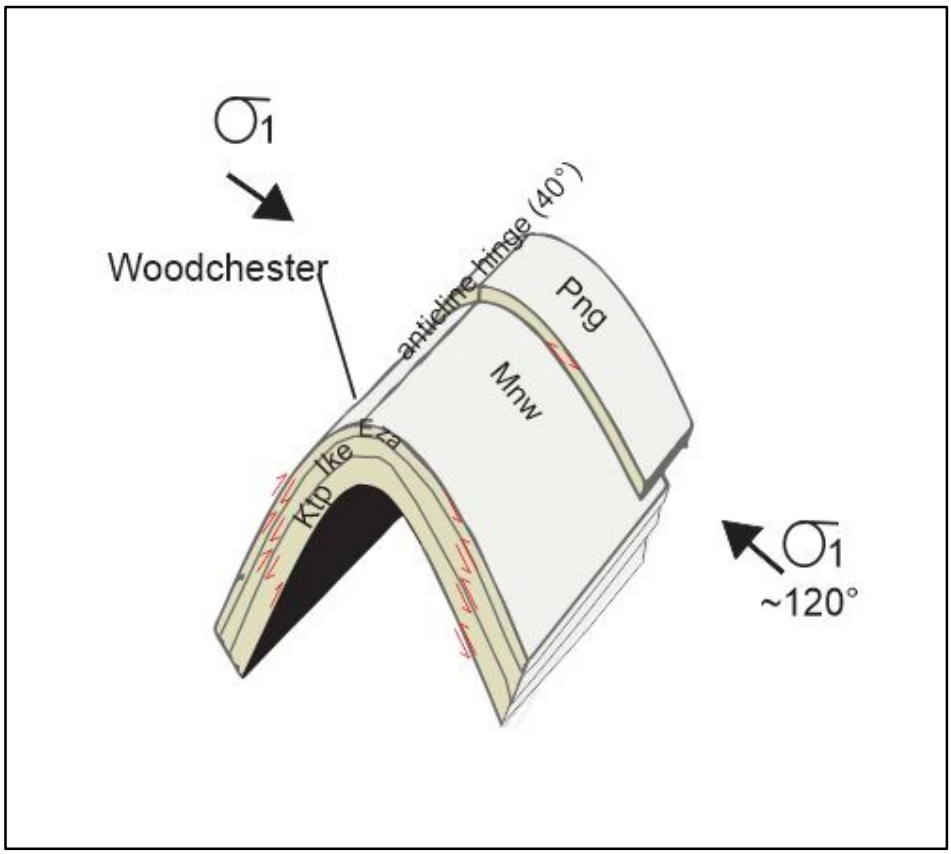

Figure 3.10: A model presenting flexural slip along bedding-parallel fault traces with respect to the regional anticline and regional principal horizontal stress (σ_1) of North Canterbury where units have not been eroded. Modified after Fossen (2016).

3.7 Summary

- There is an established link between geological fabric and fault geometry. This chapter explores the 2016 surface ruptures with respect to the cover sequence they are contained in.
- In general, all rupture traces along the SLF are relatively discontinuous, fragmented, and complicated by the topography. However, this chapter introduces the three schemes of faulting identified at the Woodchester station: Bedding-subparallel faults of the SLF, sub-parallel faults of the HF, and steeply dipping structures contained within the Greta Siltstone.
- Bedding-parallel/ sub-parallel structures trend NE-SW with strikes from 210-250° and dip moderately (25-45°). These faults are generally oblique thrusts that are upthrown to the west and rupture approximately parallel to bedding, and are accommodated by flexural slip folding. They include:

    - the Leader Road fault (68°/45°NW) which ruptured the contact of the Greta Siltstone and Torlesse (~64°/42°W),
    - The Quarry Fault (200-240°/33°W) which ruptured the contact between the Waimea Formation and Amuri Limestone (~240°/28°),
    - The Shearer's Quarter fault (225°/40°W) which ruptured the contact of the Greta Siltstone and Waimea Formation (240-255°/37-45°), and
    - The Pumphouse fault (210°/40°W) which ruptured the contact of the Eyre Group and Greta Siltstone (250°/30WNW).
- The sub-parallel faults of the HF include the Leader River Trench fault, and the Leader Landslide Fault. They strike ENE/WSW (250-260°) and dip moderately (55-68°).
- Fault gouge found in the Leader Landslide was oriented at 250/39°N in-between the Torlesse and Greta Siltstone. The gouge orientation is similar to the structural readings for the Greta Siltstone in the Leader River.
- The Leader River Trench fault is initially contained within the Greta Siltstone oriented at 285/55-60°NW, however it swings 55° and follows the contact of the Waimea Formation.
- The steeply-dipping structures refer to The Waiau Wall. These faults strike N-S (350-360°) and dip steeply (70-85°) faults and accomodate left-lateral normal displacements. They are contained within the Greta Siltstone for unclear reasons.
- The Waiau Wall displayed high amounts of vertical and sinistral displacement, however this is likely not characteristic of previous fault ruptures.
- The correlations between topography and 2016 uplift shows no clear pattern, and there is no topographic indication for The Waiau Wall.

4.0 FAULT KINEMATICS

4.1 Introduction

Fault kinematics include slip magnitude, slip direction, and slip sense, and can be determined from rupture of the ground surface following moderate to large magnitude earthquakes (Kanamori and Anderson, 1975; Stirling *et al.,* 2013; Kearse *et al.,* 2018). These data, combined with estimates of rupture length provide constrains on regional tectonics and seismic hazards (Scholz *et al.*, 1986; Scholz, 2002; Wesnousky, 2008). In low strain regions such as the present study area, measurements and observations of surface ruptures produced by large-magnitude earthquakes are especially important because they are relatively rare. When these ruptures do occur, they typically produce large displacements (e.g., 1-12 m) that dominate the long-term slip budget of faults (Abe, 1981; Scholz *et al.*, 1986; Xu *et al.*, 2002).

As discussed in Chapter 1, the newly discovered Leader Fault was unnamed, and mapped as an inactive bedrock fault before the Kaikōura Earthquake. The fault had no documented earthquake rupture history, and the section of the fault which produced the greatest slip (The Waiau Wall; Fig 3.4, location 4; Fig 4.6 & 4.7A) was entirely unmapped. By contrast, parts of The Humps Fault (HF) had been previously mapped as active to the west of the study area (Barrell and Townsend, 2012). In the northwest corner of the study area, aerial photographs display discrete warps of inferred Last Glacial Maximum (e.g., ~18 ka in age) terrace surfaces along faults that ruptured in 2016. These faults are part of eastern segments of the HF, and will be discussed in Chapter 5. Despite the presence of these rolls no active faults were known to exist in the study area prior to 2016 and no kinematic data were available for any of the faults that ruptured in 2016. The primary purpose of this chapter is to use kinematic data from the Kaikōura Earthquake 2016 surface ruptures to develop a kinematic model for the faults in the study area. A combined dataset including fault displacements and striae measurements from the field, and topographic measurements from InSAR and LiDAR in this have been used to target the following questions:

- Why is the deformation zone associated with the 2016 event so wide (up to 3km)?
- How did the orientation of the fault affect the slip distribution in 2016?
- What do the displacement variations reveal about deformation along the SLF?
- Why are striations so variable along different sections of faults that ruptured?

- How much of the slip along the SLF is tectonic, and how much is gravity driven?
- How do the slip vectors and stress axes compare with regional trends?

All displacement data presented in this chapter were collected in the months following the event, and most (~80%) of these displacements were measured directly from scarps or cultural features that were clearly offset by faulting. The collection, uncertainties, and analyses of data are described in Chapter 2. Analyses of these data complement the results of Chapter 3, where it was proposed that the 2016 event produced slip on bedding-parallel fold-related faults, along sub-parallel structures of the HF, and steep structures of The Waiau Wall. The slip magnitude and vector analyses presented here are the first to help constrain a kinematic model for the SLF.

4.2 Displacement Data and Slip Vector Analyses

The geometries and displacements of fault ruptures are complex. Strike-slip and vertical displacements for the 2016 surface ruptures in the study area are presented in Figure 4.2. For the purpose of this study, west-side up and east-side up vertical displacements are plotted separately, as are dextral and sinistral strike slip. Principal strain axes for fault planes are presented on stereoenets in the form S_1 (shortening) and S_3 (extension; Figs 4.3, 4.4, 4.7 & 4.10), and the azimuth of the regional anticline described in Chapter 3 (~40 °) is plotted alongside bedding-parallel and sub-parallel faults accommodating flexural slip. Slip vectors are present in the form of arrows relative to a fixed hangingwall (Figs 4.3 & 4.11).

Vertical displacement generally increases northwards along the Leader Fault, consistent with an increase in topography towards the inland Kaikōura ranges (Nicol *et al.,* 2018). This regional pattern of vertical displacement is accompanied by short wavelength (<1km) variations of vertical displacement up to 2 m (Nicol *et al.*, 2018). However, these short wavelength variations are not observed along the ~10 km section of the fault, where data are sparse due to the rough topography and limited access (Fig. 4.1). The highest vertical displacements (>1.5 m) are restricted to a 400 m length of the along The Waiau Wall (Fig. 4.2B; Fig 4.6). By contrast, sinistral strike-slip rises northwards to The Wall and then decreases rapidly north of The Wall . Dextral strike-slip is primarily observed in the HF at distances from 5-6 km. In addition to these general trends, the displacement graphs are irregular. This irregularity is also consistent with segmented fault traces mapped in the field

area. For the purposes of this thesis three orientations of faults distinguished which include; 1. bedding-parrallel faults, 2. steep N-S faults of the SLF and 3., steep, sub-parallel ENE faults are part of the HF (see Chapter 3 for further definitions).

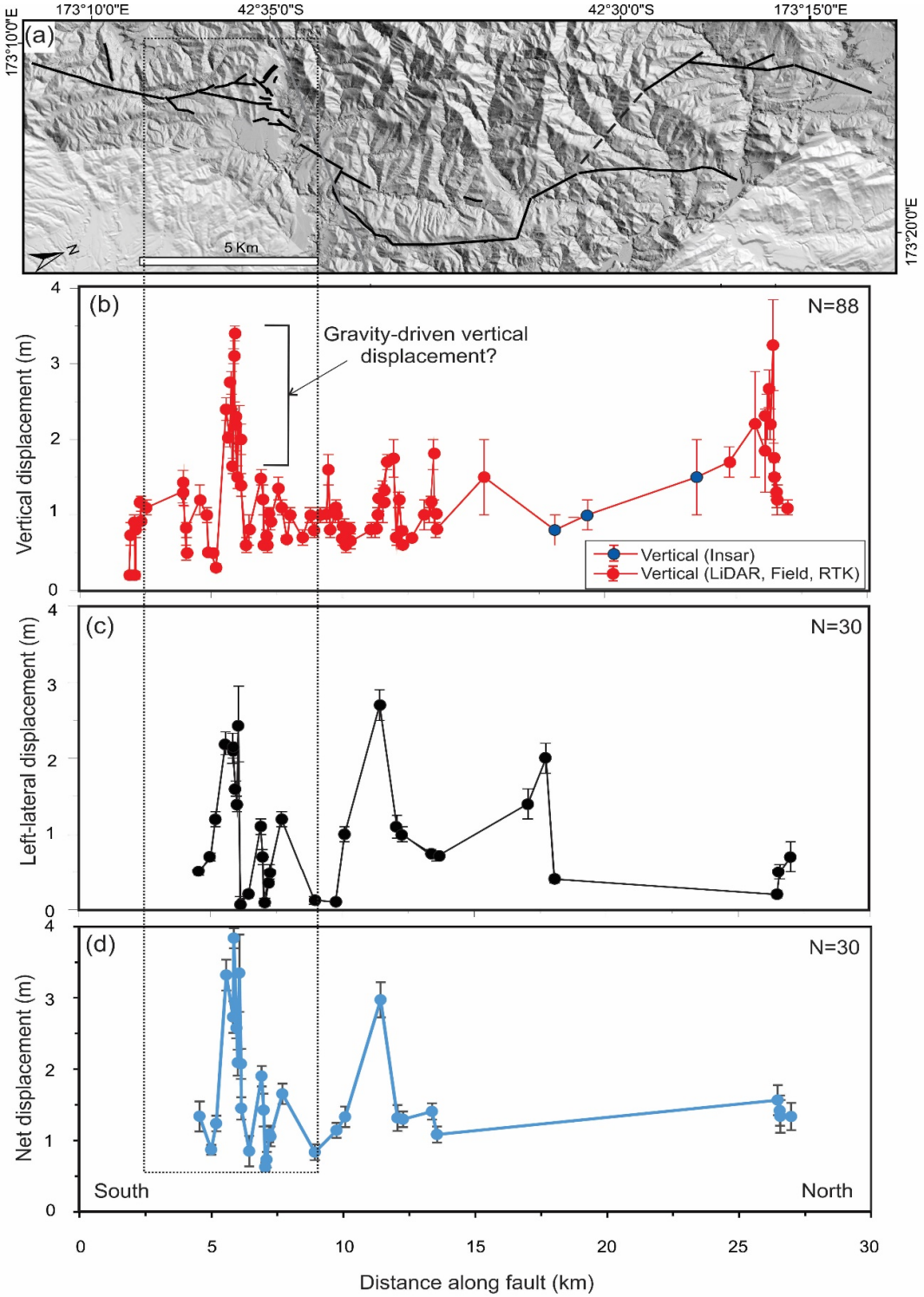

Figure 4.1: Summed vertical (b), sinistral (c), and total (d) displacements along the entire Leader Fault (a), where peak displacement in the study area occurs at The Waiau Wall. Study area is marked by a dashed line (after Nicol *et al.,* 2018).

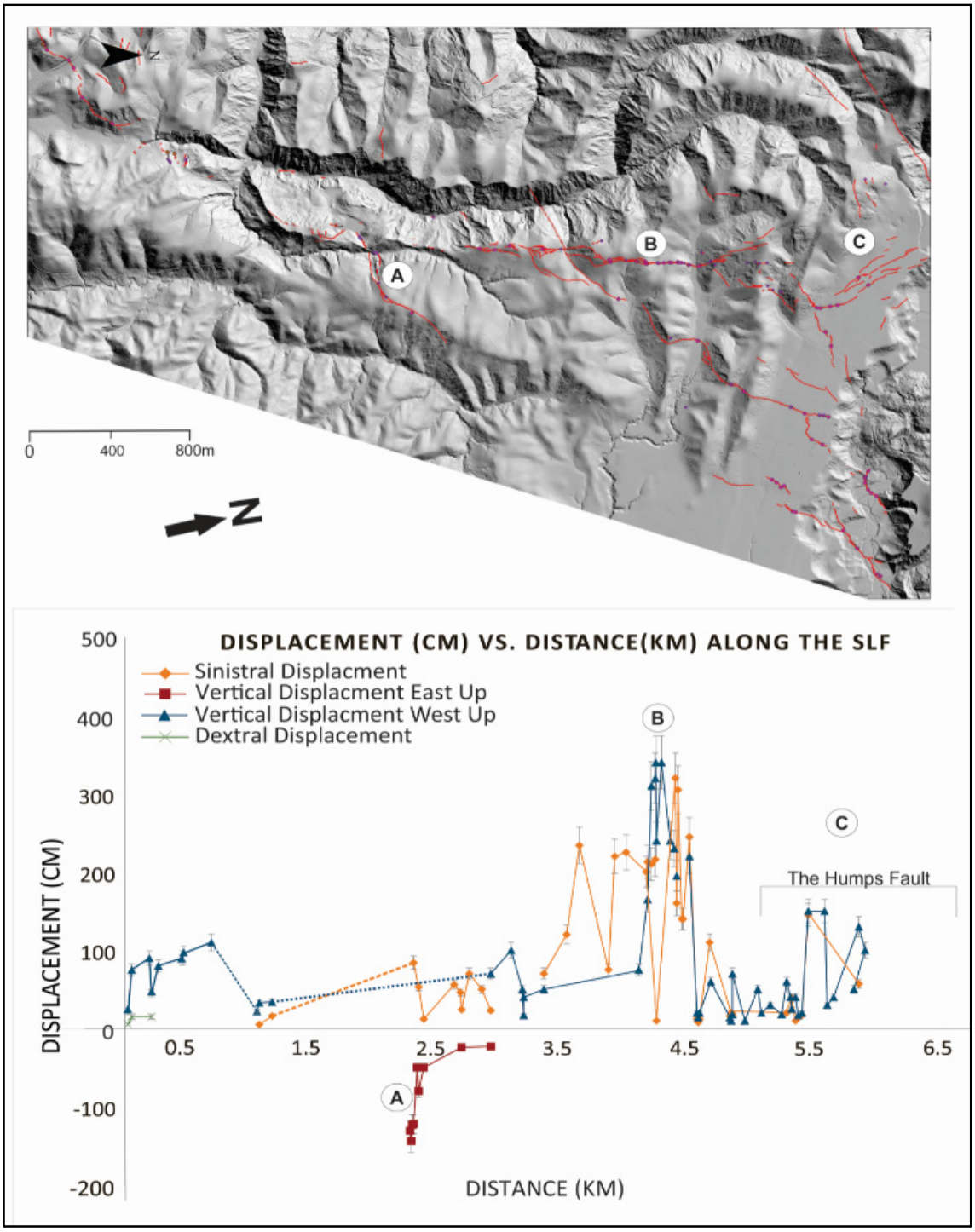

Figure 4.2: Summed sinistral, dextral and vertical displacement across the SLF. Dashed lines correspond to the approximate location of displacements on the graphs. Displacements for the HF are not included.

4.2.1 Bedding-Parallel Faults

As previously proposed in Chapter 3, a group of surface ruptures from the 2016 earthquake are parallel to, or sub-parallel to, bedding. In general, the bedding-parallel traces exhibit less

over-all displacement than the steeply-dipping faults, and display a higher ratio of vertical to strike-slip displacement with a predominantly dip-slip sense. These faults are typically thrusts, with dips ranging from 25-40 °. Striae data and stereonet plots for bedding-parallel faults have been plotted for five locations (locations 1,2,3,4, and 5 on Fig. 4.3). The only striations found in the field were documented on the Quarry fault (location 2, Fig 4.3) and formed along the contact between the Waimea Formation and Amuri Limestone. Others could be calculated where vertical and horizontal displacement, and strike and dip of a fault were known.

At the southern end of the study area in the region of the Leader Road (location 1 on Fig. 4.3), the earthquake ruptured a thrust fault referred to here as the Leader Road fault which forms the contact between the Greta Formation and Torlesse basement. The fault is orientated at ~055/25 ° NW and is approximately parallel to bedding of the Greta Formation at ~045/32° NW. Immediately north of the Leader Road (~50m) fault slip is dominated by vertical displacements with a V:H of approximately 10:3, where lateral offset is dextral. At location 1, the fault steps to the left, and changes orientation to 068/45°NW. The calculated rakes here are steep (~76°), and stereonet "A" in figure 4.4 shows a predominantly dip-slip fault with a dextral component. S_1 (shortening) is calculated at 154/16°, and S_3 equals 058/80° (Fig. 4.4A). The slip vector arrow (location 1, Fig. 4.3) trends at ~140° at 85° to the strike of the bedding-parallel fault.

Further north in the region of location 2 (Fig. 4.3), a surface rupture defines the top of the Amuri Limestone Formation. This fault cuts through a quarry and is here referred to as the Quarry fault. The fault follows the contact of the Amuri Limestone and cuts through a valley and up a ridge forming a "v" in map-view. The fault has an orientation ranging from 194/25°W – 240/30°NW. In the quarry, the fault is parallel to bedding of the Amuri Limestone, orientated at 191-200°/32-34°W. Interestingly, the fault here is upthrown to the east with a maximum vertical displacement of 1.22 m and a horizontal of 0.75 m sinistral. Given the eastside up and the westward dip locally this fault carried a normal component of slip with an average S_1 calculated at 83/15 °, and S_3 of 222/66 ° (Fig. 4.4B). The normal displacements are accompanied by the formation of fissures up to 0.2 m wide and 1 m deep, consistent with the view that locally displacement on this fault has been influenced by

gravitational failure into a deeply incised valley west of the quarry (see the discussions section of this chapter).

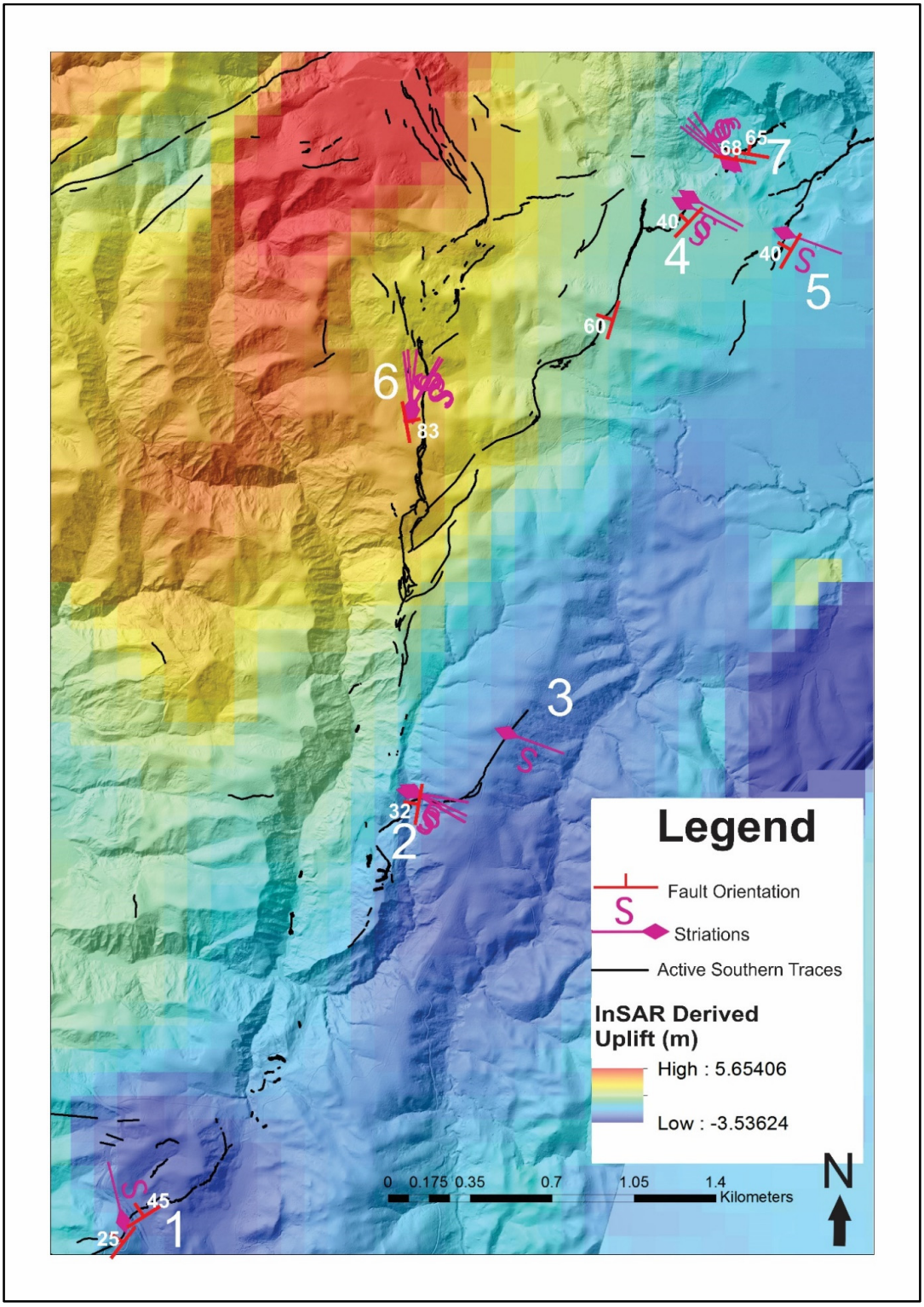

Figure 4.3: Annotated map of the SLF at the Woodchester Station overlain on an InSar uplift map after Hamling *et al.* (2017). Slip vectors are recorded for locations 1-6 from striation data. Bedding-parallel or sub-parallel faults are recorded at locations 1-5. Steeply-dipping faults are marked at locations 6 and 7.

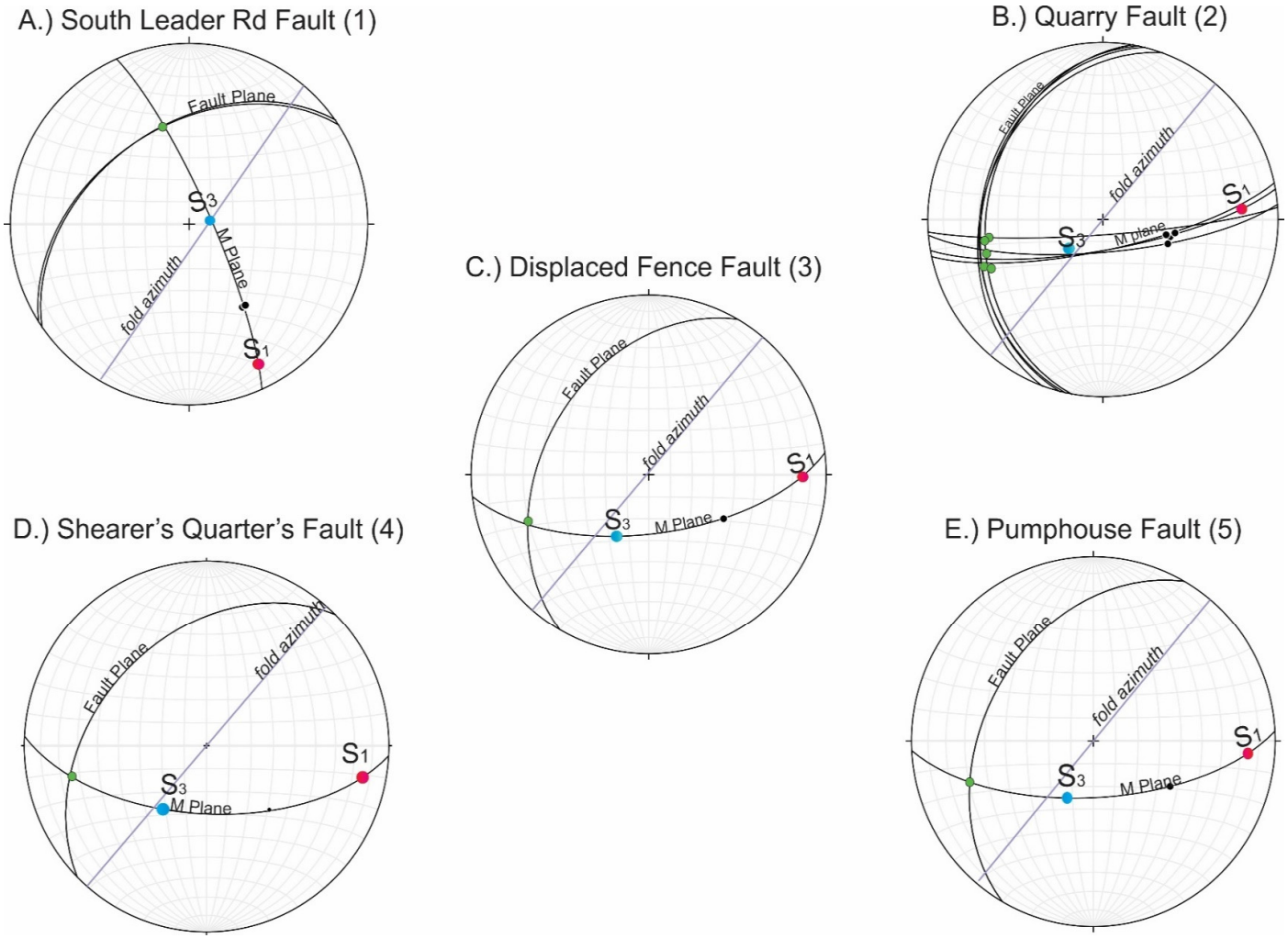

Figure 4.4: Lower hemisphere equal area stereonet projections for 5 bedding-parallel/sub-parallel locations as illustrated in Fig 4.3. Fault planes and movement planes are labelled, and rake and striae measurements are shown in green arrows. A) depicts the South Leader Road fault at location 1, B) the Quarry fault at location 2, C) the displaced fence fault at location 3, D) the Shearer's Quarters fault at location 4, and E) the Pumphouse fault at location 5.

Figures 4.4C and 4.5 show a displaced sinistral fence 0.52 km along the same fault trace as the Quarry fault. It is assumed that this fault follows the contact of the Amuri Limestone and Waimea Formation, however, no outcrops were located to confirm this. The fault strikes at 210° and dips ~40°. There is a measured 0.23 m of sinistral offset, 0.24 m of vertical up to the east, and a calculated rake of 47° with an oblique thrusting movement sense. Measurements here were taken at the top of a ridge on the flats where the influence of gravity is interpreted to be significantly less (than at location 2), and the equivalent amounts of lateral and vertical displacement convey near equal amounts of dip-slip and strike slip on the stereonet. S_1 is calculated at 90/13 ° and S_3 at 207/59 °. The slip vector here moves in the same direction as the vector for the Quarry fault.

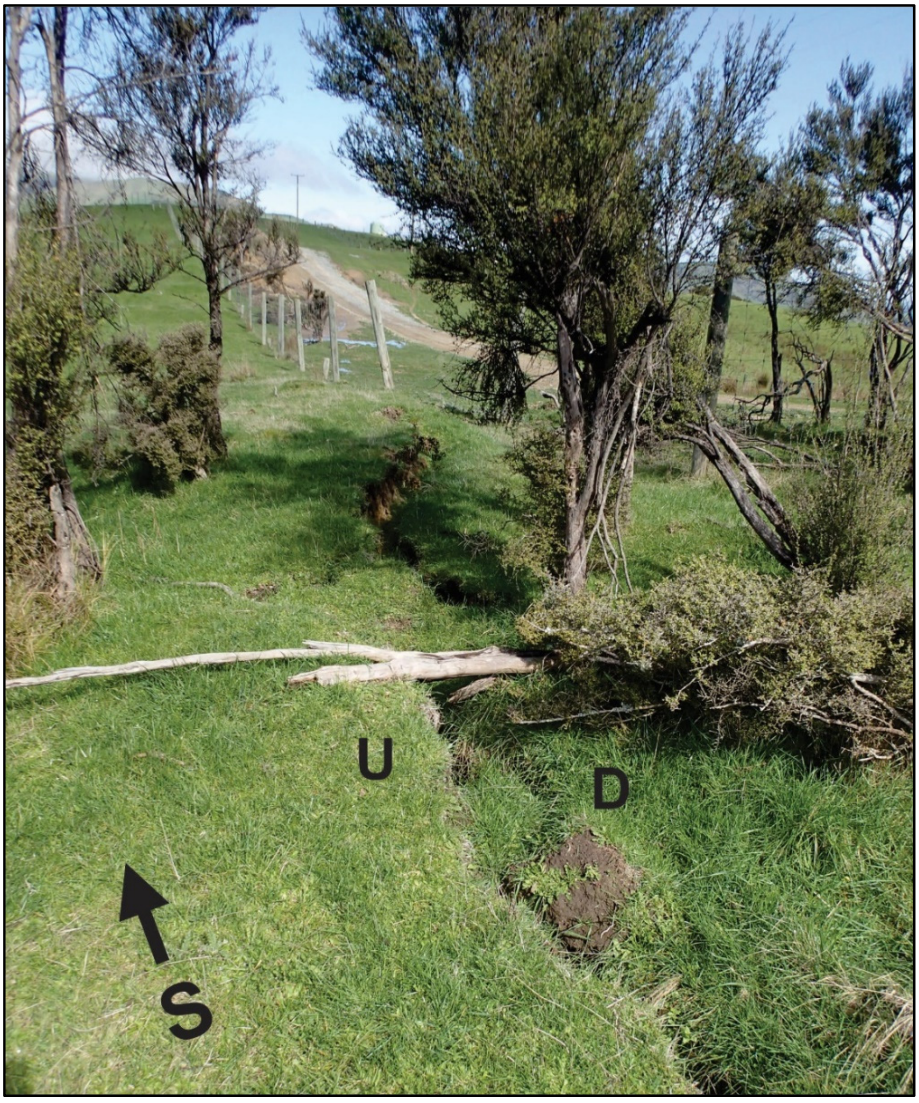

Figure 4.5: Annotated photograph of the displaced sinistral fence with an upthrown to the east referred to in figure 4.3 location 3 and figure 4.4C.

The Shearer's Quarters fault (Fig. 4.4D) is an inferred bedding parallel between the Greta Formation and Motunau Group (the Waimea Formation). There is no outcrop exposure on the high terrace surface where the fault is located, and so the contacts were extrapolated from the structural data measured in the river bed. The fault has a strike and dip of 225/40° W, with the west side up. The dip here was measured using Ground Penetrating Radar (GPR) and was imaged down to 6m (Hoare, 2017). Rakes were calculated to be 40° and sinistral offset is slightly larger than vertical (0.35 to 0.2 m). Stereonet "D" in Fig. 4.4 portrays near equal amounts of strike-slip and reverse motion. S_1 was calculated at 99/12°, and S_3 at 211/57°. Slip vectors are oriented at 115°, and indicate oblique sinistral reverse motion. At this location, bedding-parallel faults are cross cut strands of the HF. The discussion section of this chapter will address the local variations in slip sense and fault orientation within this intersection zone.

Four hundred and thirty metres to the west of the Shearer's Quarters fault (Fig. 4.4E), a fault that destroyed a pumphouse is sub-parallel to bedding between the Eyre Group and Greta Formation. Similar to the Shearer's Quarters fault, the Pumphouse fault also sits on the high terrace and structural data were extrapolated from measurements in the riverbed. The fault is oriented at 210/40°W, with vertical and horizontal displacements of 0.2 and 0.17 m, respectively. Rake of slip on the fault plane was calculated at 50°, with a S_1 of 093/14 °, and the S_3 at 210/61°. The fault accommodates oblique reverse sinistral slip with a vector that is sub-parallel to that of the Shearer's Quarters fault.

4.2.2 Steeply Dipping Faults

The steeply dipping faults (located as "6" in Fig. 4.3) are described from The Waiau Wall. At this location the fault strikes N-S, orientated at 354/85 ° to the east (Fig 4.6; Fig 4.3; location 6; Fig 4.7A). Displacement at The Waiau Wall is oblique slip with vertical and sinistral displacement are 3.5 and 3 m, respectively. The fault here is upthrown to the west. The vertical displacement is the greatest displacement in the study area, and may very well be include gravitation slip of ~2 m (Nicol *et al.*, 2018). The sinistral measurements were also recorded at sites where roads, fences, and streams were displaced, and do not exhibit the same gravitational exaggeration. Additionally, the presence of reidel shears that are only found around The Wall locality indicate a predominance of sinistral strike-slip faulting. The steep eastward dips (~83° E) on The Waiau Wall suggest that it is an oblique sinistral normal fault, however, in places the fault scarp also displays reverse component in the form of a toe

thrust, with a maximum summed scarp height of ~165 cm. The toe thrust (described in Chapter 3) is discontinuous and strikes both in N-S and NE-SW directions, occurring both on assumed bedding-parallel traces and immediately beside (1-5m) steeply-dipping fault planes.

The striae on the principal slip surface at The Waiau Wall remained in-tact in the months following the Kaikōura earthquake, and for the purposes in this study were measured along 9 m of the fault plane in March 2017. They were contained within the Greta Siltstone and their orientations were easily recorded before the fault scarp experienced significant degradation (Figs 4.6). These data permitted a detailed range of striae to help determine slip vectors, and for the purposes of this study have been divided into two groups; within 1-1.5m of the surface, the rakes are relatively shallow (22-45°) and deeper on the fault plane, they steepen. The striae closest to the talus at the base of the scarp have a rakes of 65°. An approximate location of the transition from shallow to steep rake angles is shown on figure 4.6A and occurs over a distance of 10's of cm. The change in rake of the striae suggests that the rupture initiated as mostly strike-slip, and changed to predominantly dip-slip. Average S_1 and S_3 values were calculated for these two groups of striations with shallow rake angles producing an average S_1 of 305/33° and S_3 of 043/18°, while steeper striae produce an average S_1 of 279/45° and S_3 of 060/21°. The origin of this change in fault slip orientation is examined further in the discussion section of this chapter.

The variation in slip vectors plotted for The Wall (173-215°; Figs 4.3, 4.6 & 4.7A) also reflect the changes in striae. The shallow striae indicate oblique sinistral strike-slip, while the steeper rakes are oblique normal. This normal component is likely driven by gravitational exaggeration and will also be examined in the discussions section of this chapter.

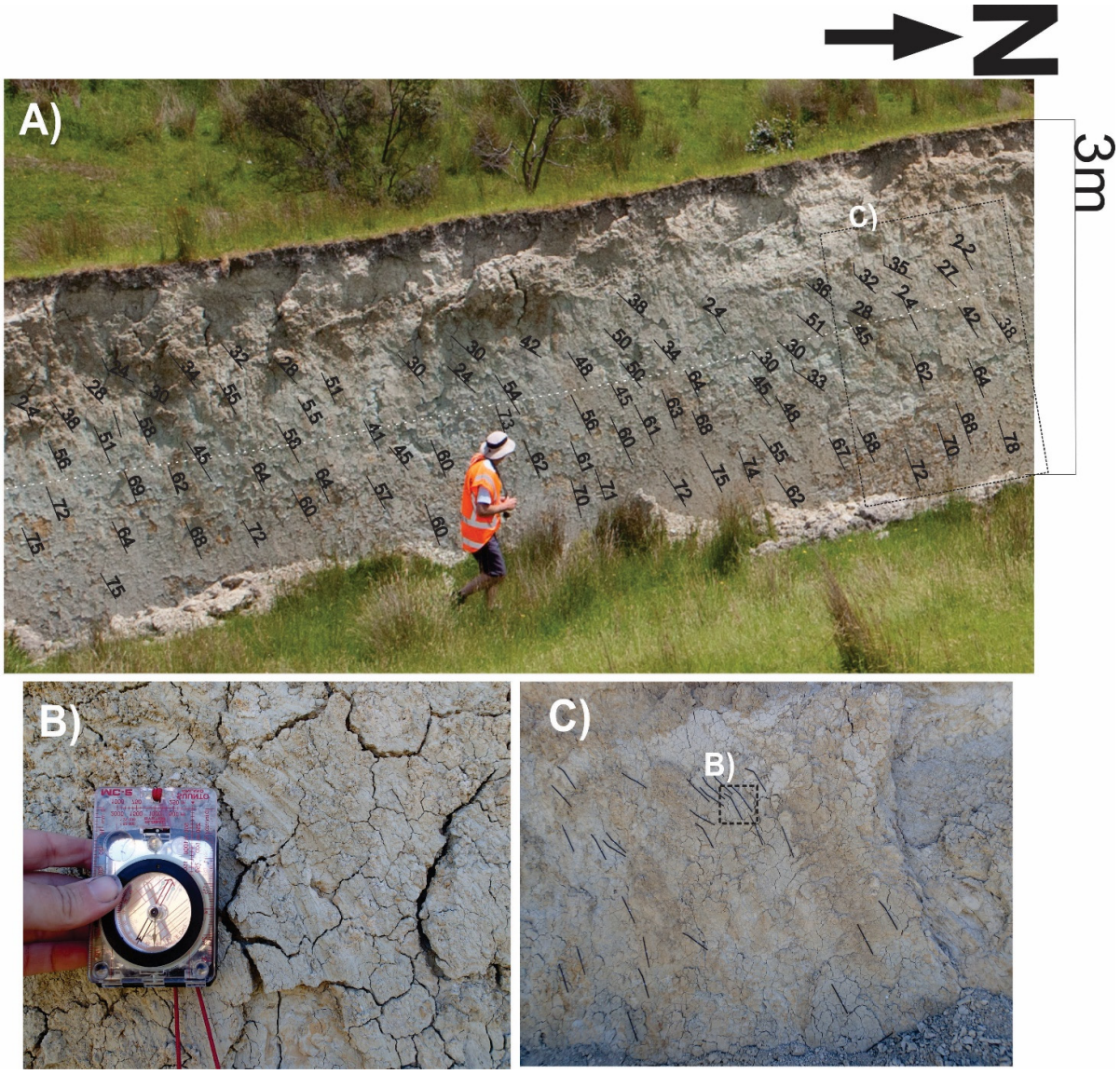

Figure 4.6: Striations along a ~9 m section of The Waiau Wall fault plane. A) annotated photograph of striae where the white dashed line shows the approximate location of the transition from predominantly strike-slip to predominantly dip-slip. The black dashed box is the area shown in C. B) Photograph of striae that show the curvature from shallow to steep rakes. C) photograph of straws that were stuck to The Wall using blue tac to capture the striae orientations and their variation on the fault plane. The black dashed box shows the location for B).

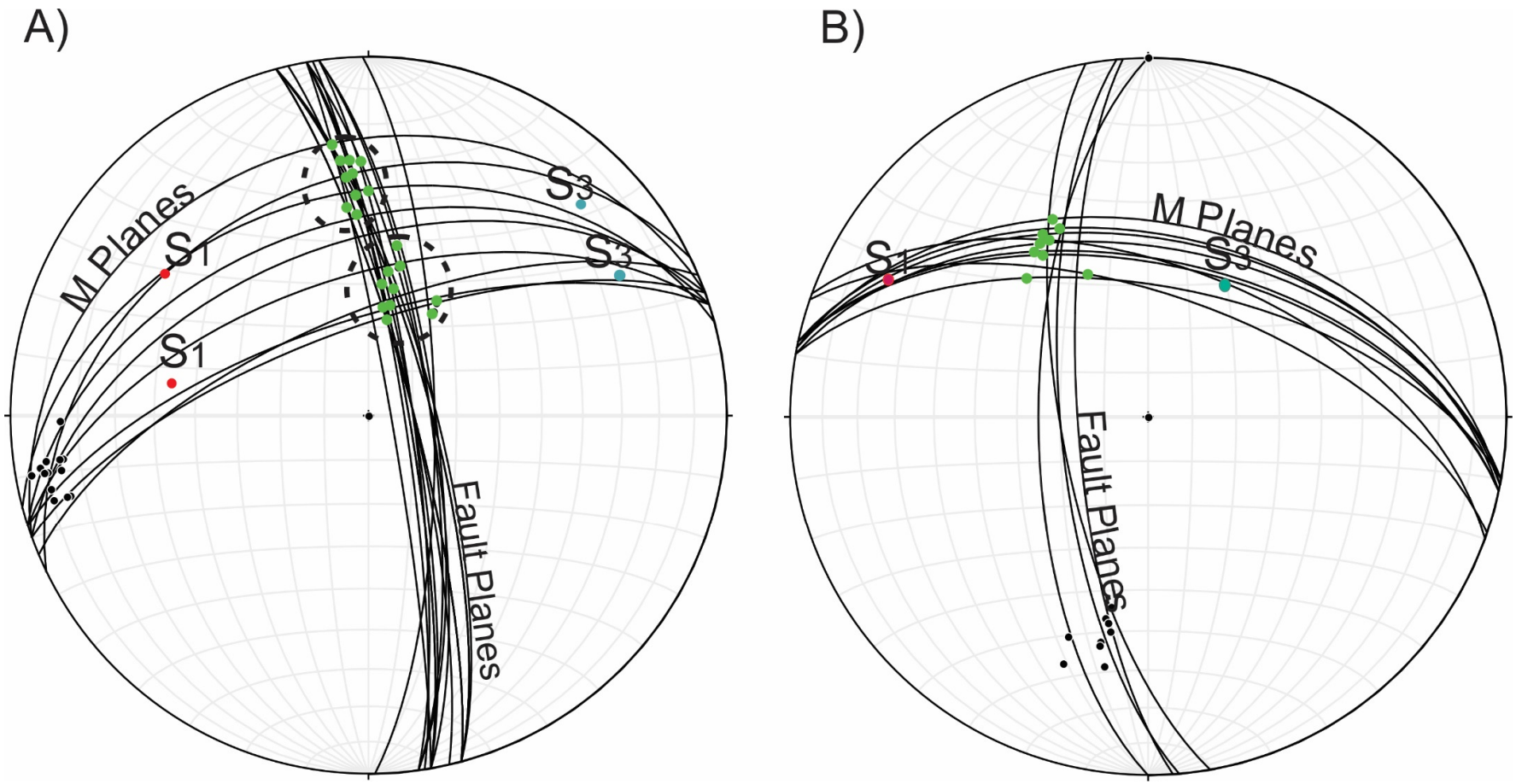

Figure 4.7: Lower hemisphere equal area stereonets for the fault plane and striae at The WallLocality (A). Rakes plotted for The Waiau Wall show two groups; low rake angles (~22°-45°), and high rake angles (~50°-68°) circled dashed black. S_1 and S_3 have been plotted as averages of these two groups. B) Rakes plotted for the Trench fault with S_1 and S_3 averages.

4.2.3 The Humps Fault (HF)

Part of the HF was mapped in the northwest corner of the map area, where the fault traces have an east to northeast strike and strike-slip is predominantly dextral. Displacements for the entire HF are shown in Figure 4.8 along with the horizontal (dextral), vertical and net slip. These displacements are illustrated at the trench locality (marked as "7" in Fig. 4.3) where the vertical displacement is ~1 m, and dextral displacement ~0.5 m forming a V:H ratio of 2:1 (Fig. 4.9). The average strike and dip along the fault plane where these displacements were measured is 292/65° NW.

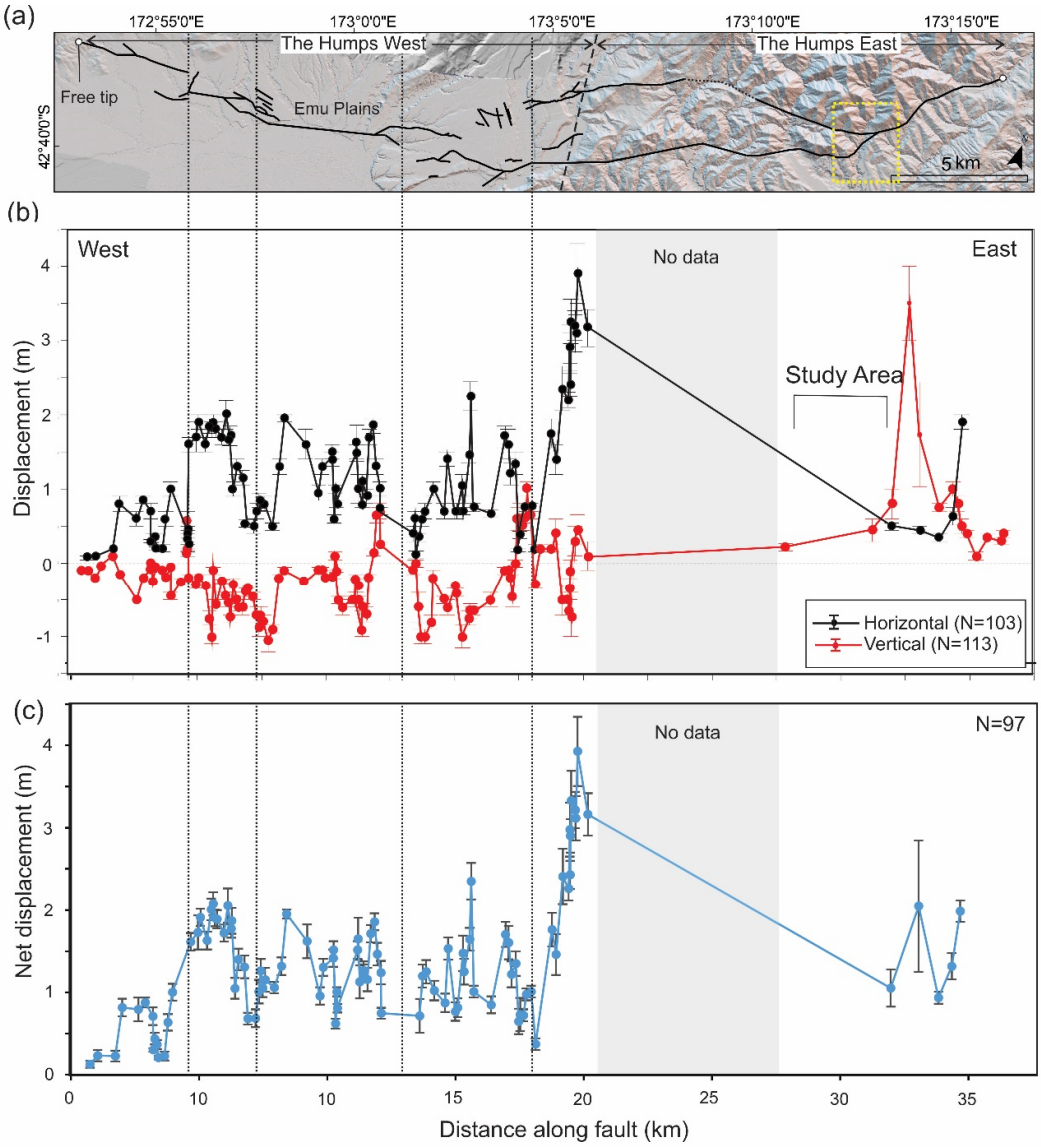

Figure 4.8: Along-strike displacement trends for the HF after Nicol *et al.,* 2018. The study area is marked by a yellow box in (a).

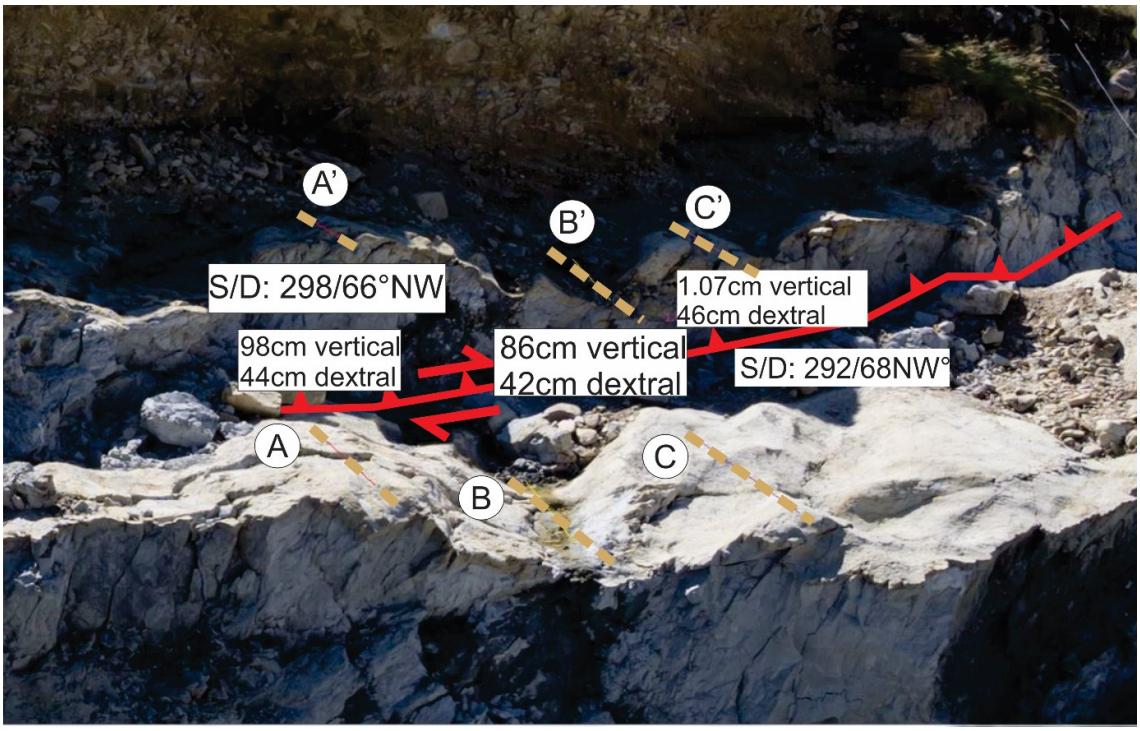

Figure 4.9: Bedrock fluted strath surface showing displacement along a section of the fault plane. Beige dashed lines indicate the piercing points of the fluted strath which were used to measure displacement of A, B, and C.

Striation data were found in a small section of fault gouge approximately 10 m downstream from figure 4.9 three months after the Kaikōura earthquake. At this location, the HF strikes at 282 ° and dips 55-68° to the north. The rakes observed here are steep and have an average of ~65°, which is consistent with a higher vertical to strike-slip displacement sense measured from the displaced ground surface. An average S_1 was calculated at 297/19°, and S_3 at 033/53°.

As previously discussed in Chapter 3, the Trench fault changes orientation to the east where it has an azimuth of ~055 ° and inferred dip of ~45°. This swing in the fault strike also coincides with a bedding contact between the Greta siltstone and Motunau formation, and the fault is inferred to follow this contact northwards beyond the study area.

4.3 Kinematic Model

Kinematic models are powerful tools for fault analyses and for the study of faulting processes. They may also help us to understand how strain is accommodated across the SLF, of which the geometries and displacements are complex. A kinematic model for the SLF (Figs 4.3 & 4.10) was produced using the magnitude, slip orientations, and slip vectors along the fault trace. The kinematic model presented is primarily tectonic although it is

acknowledged that faults are locally utilized for gravitational failure. From the displacement profile and fault trace maps, it seems that fault strike and dip influence the magnitude and sense of displacement.

The kinematic model for the SLF depicts three main types of movement; reverse dextral, reverse sinistral and normal sinistral. The most common slip sense for the bedding-parallel faults is reverse/dip-slip with a sinistral component (the Quarry fault, the displaced fence fault, the Shearer's Quarters fault, and the Pumphouse fault; table 4.1). Bedding-parallel faults appear to a least partly use planes of weakness along lithological boundaries of Cenozoic strata, and these faults may have accommodated flexural slip and associated folding in the cover sequence (see Chapter 3). Where these bedding-parallel faults occur, their dips are generally low, strikes are to the NE-SW, and the predominant slip sense is dip-slip (slip vectors for bedding-parallel faults form rake angles of ~50-82°). As shown in figure 4.1, if we exclude the Quarry fault, the slip vectors and senses of bedding-parallel faults are consistent with one another. The average S_1 for these four equates to 91°, which is similar to the regional PHS (~120 +/-19 °; Nicol *et al.,* 1992; Nicol *et al.,* 2018), and the maximum horizontal compressive stress of ~115° +/- 15° for dextral strike-slip faults of Canterbury (Sibson *et al.*, 2011; 2012).

Where the SLF dips steeply, it strikes N-S (e.g.; The Waiau Wall). At the ground surface, the sinistral component is accommodated by the steep faults, while an important component of shortening is accommodated by folding and a discontinuous toe thrust. The observed oblique sinistral displacement at The Wall is also generally consistent with the regional PHS direction. These two styles of faulting across the SLF help to explain why the faults formed in the 2016 rupture are spatially distributed across a rupture zone up to ~3 km wide in Woodchester area. It is inferred that both steep faults and the bedding-parallel faults utilize pre-existing planes of weakness. The steep SLF utilises a pre-existing structure with 600-800 m of throw (see Chapter 3) which may have utilised steep basement fabric in Torlesse Supergroup rocks, while bedding-parallel faults are using bedding planes in Cenozoic strata to accommodate flexural-slip and associated near-surface folding.

Table 4.1: Fault characteristics and slip vectors for the 7 faults described in text and Figure 4.3

Location (Fig 4.3)	Fault Classification	Horizontal Displacement (m)	Vertical Displacement	Approximate V:H ratio	Fault Sense	Side Up	Fault Strike (°)	Fault Dip (°)	Slip Vector Azimuth (°)	S_1 (°)	S_3 (°)
1	Bedding-Parallel	0.26	0.81	10:3	Reverse Dextral	W	65°	45°NW	~140°	154/16°	58/80°
2	Bedding-Parallel	0.75	1.22	12:7	Reverse Sinistral	E	194-200°	25-35°W	~100-122°	83/15°	222/66°
3	Bedding-Parallel	0.23	0.24	1:1	Reverse Sinistral	E	210°	40°W	~120°	90/13°	207/59°
4	Bedding-Parallel	0.35	0.20	2:3	Sinistral Reverse	W	225°	40°W	~115°	99/12°	211/57°
5	Bedding-Parallel	0.17	0.20	1:1	ReverseSinistral	W	210°	40°W	~115°	93/14 °	210/61°
6	Steeply-Dipping	2.01	2.95	3:2	Normal Sinistral	W	354°	85° E	~173-215°	279/45° & 305/33°	033/53° & 060/21°
7	Sub-parallel/ HFZ	0.45	0.9	2:1	Reverse Dextral	N/NW	292°	65°N	~140°	297/19°	033/53°

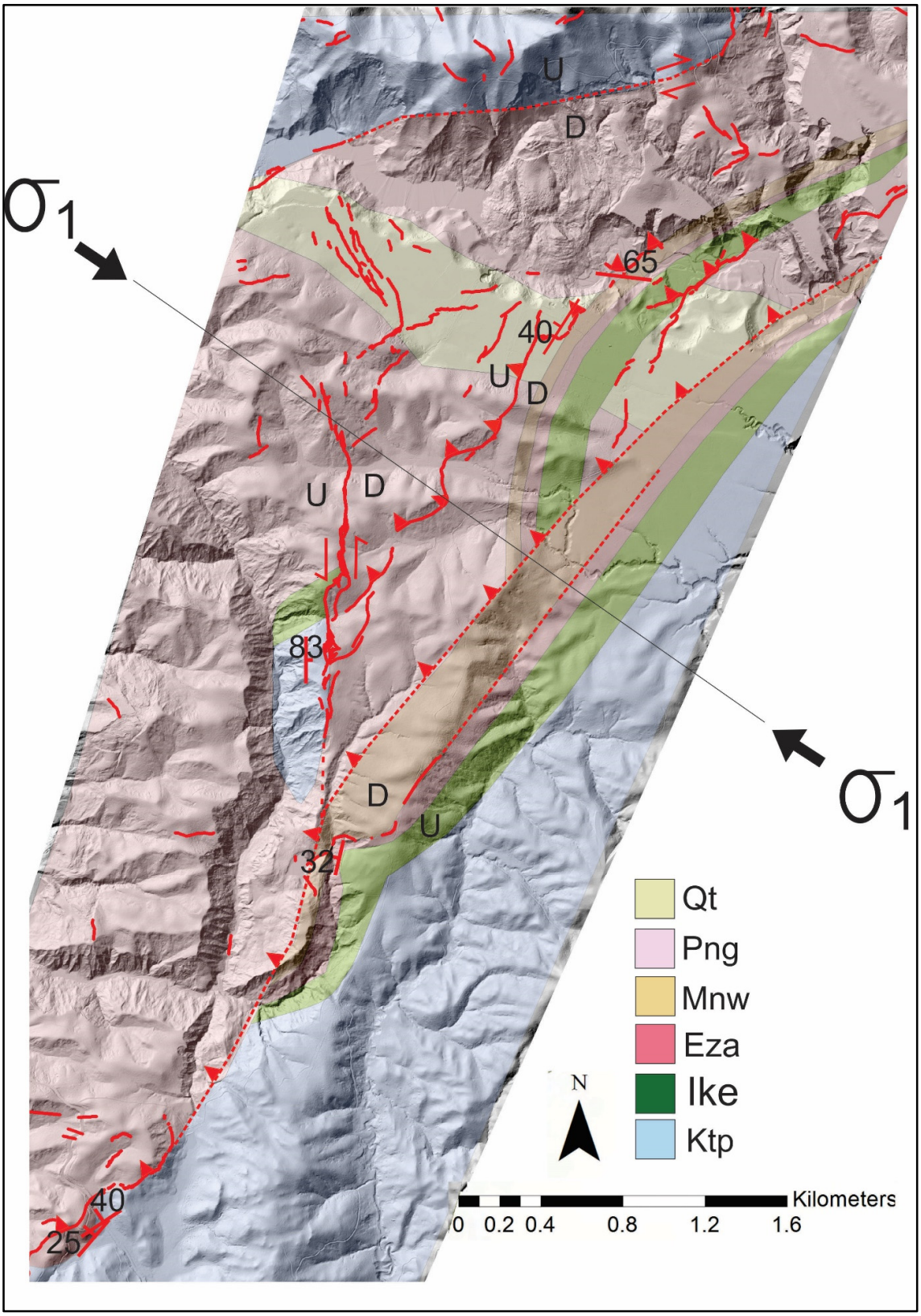

Figure 4.10: Generalized schematic of faulting with respect to host geology. The σ_1 value used here is an average of all S_1 values (105°) reported in Table 4.1.

The lowest S_1 values are for the Quarry fault and likely reflect a gravitational component of slip and/or slip partitioning. The steep angle of rakes, deep tension cracks, and high vertical displacements characteristic of this location are indicative of normal faulting and extension. About 500 m west of the Quarry Fault, there is significant landsliding and slope failures which has diverted stream flow to the west and produced a pressure ridge in the valley up to 1 m in height. Maximum vertical east-up displacement on the Quarry Fault (1.22 m) roughly corresponds to the height of the pressure ridge consistent with the model that the fault was locally utilised for gravity failure (Fig. 4.11).

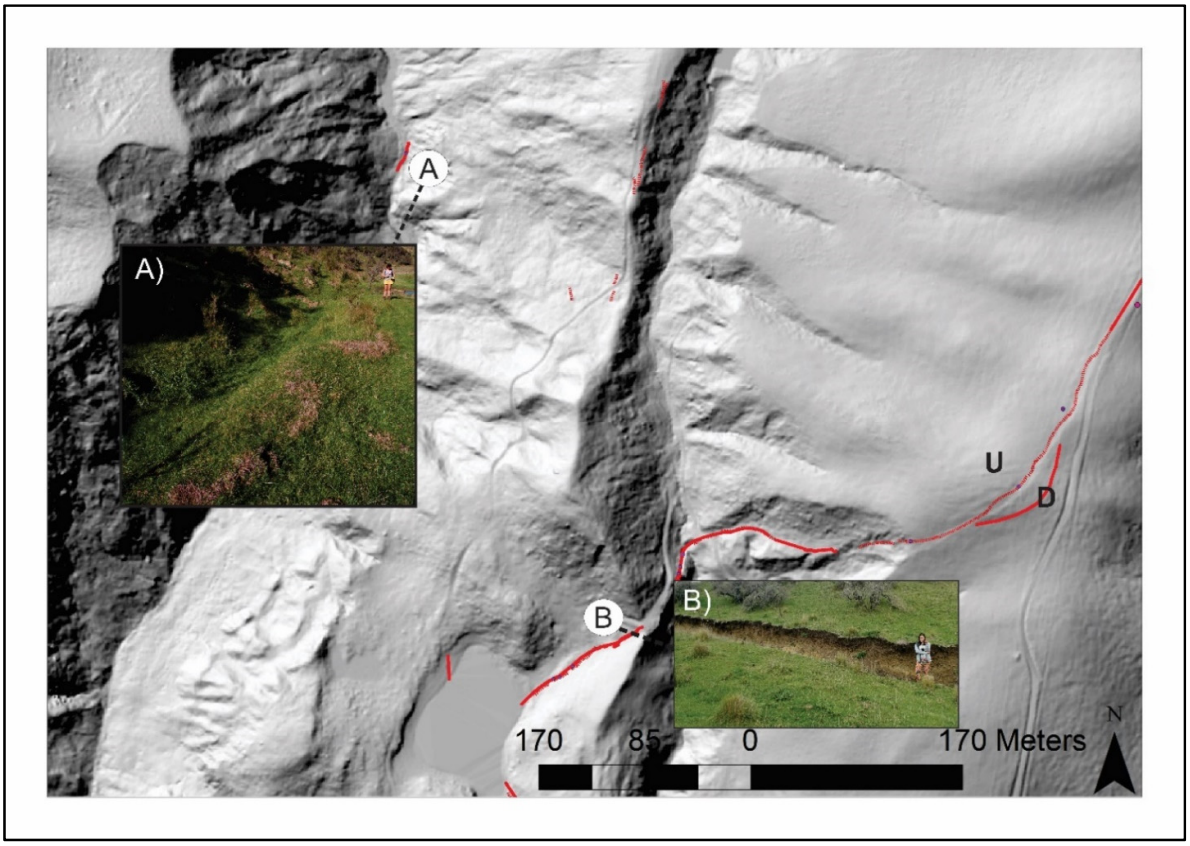

Figure 4.11: Hillshade LiDAR with 0.25 m resolution showing the location and geometry of the bedding-parallel Quarry Fault (red lines). A) A compressional roll in the river bed which is ~0.70 m in height. B) Extensional fault scarp up to ~1.22 m in height. Dotted lines connect photographs to their approximate locations.

There also seems to be a component of strain partitioning; although the sense is predominantly reverse, some of the deformation was expressed as normal dip-slip. While the reasons for strain partitioning are not always clear, this mechanism is more likely to occur on shallowly dipping faults, and the degree of partitioning depends on the strength of the host rock (Barnes *et al.,* 1998; Jarrard, 1986; McCaffrey, 1992). The striations found on the fault

plane occur in the Waimea Formation, which is mainly comprised of mechanically weak poorly-moderately indurated, loosely consolidated sandy siltstone (Browne and Field, 1985).

4.4 Discussion

Despite the complicated geometries of the Kaikōura 2016 earthquakes, the magnitude and nature of displacements reported for the SLF are consistent to the stress fields reported across North Canterbury. Figure 4.10 depicts shortening across the SLF trending NW-SE, which is consistent with the findings of Nicol *et al.,* (1992) for shortening axes across faults in Wairapa, North Canterbury. This orientation is also in line with Cowan's (1992) study, which concluded that shallow faults in the Porters Pass Amberely Fault Zone and Canterbury foothills demonstrate contractional axes oriented in a WNW fashion.

The slip vector data presented in this Chapter are supported through both studies of Wallace *et al.,* (2012; 2007) for strain axes in North Canterbury, wherein geologic data and GPS velocities were used to model principal strain rates. In their 2007 study, the principal contractional axes across North Canterbury produced a $S_1 = 97° \pm 8°$; however their 2012 study reported S_1 at $77 \pm 20°$. Both data sets fit well within what has been observed for bedding-parallel structures along the SLF; the reverse sinistral structures have an average S_1 of 90.5°, with the largest $S_1 = 99°$ (The Shearer's Quarters fault), and the smallest $S_1 = 83°$ (the Quarry fault). The variation in the models presented by Wallace *et al.,* (2007; 2012) are all within range for the different fault segments of the SLF, and appear to also reflect localised strain partitioning within the North Canterbury Block. Averaging the S_1 values of the South Leader Road fault (~154°), The Wall fault (~99° and ~125°), and the Trench fault (117°) with the reverse sinistral bedding-parallel faults results in an average S_1 of 107°. This S_1 value intersects the azimuth of the anticline first described in Chapter 3 nearly perpendicularly, and supports a model of bedding-parallel faulting produced by flexural-slip folding.

In general, the stress fields for the SLF are consistent with overall NW-SE compression axes reported in all geologic studies in North Canterbury within the last 30 years (Cowan, 1992; McMorran, 1991; Wallace *et al.,* 2007; 2012; Nicol *et al.,* 1992; Sibson *et al.* 2011; 2012). Although the slip vectors here fit reasonably well, there are inconsistencies and problems within this kinematic model, especially with respect to The Wall fault and the Quarry fault. Slip on these faults appears to have been influenced a significant component of gravitational

collapse of ridges into valley floors hundreds of meters lower (Fig 4.11). These gravitational collapses are mainly landslides which range in size from 10's of m^2 to 10 km^2.

For the Quarry fault, compressional rolls in the riverbed are similar in magnitude to vertical displacements on the fault itself, consistent with westward slope movement as least partly accommodated on the bedding-plane fault. Miller and Dunne (1996) demonstrate high regional compression combined with high topography can cause tension at ridge tops and compression within valleys.

The gravitation exaggeration on The Wall is estimated to be as high as ~2m (Nicol *et al.*, 2018). The Wall scarp itself is normal; it dips at 85° and has a group of rakes that plot as high as 75°. However, the striations towards the top of the fault scarp have rake angles as low as 20° that indicate an initial strike-slip event. These two groups of striations seemed to have recorded two 'events'; initially strike-slip, with a latter dip-slip motion that produced much of the elevated vertical displacements recorded. It also remains possible that the high vertical displacements at The Wall are tectonic, and were induced by late-stage slip in the bedding-parallel thrust faults. For such a model, rupture on The Wall initiated movement on the low-angle thrust faults, which, in turn, required dip-slip normal faulting to accommodate deformation. This idea is supported by the findings of Wesnousky (2008), which suggest the front of large laterally propagating earthquake ruptures may trigger slip on adjacent faults.

The striae data on The Wall opposes the striae data on the Kekerengu Fault, which instead of an initial strike-slip event followed by a dip-slip event, suggests an initial oblique-reverse mechanism followed by a strike-slip event (Kearse *et al.,*2018). For the Kekerengu Fault, striae formed an average initial ~15° oblique-reverse pitch and transitioned into a more horizontal orientation over 0.5-2 m. This curvature has allegedly recorded an initial, short phase of dextral-reverse followed by a longer displacement of nearly pure dextral strike-slip (Kearse *et al*. 2018). Unlike The Wall fault example, the 'two phase' slip recorded on the Kekerengu Fault are primarily attributed to tectonic earthquake processes.

Both vertical and lateral displacements decrease around 4.5 km along the fault displacement profiles (Fig. 4.2), where the faults begins to splay in a complicated network as they approach the intersection of the HF. The sense and magnitude of displacement along these traces

becomes less obvious both in the field and on LiDAR. Around this location, the steeply dipping Waiau Wall faults terminate. Although it is expected that vertical displacement should increase to the north, the intersection of the HF around 4.5 km on the profiles may complicate the displacement data. The Shearer's Quarters and Pumphouse faults are examples of this, as both exhibit a slightly higher sinistral to vertical displacement (than on bedding-parallel faults south of the intersection zone). However, the striae, displacements, and slip vectors on the HF at Woodchester Station are consistent with each other and show oblique dextral faulting.

4.6 Summary

- Three main groups of faulting described in chapter three (bedding-parallel/sub-parallel along the SLF, steeply dipping faults contained within the Greta Formation, and sub-parallel steep faults of the HF) differ in slip sense and kinematics.
- For bedding-parallel/sub-parallel faults, slip occurs on weak bedding planes in Cretaceous-Cenozoic strata and is interpreted to accommodate flexural-slip folding. These faults are low-angle in nature, and can be broadly characterized as oblique thrusts.
- Slip on the N-S steeply-dipping is oblique sinistral and down to the east. Movement occurred on a fault with as much as 800 m of total vertical displacement and may reactive or use a steep N-S basement fabric.
- Faults in the north of the study area that strike ENE and carry oblique dextral reverse slip are part of the HF.
- Vertical displacements at The Waiau Wall and part of the Quarry fault are elevated due to local gravitationally-induced slip on these faults. Inferred gravitational slip is supported by striations on The Wall fault plane which record an initial phase of strike-slip followed by mostly dip-slip.
- The orientations of the principal strain axes for surface rupturing faults in the study area are broadly consistent with the regional principal horizontal shortening of ~100-140°. Therefore, kinematics of the earthquake are consistent with contemporary GPS and geological timescale deformation.
- Striae on The Wall record an initial phase of strike-slip with a dramatic change to dip-slip. These results parallel the striae for the Kekerengu fault as reported by Kearse *et al.,* (2018).

5. PALEOSEISMIC ACTIVITY OF THE HUMPS FAULT AT WOODCHESTER

5.1 Introduction

The geological and kinematic studies presented in Chapters 3 and 4 of this thesis provide valuable insights into the geometry and slip of faults that ruptured the ground surface in the study area during the 2016 Kaikōura earthquake. To understand the seismic hazard of these faults, paleoseismic trenching and analysis of the relationships between the fault scarps and the landscape are necessary help to establish the rupture history of faults, including their recurrence intervals, slip and slip rates (e.g., McAlpin, 2009)

Paleoseismic investigations are generally time consuming, can be expensive (i.e., they often require significant time, labour, and resources), and may fail to convey valuable information even in the most ideal circumstances (McAlpin, 2009). Paleoseismic investigation in this study became viable when an active fault that ruptured in 2016 was exposed in the near sub-surface by river incision, although it was not in the original scope of this research. Rapid river downcutting occurred 4 months after the earthquake when the Leader Landslide dammed the Leader River to form a lake (informally named "Lake Rebecca", after landowner Rebecca Kelly) was breached. The overflow for the lake down-cut through a flight of fluvial terrace surfaces, exposing a part of the HF, and created a natural trench-like exposure of the fault where it crosses river terraces. In the months following this incision, the northern wall of the cutting (which contained the fault) was cleaned, flagged, logged, and analysed. Results of this 'trenching' are described in this chapter, in conjunction with geomorphic analysis of faulted landforms near the trench site, have been used to assess the following questions;

- What was the size and timing of events in the natural trench?
- Is there any evidence of previous surface rupture of the HF or SLF in the study?
- Are the prehistorical events from this study consistent with the paleoseismic characterization of the HF further west and what implications do these relations have for prehistoric rupture of the HF at the ground surface?

5.2 Leader River Site Description and Geomorphology

5.2.2. Geomorphology of the Leader River

The trenched fault scarp is located in the floor of the Leader River valley on Woodchester Station (Fig 5.2). The Leader River at Woodchester Station drains a relatively small

catchment, which includes parts of the Mount Stewart range. The river flows eastwards with an average bed gradient of ~1.5 m/km and has cut a flight of terrace surfaces and meander loops (Figs 5.1 & 5.2). For the purposes of this thesis, these terraces have been labelled from lowest to highest Qt1- Qt11. The lowest terrace (Qt1) was 1 m above the pre-earthquake active river bed, while Qt6 and Qt10 terraces are ~10 and ~60 m above the river bed, respectively.

In addition to the terrace surfaces the river valley near the trench site comprises landslides, alluvial fans and abandoned meander loops (Figs 5.1 & 5.2). The most notable of the area is the Leader landslide, which was formed in response to ground shaking during the 2016 earthquake and has an estimated volume of ~6 million m^3 (Massey *et al.*, 2018). The landslide reached within ~65 m of the trench side (see Figures 5.1-5.3) and dammed the Leader River immediately post-earthquake. Additional smaller landslides also formed in 2016, primarily along the northern side of the valley where they are located in close proximity to alluvial fans. By contrast, abandoned meander loops are most often preserved on the southern side of the valley (Figs 5.1-5.3).

The faults that ruptured the Leader River valley in 2016 displaced many of the terrace surfaces (Fig 5.1 & Fig 5.2) and appear to have had no discernible scarps prior to the earthquake (see section 5.5). Close to the trench site the fault ruptured the Qt6, Qt5, Qt3 and Qt2 terrace surfaces, although did not produce a clear trace across the active river bed. West of the trench site the 2016 rupture is buried by the Leader Landslide (Fig 5.2).

The geomorphology of the Leader River valley in the study area underwent significant changes during the earthquake and in the 12 months immediately post event. Figure 5.3 compares photographs of the riverbed before and after the 2016 event. In these photographs it is clear that the flow of the river was disrupted by the Leader Landslide which buried parts of the active channel. As a consequence of the landslide and the associated damming of the river, the river abandoned the large meander loop enclosing the Qt6 terrace at the trench site and, following dam breaching, cut a new channel along the newly formed fault scarp at the trench site. This incision produced the natural trench exposure studied here.

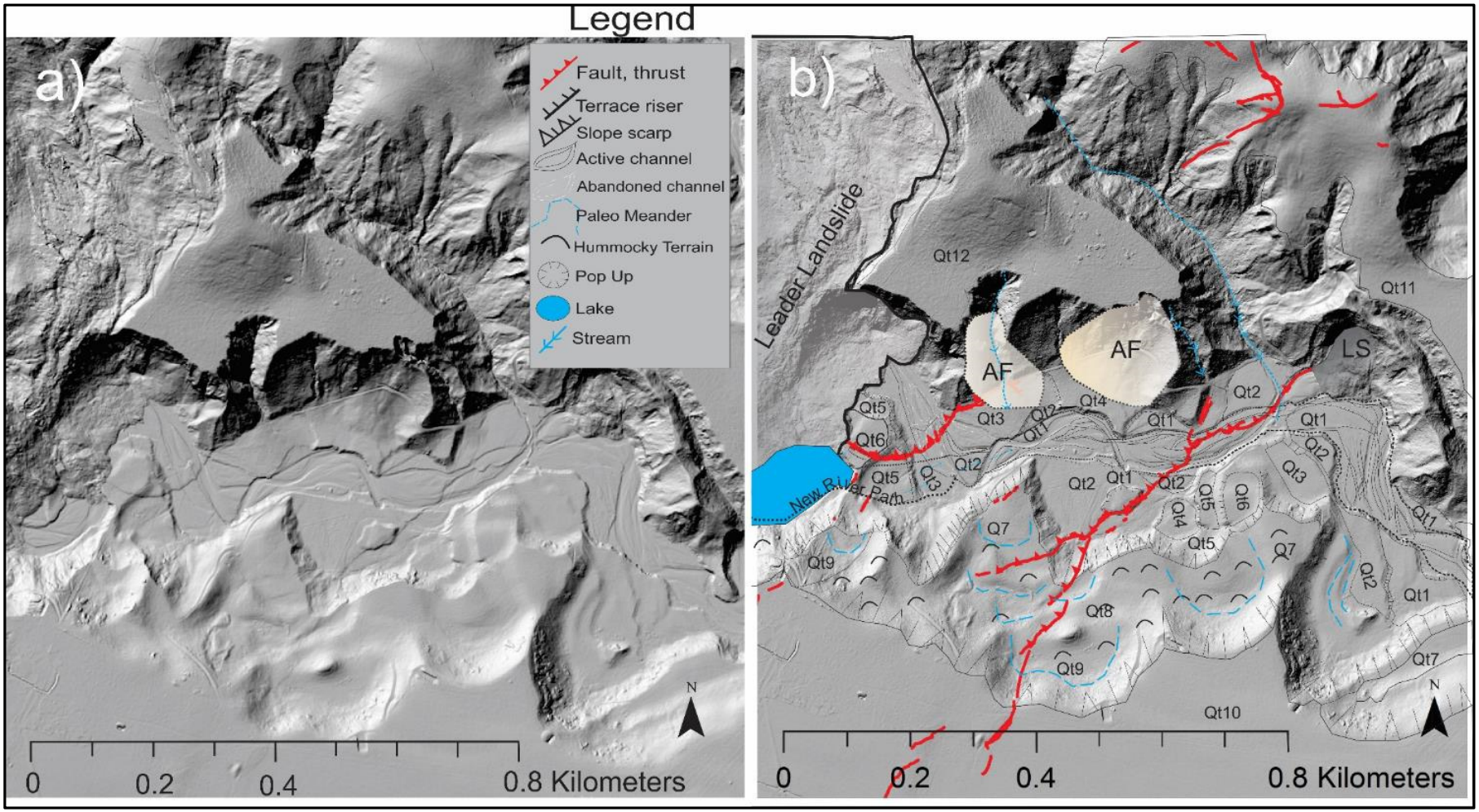

Figure 5.1: Hillshade model (0.25 m resolution) of Leader River: a) depicts the uninterpreted hillshade model and b) is an interpreted geomorphological map with correlated river terraces. LS= landslide, AF= alluvial fan.

5.2.1 Trench Site Geology and Fault Characteristics

The fault that runs through the trench site is not part of the SLF, and instead is considered part of the HF. The geometry of this fault was first described in detail in Chapter 3, while dextral and vertical displacements along the fluted bedrock terraces immediately west of the trench are described in Chapter 4. The fluted terrace outcrop is situated along strike from the fault exposed in the trench, which coincides with a location where the fault swings ~45° in strike. For these reasons, few paleoseismologists would elect to excavate a trench here, and as figure 5.4 shows, the units and geometries in this trench are complicated (for descriptions see section 5.3). At the trench site (Fig 5.2), the fault strikes at 282-290°, dips 55-68° N, and is contained within the Greta (Siltstone) Formation. Fifty metres northeast of the trench site the fault strikes at ~265° and dips 25-40° NW, approximately parallel to bedrock bedding along the contact between the Greta Siltstone and Motunau Group. Prior to river erosion the fault scarp was visible from the toe of the Leader Landslide to the active river bed forming a continuous trace for 342 m, although at the time of writing river erosion had decreased this length to 126 m (annotated in Fig 5.2). The scarp is prominent on the LiDAR, where it is visible as a 1.25 m high roll on the Qt6 terrace surface. A second fault scarp is visible ~360 m downstream of the trench site, where it is oriented at ~265°/40° NW, sub-parallel to bedding, and forms the contact between the Eyre Group and the Greta (Siltstone) Formation.

5.3 Trench Exposure

The location of the natural trench and its relationships to the geomorphology are shown in figure 5.2. The trench exposure is oblique to the fault trace and provides sub-surface information on the relationships between Miocene bedrock (Greta Stilstone), fluvial deposits, and colluvial wedges of uncertain origin (i.e. they could have formed due to degradation of the fault scarp following previous earthquakes or due to erosion of a terrace riser formed by river incision). Unit descriptions are provided in Table 5.1. No organic-rich material suitable for C^{14} dating was identified in these units, however a sandy silt sample (unit 6; LR5) in the trench and a loess deposit (LR4) from terrace Qt6 were sent to Victoria University for OSL (Optically Stimulated Luminescence) dating. The results of the OSL dating were not conclusive and are discussed in section 5.3.3.

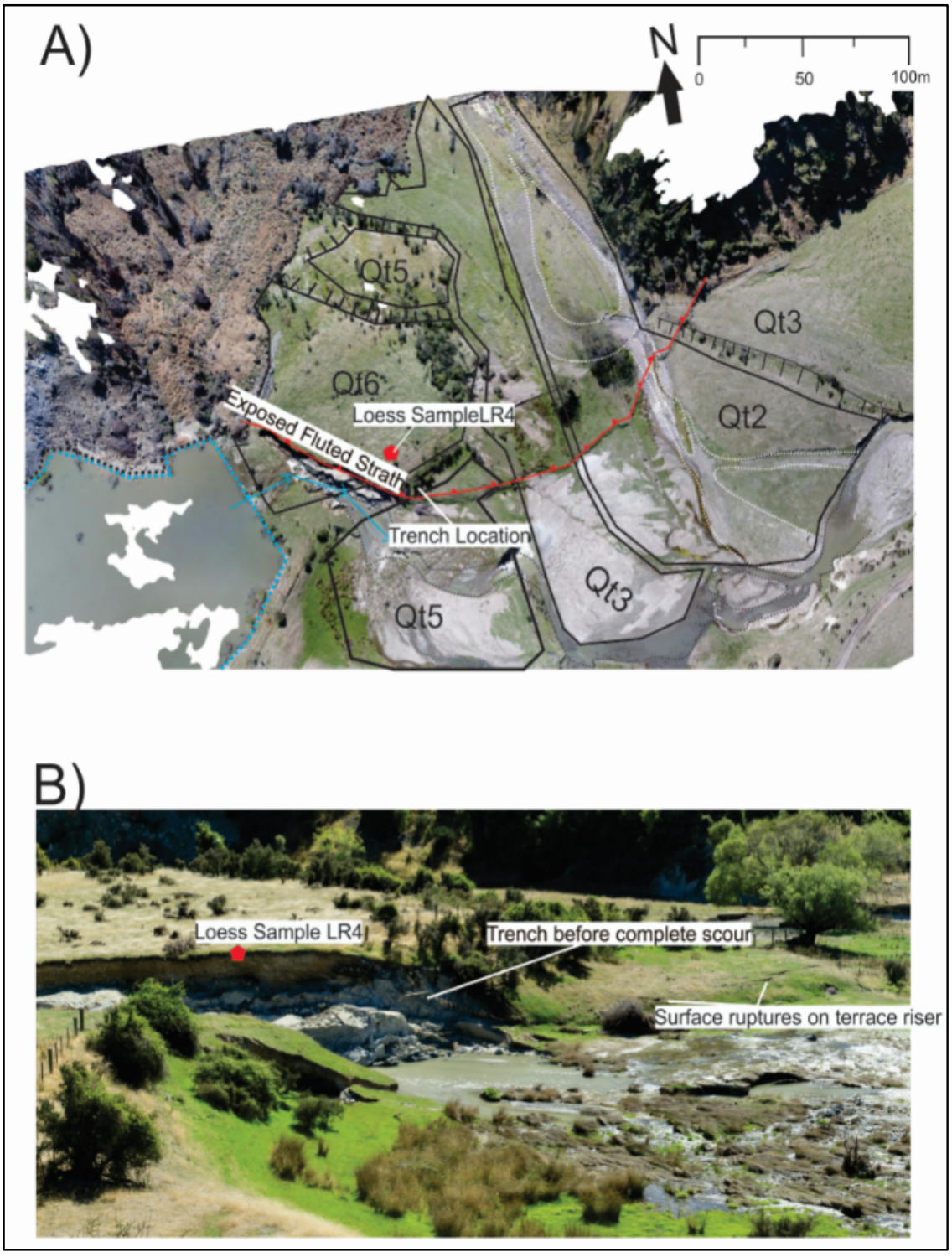

Figure 5.2: Photographs of the trench site. A) is an annotated aerial photo comprised of multiple photogrammetry images taken from a drone survey patches of white indicate sparsity of point-cloud data. The trench location is shown in the white arrow, and OSL sample LR4 is shown by a red filled circle. The fluted bedrock strath surface is exposed along the scoured terrace. B) Photograph standing on QT5 and looking north at the trench site before it was excavated.

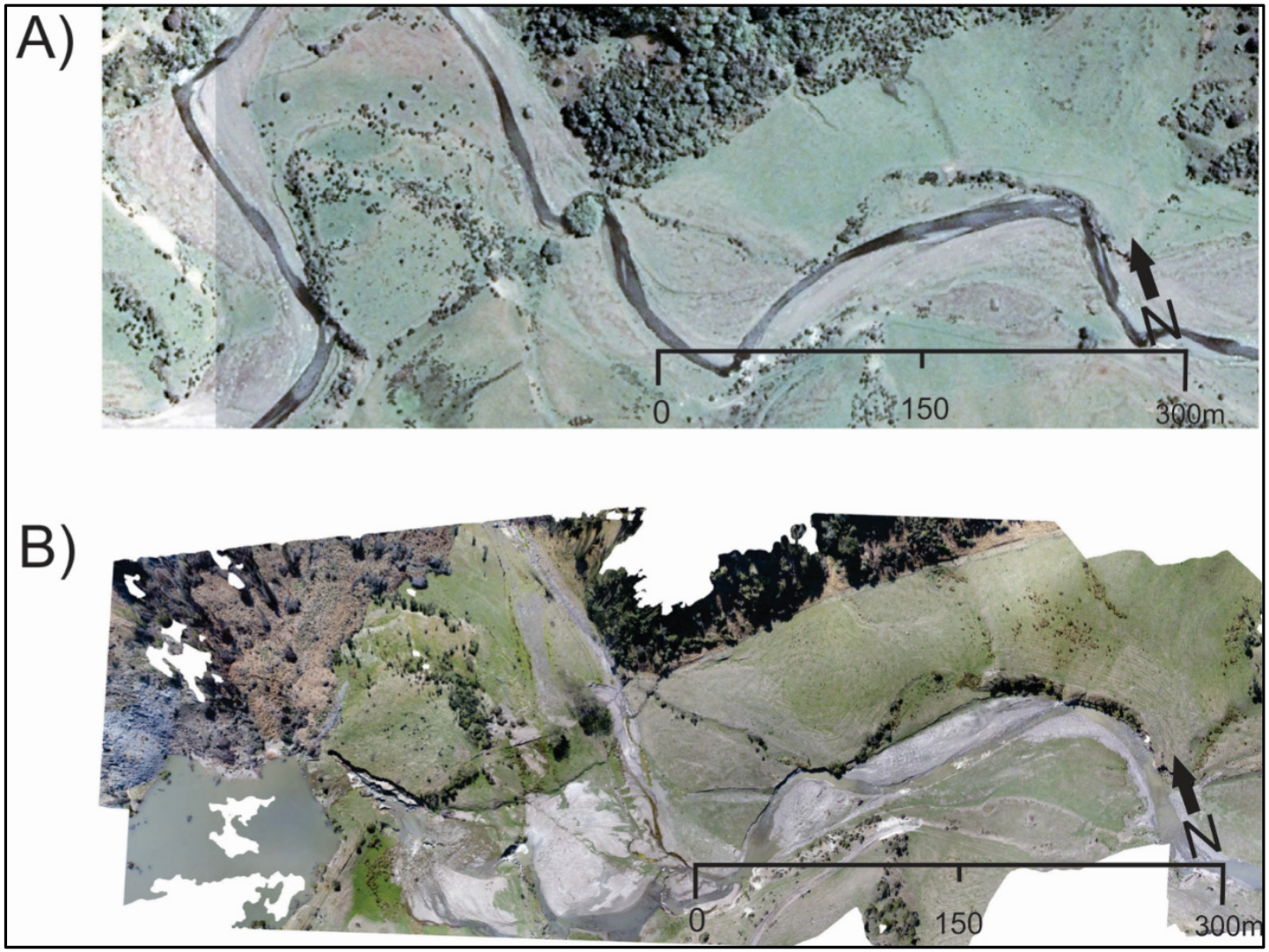

Figure 5.3: A) Kiwi Image from the 1970s showing the riverbed morphology and B) Post 2016 event and dam failure captured from a drone survey. Areas of white patches in B indicate sparsity of point-cloud data.

5.3.1 Trench stratigraphy and fault related deformation

The geometries and lithology of deposits adjacent to the fault in the trench place constraints on the earthquake activity of the fault since deposition of the sedimentary units. The geometries and boundaries of these units were mapped over 9 days during multiple visits to the site. The clarity of the primary contacts shown in figure 5.4 is variable with dashed lines corresponding to gradational boundaries, and solid lines to sharp, easily identifiable, boundaries.

The trench exposes two faults that displace stratigraphy comprising three main components; 1) Greta Siltstone bedrock (units 2, 3 & 4), 2) fluvial deposits (units 6-11) and colluvial material (units 1 & 5). Fluvial stratigraphy dominates on the right side of the log (between distances of 0 and 2.5 m), and is characterized by moderately to poorly bedded gravels similar to fluvial deposits exposed in the active river bank downstream from the fault scarp. At distances of 3 to 7 m the stratigraphy is dominated by colluvial material, while beyond 7 m the trench mainly exposes bedrock.

At the base of the trench, the coherent bedrock Greta (Siltstone) Formation (Fig 5.4, unit 4) comprises mainly fine siltstone with the occasional thin (<5 cm) sandstone and faulted lignite beds (Fig 5.5c). The bedrock strath, separating bedrock and fluvial deposits, is irregular probably due to river erosion and associated channelization. The strath surface is approximately horizontal between 0 and 2 m, however, it is tilted at ~15-37° between 2- 7.5 m, with the greatest tilt between 5 and 7.5 m towards active fault, F1 (Fig. 5.4). Units 10 overlies the strath surface and comprises a poorly sorted sandy cobble gravel. The bedding in unit 10 is approximately parallel to the strath surface and also appears to be tilted west of 5 m distance. In contrast, units 7, 8 and 9 are predominantly sub-horizontal and onlap unit 10. These units comprise beds with varying sand/silt and gravel cobbles (Table 5.1). Units 6 and 7 have higher proportions of coarse sand and silt and greater Fe-staining than units 8, 9 and 10. The observed lithologies for units 8, 9 and 10 are consistent with fluvial gravels observed down-stream and reported elsewhere in the South Island (e.g., Bull, 1991). The increase in silts and sands in the upper part of the trench may indicate an increase in the importance of overbank processes or input of fines from degradation of a near-by terrace riser.

In the upper section, two wedge-shaped units (units 1 & 5), thicken towards the faults (labelled F1 and F2 in Fig 5.4) and taper downstream to the east. There are clear differences in clast size, colour, and silt content of units 1 and 5. Unit 1 consists of light brown silt interbedded with small clasts (~2 mm), whereas unit 5 has a matrix of silt and coarse sand with many more sub-angular, chaotic cobbles. Despite their lithological differences, the two wedge-shaped bodies could represent 1 or 2 degradational events. It is possible that these events relate to fault slip and/or stream incision and terrace riser degradation. Both scenarios will be explored in the interpreted earthquake history section of this chapter.

Trench stratigraphy is displaced by two faults (F1 and F2, Fig. 5.4). Fault F1 displaces the bedrock strath surface and separates fresh bedrock in the fault footwall from weathered bedrock in the hangingwall. F1 has ~0.4 m of displacement in a reverse sense, but does not displace unit 5 or younger stratigraphy. The apparent reverse displacement on F1 is a minimum as unit 3 and an unknown amount of bedrock have been eroded from the upthrown side of the fault. F1 did not slip during the 2016 earthquake. Fault F2 is about 2.5 m higher in the section (than F1) and accumulated slip during the 2016 earthquake (on average, 0.5 m of dextral and 1 m of vertical; see Chapter 4). The dip of F2 changes upsequence. Within bedrock and unit 2 F2 dips at 40-54° N, however, when it reaches the paleo-ground surface it flattens onto the ground surface producing an overthrust, asymmetric fold (i.e., a turf roll) and fissures in the fold hinge. Overthrusting of the pre-earthquake soil in the 2016 event was ~1.2 m and is interpreted to be equal to the net dip on the fault within bedrock. Therefore, the total net slip on faults F1 and F2 is estimated to be a minimum of ~1.6 m, which is significantly less than the 4-5 m altitude change in the strath surface across the trench log. This difference may indicate that some of the altitude change across the fault in the trench reflects deformation of the Qt5-Qt6 terrace riser and it not tectonic in origin.

5.3.2 Interpreted Earthquake History

Interpretation of the processes that produced the stratigraphy in the trench and, specifically, the number of earthquakes that resulted in the configuration of units is not unique. Here, I present two interpretations of the trench data. These interpretations, named model 1 and model 2, require different numbers of ground-rupturing earthquakes. These differences largely reflect uncertainty in the origin of the colluvial wedges (units 1 and 5) which reflect degradation of a fault scarp or a terrace riser and could reflect one or two deposition events. More investigation and excavation on the opposite side of the river (to the trench) is required

to constrain the geometry and genesis units 1 and 5. In the absence of more data, the available stratigraphy could be explained by 2-4 surface-rupturing earthquakes (including the 2016 rupture) and define the present uncertainties in the paleoseismic data.

Table 5.1: Unit descriptions for lithologies presented in figure 5.4 and 5.5

Unit 1	40% silt; 30% medium-coarse sand (~.60mm); 20% gravels (~7mm). 10% elongated, sub rounded cobbles (~60cm) in the lower unit. 10-80cm thickness.
Unit 2	Weathered bedrock, no clasts. 90cm-2m thickness
Unit 3	Fractured bedrock with jointing, with small clasts (~5mm) increasing in frequency towards unit 5. To the left bedrock is matrix supported, to the right it is clast supported. 80cm thickness
Unit 4	Bedrock, Greta siltstone; 90% blue-grey moderately indurated siltstone; 10% fine sand (>.25mm). Matrix supported with mud/calcite cementation. Sharp, erosional boundary. Low-energy continental shelf or slope depositional environment. ~480m thickness (Brown and Field, 1985)
Unit 5	0.5% Boulders (~252mm); 30% cobbles (~40cm); 20% gravels (~7mm); 59.5: course sand (~.60mm). Olive green-grey. Sub-angular, largely aligned clasts. Matrix supported. 10-80cm thickness. Likely colluvial wedge
Unit 6	30% subangular gravel (~6mm); 40% lenses of well sorted, fine sand; 30% silt. Loosely consolidated, clast supported. 10-15m thickness.
Unit 7	5% boulders (~256cm); 20% cobbles (50cm); 30% gravels (~10mm); 20% silty mudstones; 25% course sand (~.60mm). Poorly sorted, cemented, and consolidated. Fe staining common. Likely fluvial deposition
Unit 8	100% well sorted, loosely consolidated, medium-fine light grey sand (>.25mm). Approx 40cm max thickness, some horizontal bedding, and abrupt sharp boundaries between units. Likely low-energy fluvial depositional environment
Unit 9	Varying contents of boulders, pebbles, gravels, silt, and sand. Lenses of dark grey course to fine sand, horizontal bedding apparent. Largely loosely consolodated. Likely floodplain fluvial depositional environment.
Unit 10	1% boulders (~256mm); 20% cobbles (~60cm), 20% gravels; (~7mm); 60% fine sand. Sub-angular clasts, poorly sorted and cemented, matrix supported, and tilted with respect to bedrock. 40-80 cm thickness Likely storm surge/ high energy fluvial or possible third colluvium
Unit 11	40% Clay; 60% course sand. Well sorted and matrix supported lenses that pinch out on coherent bedrock

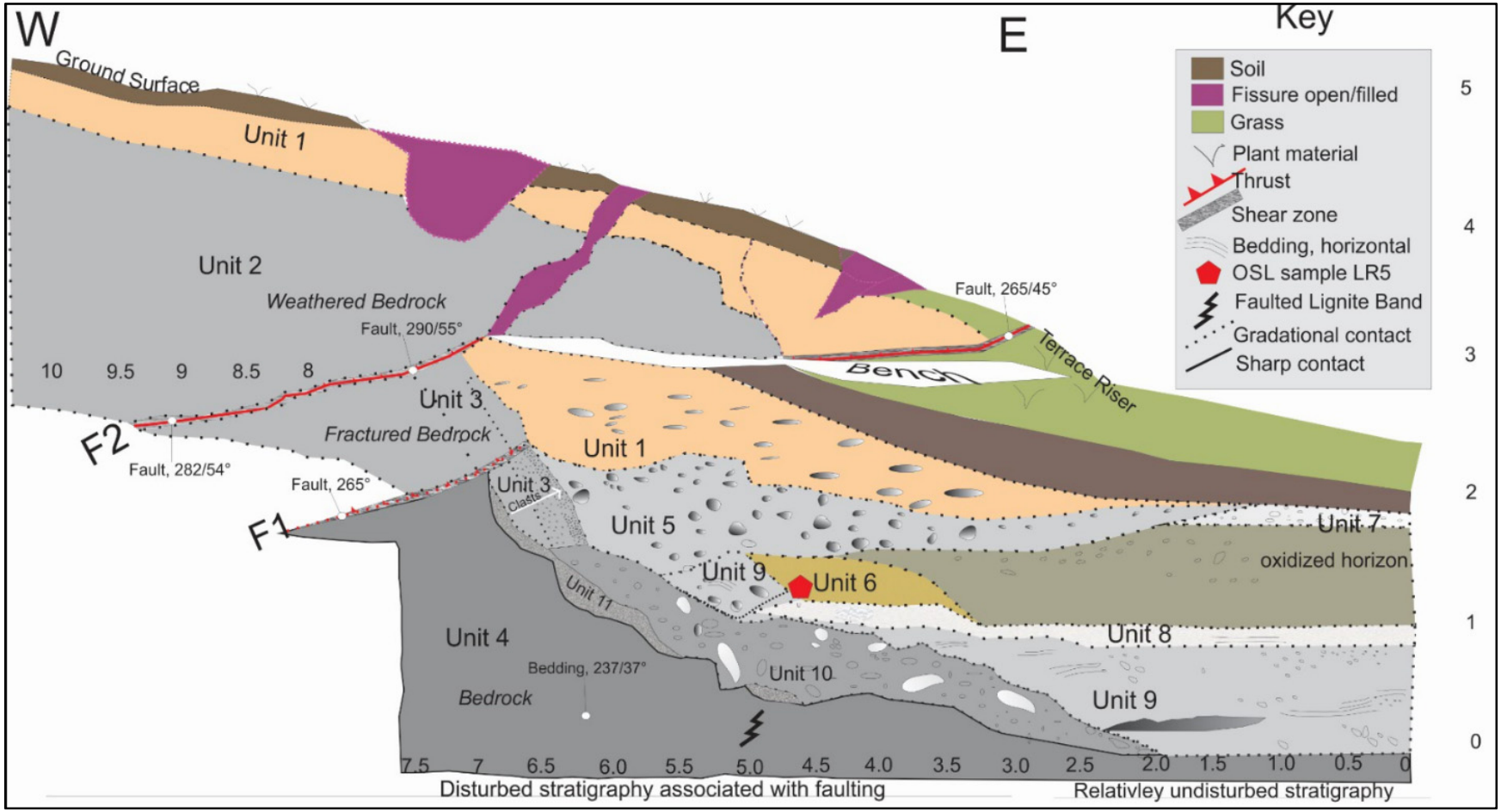

Figure 5.4: Interpreted trench log from the Leader River Trench site. Refer to Table 5.1 for unit descriptions. Trench log is at true scale with distances along the base of the log in metres.

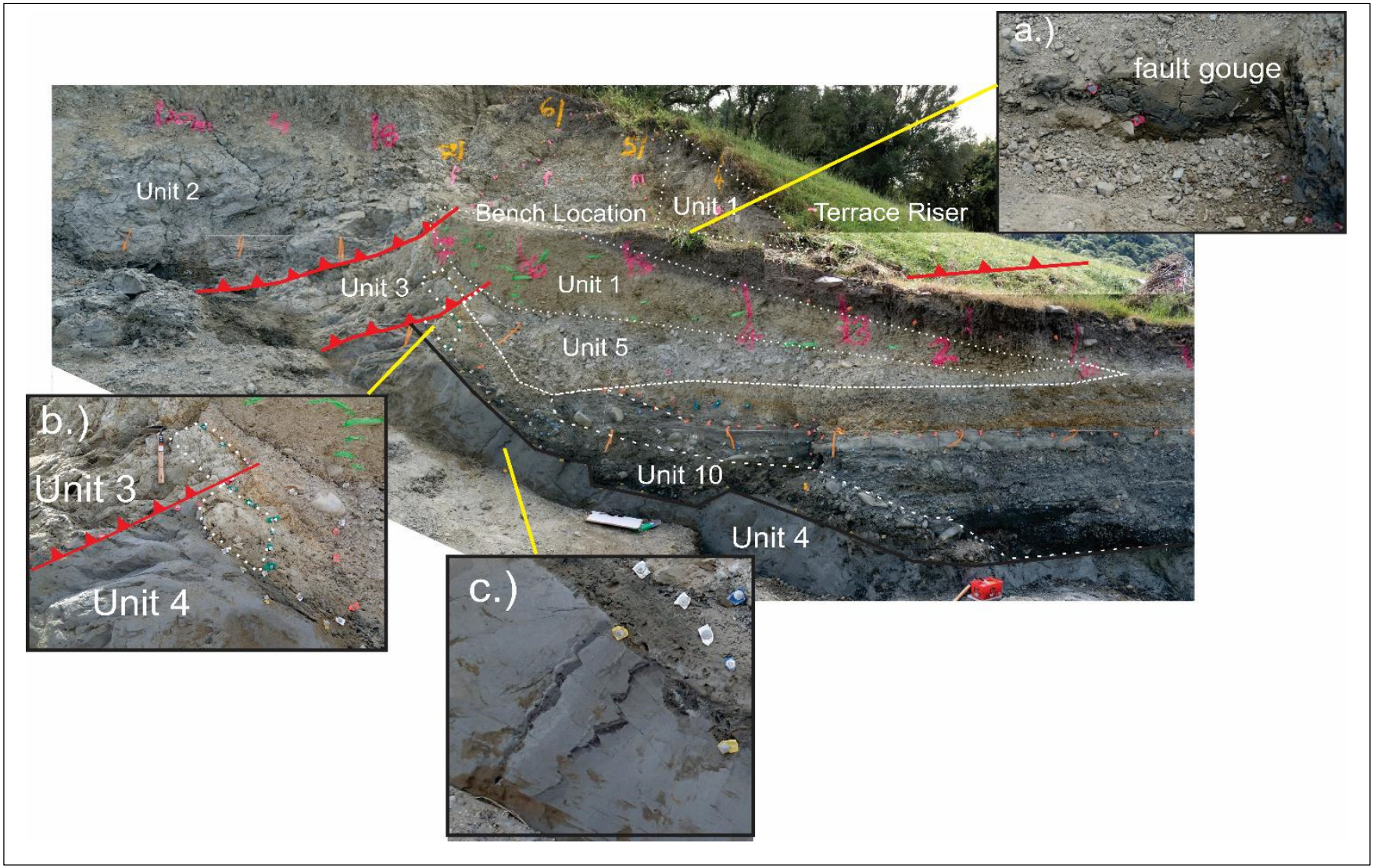

Figure 5.5: Annotated photograph of trench log to accompany Figure 5.4. Key parts of the trench are shown. a) Section of fault gouge excavated in the bench and exposed at the the fault bend, b) annotated offset block of weathered bedrock across F1, and c) bands of faulted lignite in bedrock.

Model 1: Two Earthquakes and Wedges of Sedimentary origin: In the first model the wedge-shaped colluvial units (units 1 and 5) are assumed to have formed in response to degradation of a terrace riser produced by down-cutting of the Leader River. In support of this model the terrace riser which separates the Qt5 and Qt6 terraces immediately north and south of the trench can be mapped into The Wall of the trench at the approximate location of the wedges. If these wedges reflect sedimentary rather than tectonic processes, the primary evidence for earthquakes in the trench log is provided by faults F1 and F2. Fault F1 displaces bedrock, the bedrock strath surface and units 10 and 11, but does not appear to displace units 1 or 5, suggesting that the event post-dates units 10 and 11 and predates units 1 or 5. For the two-event model the second event occurred in 2016 and displaced both the trench stratigraphy and the ground surface. Both events post-date the formation of the terrace surfaces Qt5 and Qt6 and could have each accommodated throws of ~0.5-1 m consistent with the amount overthrusting in 2016 and the displacement on F1 (Fig 5.6).

Model 2: Two-Four Earthquakes and Wedges Tectonic: In this model the wedge-shaped colluvial units (units 1 and 5) are assumed to have formed in response to one or two surface-rupturing earthquakes. In support of this model the wedge-shaped bodies formed in close proximity to fault F1. If these wedges reflect tectonic processes, each wedge defined by units 1 and 5 could have formed in a discrete earthquake or both units could reflect a single event. In either case it would inferred that the event that produced the ~0.4 m displacement and tilting of the bedrock strath on (or associated with) fault F1 was also responsible for the scarp that was subsequently degraded to produce unit 1 or unit 5 or both units. If this is the case, then units 1 and 5 together with displacement in F1 would require one or two surface rupturing earthquakes. As with model 1 the 2016 earthquake represents an additional event and all events probably post-date the formation of the terrace surfaces Qt6. Two to three events of 1-1.5 m would be required to account for the apparent 4-5 m displacement of the bedrock strath in the trench. Figure 5.7 depicts a sequence of events that could have been associated with Model 2.

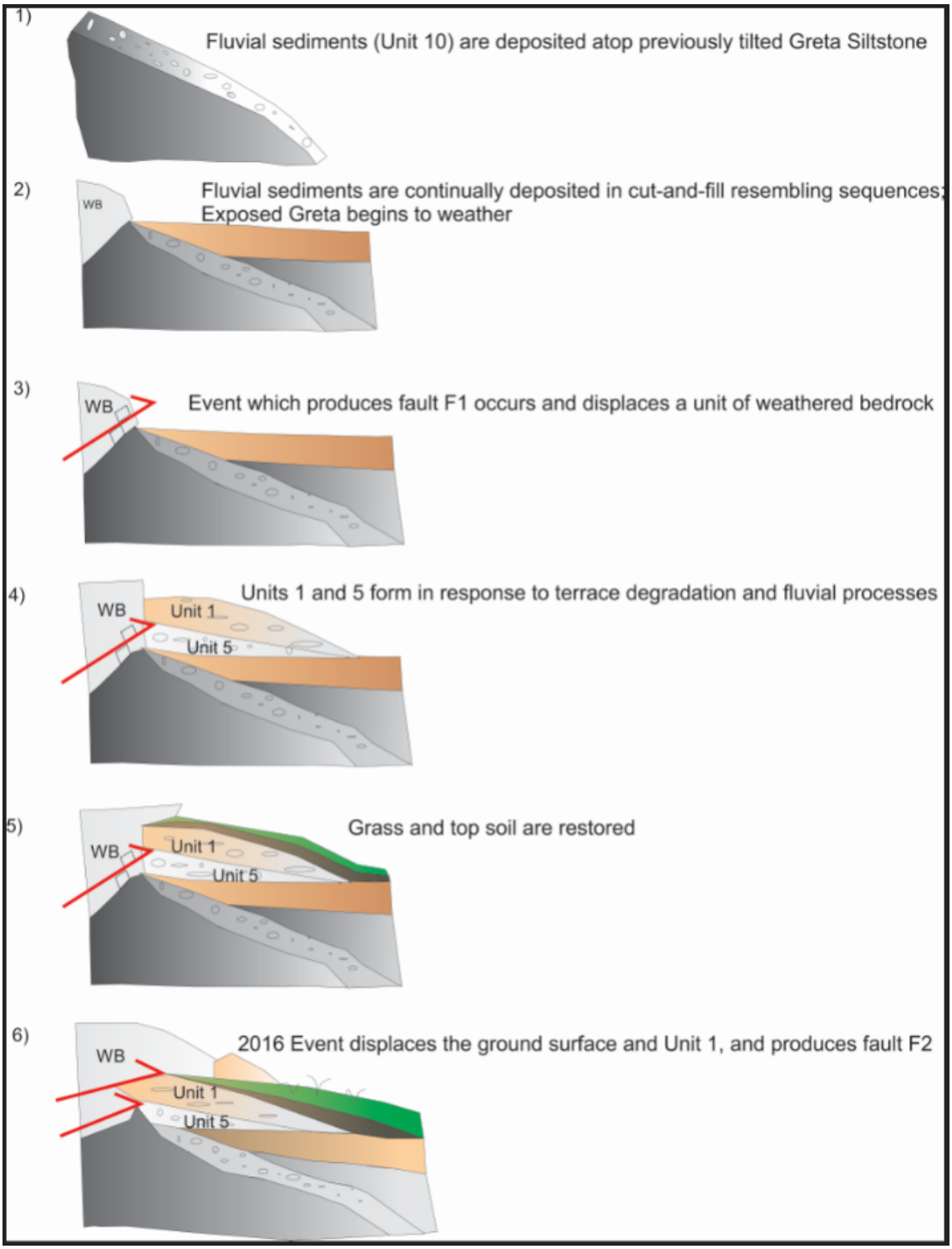

Figure 5.6: Schematic diagram of possible earthquake history for Model 1: Two Earthquakes and Wedges of Sedimentary Origin.

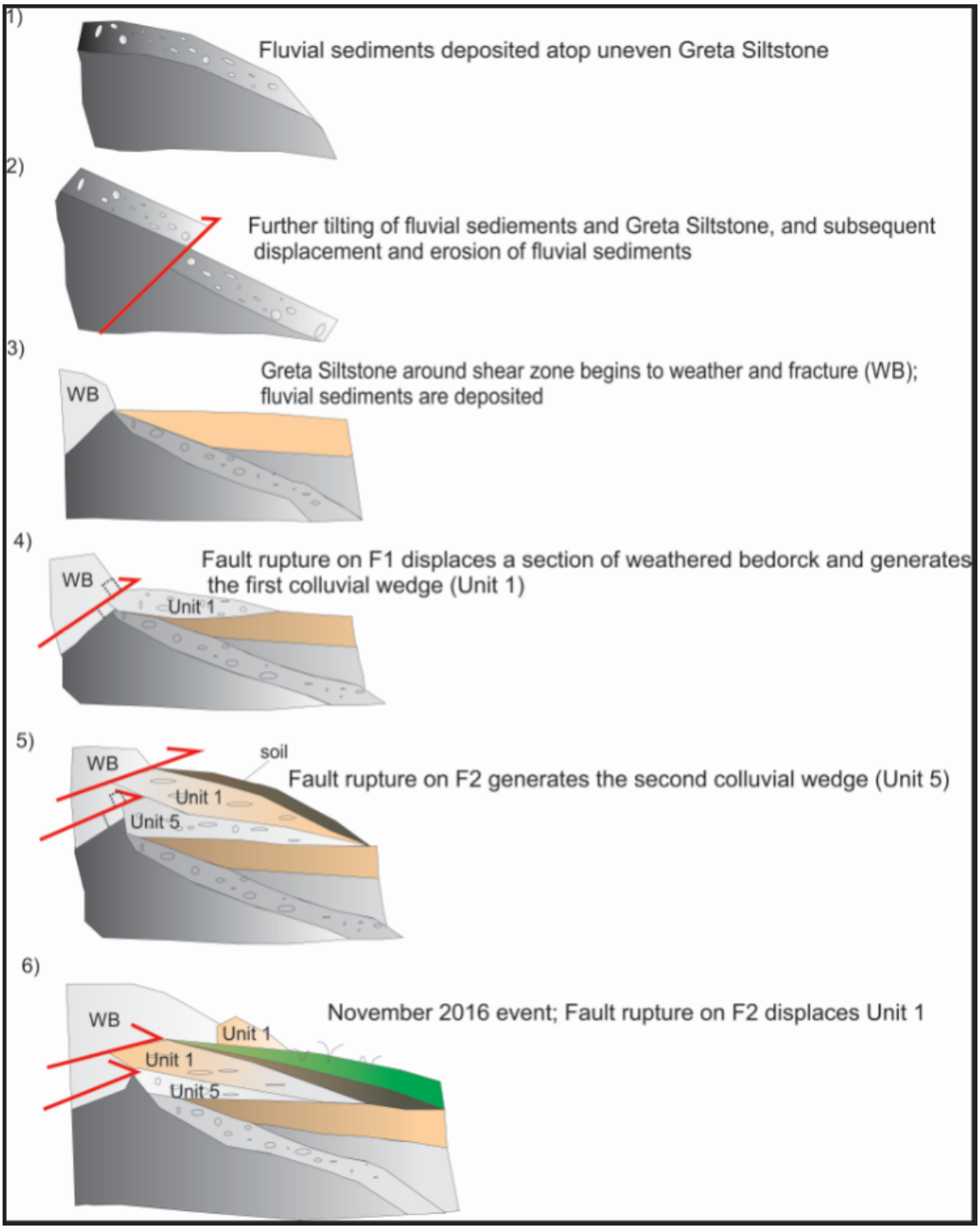

Figure 5.7: Schematic diagram showing possible earthquake history for Model 2: Two- Four Events and Tectonically Generated Wedges.

5.3.3 Ages Qt5 and Qt6 terraces and paleoearthquakes

In an attempt to constrain the timing of the earthquakes inferred from the trench, two samples were sent to the Victoria University OSL dating laboratory (Chapter 2 of this thesis reviews the procedure used for dating them, and the full report is available in appendix E). One

sample was collected from unit 6, a silty sand on the downthrown side of the fault, and a second from a loess sample resting on the Qt6 surface (see Fig 5.2A and 5.4 for locations and Table 5.2 for sample details). The ages for these samples were reported as 46.4 ± 2.9 ka (LR4; loess atop terrace 6, Fig 5.2) and 43.6 ± 2.6 ka (LR5; paleosoil, Fig 5.4). Although internally consistent, these ages are significantly older (~30-40 kyr) than would be expected from interpretations of the geomorphology in the river valley or from previous interpretations of the terrace ages (e.g., Rattenbury *et al.*, 2006). This incompatibility could arise because our models for landscape evolution in the region of study are incorrect, or because the sample dated primarily contained feldspar that was recycled within the catchment without sufficient exposure to sunlight, and thus has not had its signal reset. This will be further addressed in the discussions section of this chapter.

In the absence of direct dates to constrain the ages of the terrace surfaces in the study area, the age of the Qt10 surface is here inferred to be ~18,000 ka in age (Rattenbury *et al.,* 2006). If this age is correct and the rates of river down-cutting were approximately uniform since ~18,000 ka the Qt6 terrace surface may be approximately mid Holocene in age. Based on the available data (and their interpretation) it is suggested that two-four earthquakes (including the 2016 event) occurred in this time.

Table 5.2: Summary of OSL samples LR4 (loess atop terrace QT6) and LR5 (sandy silt). The full report is available in the appendices.

Lab Code	Field Code	Depth below surface(m)	Water(%)	Dose Rate (Gy/Ka)	Age (ka)
WLL1289	LR4	0.46	15	3.09 +/- 0.19	46.4+/-2.9
1LL1290	LR5	1.45	15.5	3.61+/- 0.21	43.6+/-2.6

5.3.4. Single event Displacements

Chapter 4 described the average vertical and dextral displacements on the fluted terrace surface of ~1 m and ~0.5 m, respectively, during the Kaikōura event. Single event displacements for the prehistoric event(s) is poorly constrained by data from the trench or displacement of the bedrock strath. The reason for this uncertainty is the lack of clarity in the total displacement of the bedrock strath and the number of prehistoric earthquakes; in both cases these uncertainties are due to the presence of the Qt5 and Qt6 terrace riser at the trench

site. Additionally, the strath terrace is uneven upstream away from the fault, and displays large scouring events which complicate what is truly tectonic displacement. Given these uncertainties, it is only possible to say that the event which produced the F1 fault had a net slip of at least ~0.4 m. Therefore the events prior to 2016 the single event displacements are poorly constrained.

Figure 5.8 shows the difference in elevation from the top of the strath terrace on the south side (un-faulted) of the river and the top of the fluted terraces displacements described in chapter four for two locations. The above in figure 5.8 has the viewer positioned standing downstream from the scour looking towards the landslide dam. In the image below, the viewer is standing on the waterfall where the lake breached, looking to the east. The vertical displacement across the river was measured at 3 locations (marked 1-1', 2-2', and 3-3'). The maximum displacement is 3.4 m at the bottom of the terrace riser (location 1-1'), and the minimum is 1.4 m at the top of the terrace riser (location 3-3'). Location 2-2' has a displacement of 3.1 m, and the average displacements across the strath terraces here are 2.6 m.

If the average vertical displacement for the Kaikōura event on the fluted terraces is ~1 m, and the average total vertical displacement from across the fault is ~2.6m, this could imply 2-3 events on this fault in the Holocene. But given that the strath terrace is uneven to begin with, limited trench interpretations, and unclear ages of Quaternary surfaces, these numbers are currently little more than conjectures.

Figure 5.8: Above: Depicts the difference in strath elevation across QT6. Viewer is standing looking upstream towards the head of the scour. Below the viewer is positioned looking downstream at the head of the scour.

5.5 Pre-existing fault scarps

Despite the Holocene history of surface faulting on the HF in the trench, no active fault traces have been previously mapped in the study area. Armed with knowledge of active fault locations provided by the 2016 ruptures re-examination of the pre-earthquake aerial photographs was undertaken to determine if there is evidence of prehistoric events. Colour aerial satellite photographs from 2015 (Zekkos *et al.* 2018) together with black and white photographs of ~1:17,000 from NZ Aerial Mapping (NZAM 1950, run 1800/ 40-49 and run 1799/ 40-50) were used to search for pre-existing active fault scarps in the study area. These photographs were examined as stereo pairs and individually. It is estimated that in open farmland with limited relief (<10 m per 500 m) scarp heights as little as 0.5 m could have been identified from the images if such scarps were present.

Examination of the images revealed few pre-existing scarps. No unequivocal evidence for pre-existing scarps were observed along the SLF. The aerial photographs show no evidence for the fault at the trench site, or anywhere in the Leader River bed prior to the earthquake. The only evidence for pre-existing deformation was observed on the Qt10 surface upstream of the trench site where rolls or warps up to ~80 m in length were observed to trend NNW across the terrace surface (figure 5.10). These warps are located between strands of the HF and could have formed during the event(s) identified in the trench. The aerial photo analysis supports the suggestion that previous examination of aerial photos in the study did not miss clear and obvious active fault scarps.

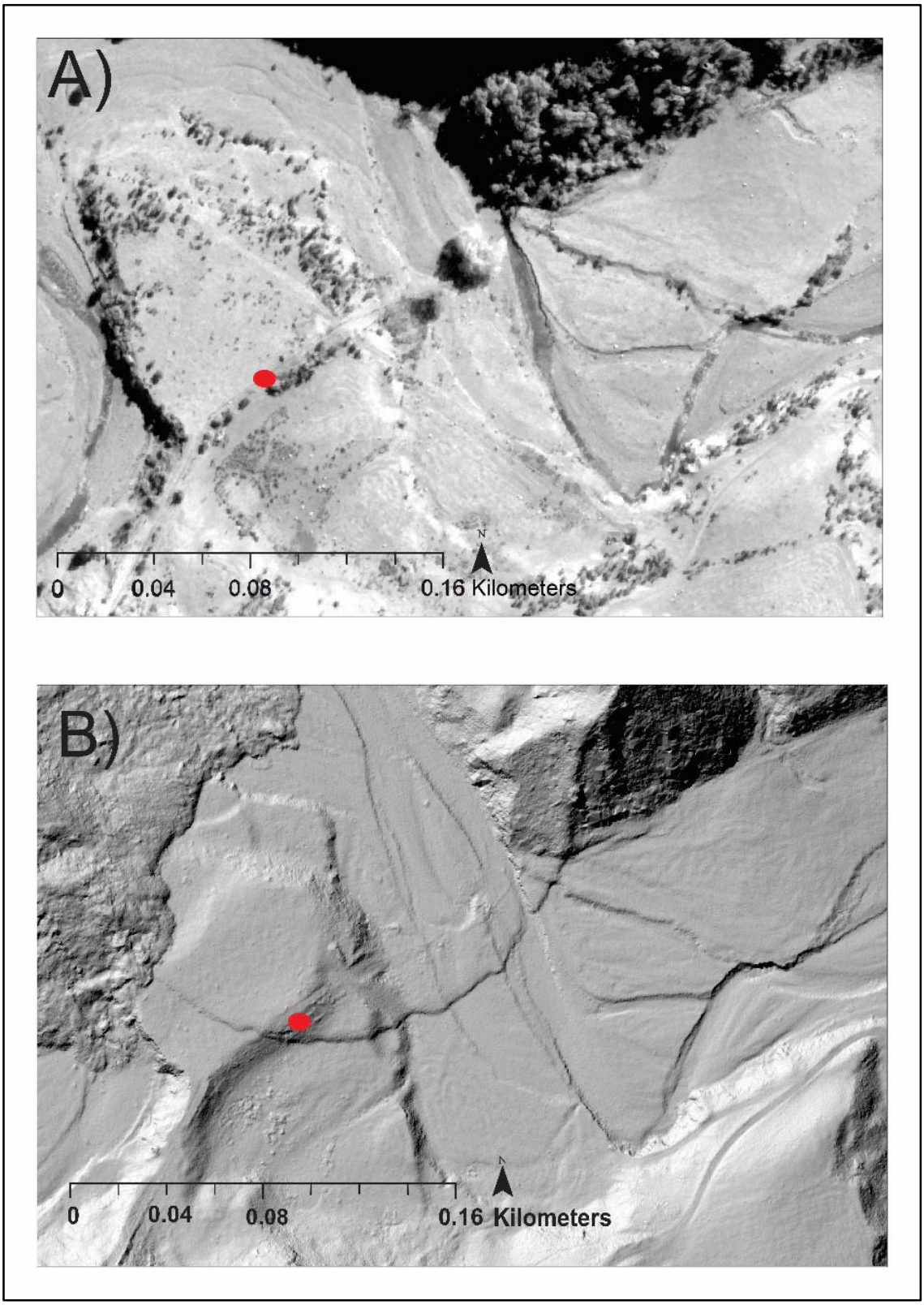

Figure 5.9: Pre and post comparisons of the trench site, where A) Shows an orthophoto from May 2015, and B) Shows a hillshaded LiDAR model (0.25 m resolution) of the landscape post the 2016 event. A red ellipse approximately marks the trench.

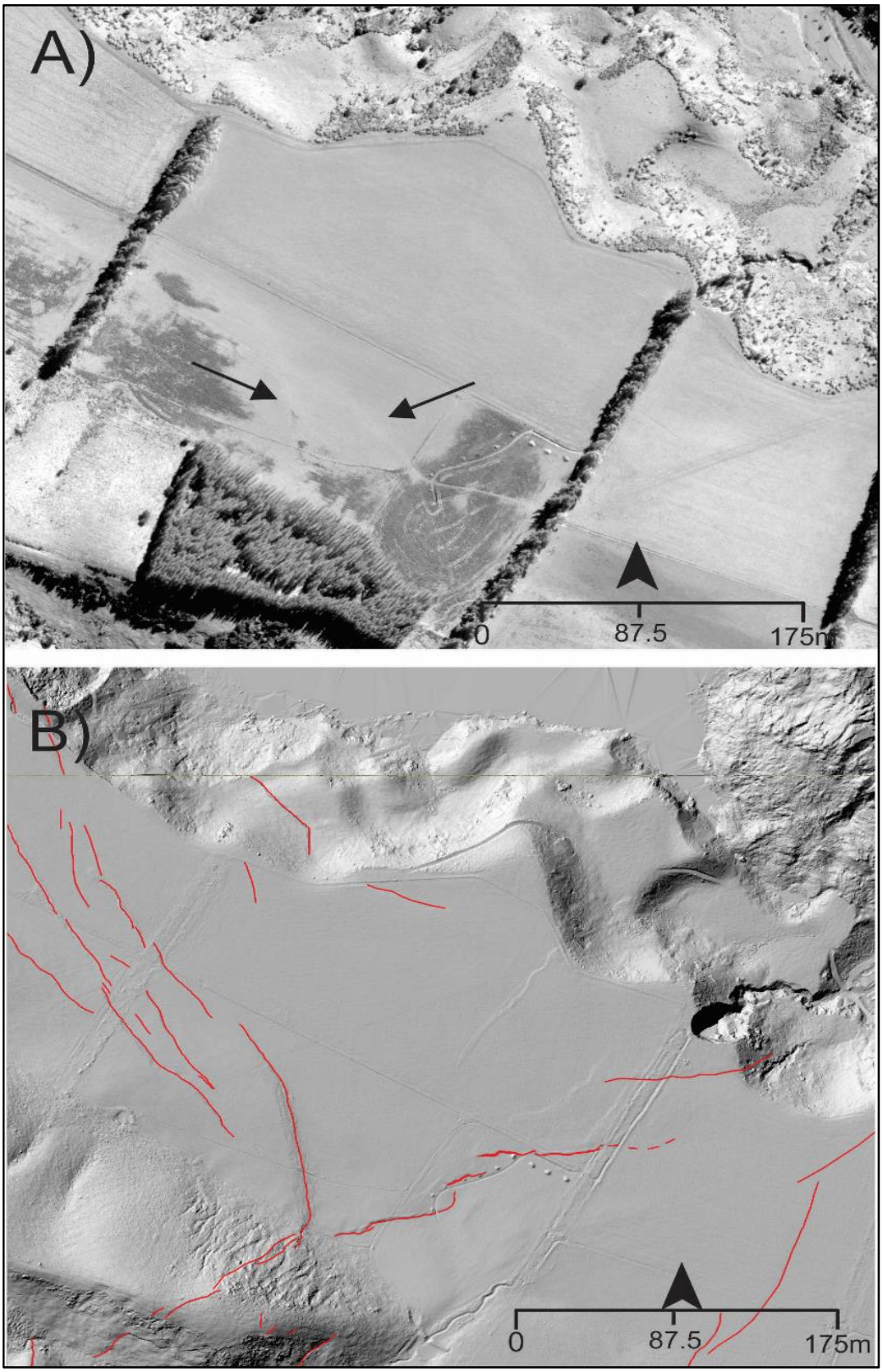

Figure 5.10: Pre (A) and post (B) imagery of the faults on the Qt10 terrace surface above and west of the trench site. Close examination of A) reveals discrete rolls (indicated by black arrows) on the high terrace that later ruptured in 2016.

5.6 Discussion

The SLF was unnamed and considered inactive prior to the 2016 earthquake. At present its paleoseismic is also unknown, and will require data from multiple trench locations to constrain the timing and size of the prehistoric events.

Some limited evidence for previous earthquakes on the HF in the Leader River Trench are presented in this chapter. Currently the available data suggests the possibility of two or three events on the HF (including the 2016 event) since the mid Holocene. The precise amount of events in the Leader trench is unclear because this trenching site is in not optimal for separating faulting and sedimentalogical processes.

Currently, there are trench investigations underway on the western segment of the HF where it crosses the Emu Plains. Although these studies are not complete, they do provide some inFormation on the paleoearthquake history of the fault. At the McClean's Trench on the Emu Plains (Fig 5.11) the 2016 rupture produced vertical displacements of ~0.5 m and dextral displacements of ~2.0 m (Brough, pers comm., 2018). Four to five paleoearthquakes were identified in the trench stratigraphy at the McClean's Trench, which is presently assumed to span ~20 kyr. If the assumed age is correct then these events would have occurred every 5-7 kyr. Aditionally, an OSL date of 9.7±0.8 ka from silt resting on a fluvial terrace provides an age estimate for the surface trenched. This surface had a fault scarp prior to the 2016 earthquake, which suggests that it was displaced by two or more surface-rupturing earthquakes (including 2016) with a recurrence interval of no more than 10 kyr. Taken together the data from the Emu Plains and from Woodchester (this study) suggest both the eastern and western segments of the HF likely ruptured during the Holocene and that the recurrence intervals of these events were probably thousands of years but perhaps not greater than 10 kyr.

The dates for the loess and paleosoil sample were much higher than the expected age. There are numerous publications which highlight the limitations of OSL dating in mountainous, glacial, or tectonically-active areas (Guralnik *et al.,* 2015; Preusser *et al.*, 2006; Rhodes and Pownall, 1994; Smith *et al.,* 1990). Woodchester Station exhibits all three of these environments. While OSL dating can yield successful Quaternary dates, one of the key challenges is in selecting sediments that have had their luminescence signal fully reset prior to their deposition (King *et al.,* 2014). This can only occur when the sediments (quartz and

feldspar) have sufficient exposure to sunlight. Partial resetting (known as bleaching) occurs when there has not been sufficient infrared stimulated luminescence (IRSL), and in these sediments, older signatures can meddle the depositional ages (King *et al.*, 2014). Fluvial and glacial deposits are especially prone to the effects of bleaching (Rhodes and Pownall, 1994), as well as sediments in mountainous areas (Srivastava *et al.,* 2008). The Leader River Trench is situated in a riverbed immediately before the inland Kaikōura ranges, and it is likely that the sediments did not have sufficient exposure before erosion and deposition, and are likely carrying IRSL signals prior to their deposition. Additionally, the IRSL signal of feldspar saturates at higher doses than quartz (Kars *et al.,* 2014), and if there is not sufficient sunlight, they will not reset.

While these obstacles in OSL dating explain the discrepancy for the paleosoil sample, aeolian deposits do not usually experience bleaching as frequently or readily as fluvial, glacial, or range-front sediments. However, only one sample was taken from each location. For there to be a truly well-constrained date, at least three samples would be needed. Although the ages given from Rattenbury *et al.,* (2006) are inferred, a terrace age of 50,000 years old is highly unlikely at this location, given the geomorphological context.

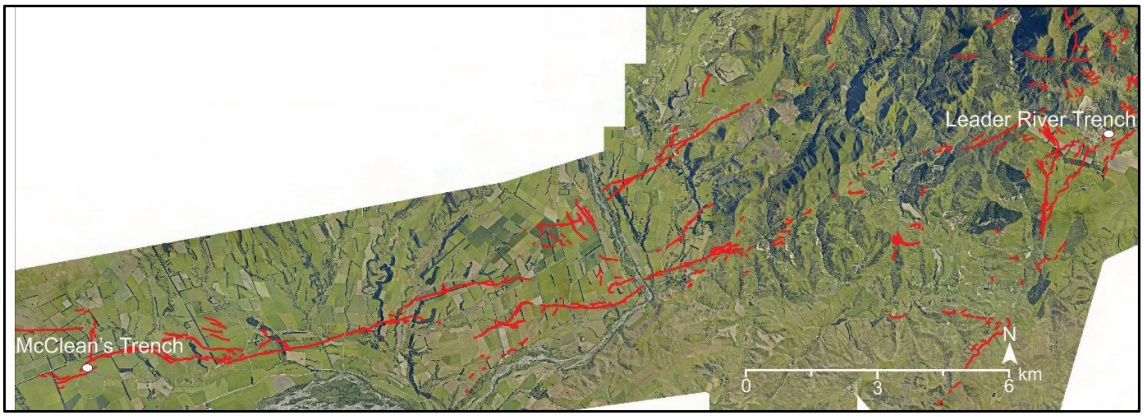

Figure 5.11: Map showing the HF west segment, where the McClean's Trench is marked. This sits approximately 24km SW of the Leader River Trench.

5.7 Summary

- The landslide dam breached in March of 2017, and the river scoured the fault plane through the terrace Qt6, exposing both the fault and the bedrock. This erosion produced a natural trench that was analysed here,
- The natural trench was close to the Leader River bed near the junction of the SLF and HF faults. The fault scarp cross multiple river terraces, the age of which are not well constrained,

- The trench may indicate at least 2-3 events from the mid Holocene (including 2016). The variation in the number of events because colluvial wedges in the trench have formed due to faulting or river erosion,
- An interpretation for 2-3 events in the Holocene could, at the moment, be consistent with initial interpretations from trenches in the western section of the HF, where recurrence intervals of 5-7 ka are possible,
- There is no undisputable evidence of pre-existing fault scarps along the SLF visible in pre-earthquake aerial photographs. The only clear pre-existing structures are shown in Fig. 5.10 on the Qt10 surface. These pre-existing scales are interpreted to be part of The Humps Fault and their presence is consistent with the findings from the Leader River Trench.

6.0 CONCLUSIONS AND FUTURE WORK

6.1 Introduction

This thesis has essentially been a year of post-earthquake reconnaissance following the November 2016 Kaikōura Earthquake. Insights to the geological controls, kinematics, and paleoseismic activity of faults that ruptured the ground surface at Woodchester Station were achieved through combined methods that have involved fault trace, displacement, geomorphological and geological field mapping, terrestrial LiDAR, InSAR analyses and historical aerial photo analyses, and a single natural paleoseismic trench. The results provide information about the South Leader (SLF) and the Humps (HF) faults in the study area and are summarized in this chapter.

6.2 Geological controls on fault geometry

Field mapping and LiDAR analyses along the SLF its intersection with the HF revealed many short, discontinuous, fractured ruptures that were complicated by topography and formed a zone of faulting up to 3 km wide. These faults varied greatly in their orientation, and could neither be described by a "single rupture trace" nor by one type of fault kinematics (Figs 3.4, 3.5, 3.6, 3.7& 3.8). The faults were divided into three different groups following combined geological mapping and fault trace mapping.

1. NE-SW Striking (210-245°), shallow to moderate dipping (25-40°) oblique thrusts with bedding-parallel or sub-parallel orientations along the SLF,
2. N-S (350-360°) striking steeply dipping (70-85°) faults with sinistral normal displacements of the SLF and,
3. ENE-WSW (250-290°) striking moderately dipping (50-68°) reverse dextral faults of the HF.

Bedding-parallel and sub-parallel structures ruptured bed boundaries within, and at the base of Cenozoic strata, and include: The Leader Road Fault (068/45°NW) which ruptured the contact of the Greta Siltstone and Torlesse Supergroup basement (~64/42°W), the Quarry Fault (200-240°/33°W) which ruptured the contact between the Waimea Formation and Amuri Limestone (~240°/28°), the Shearer's Quarters Fault (225/40°W) which ruptured the contact of the Greta Siltstone Formation and Waimea Formation (240-255°/37-45°), and the Pumphouse Fault (210°/40°W) which ruptured the contact between the Eyre Group and Greta Siltstone Formation (250°/30WNW). Similarities between the orientations of the faults and the beds (Figs 3.7 & 3.8) together with the near orthogonal angle between the fault slip

vectors and the ~40° trends of fold hinges (Fig 3.1) supports the idea that these faults accommodate flexural-slip during folding of the Cenozoic cover sequence (Fig. 3.10). If correct, this hypothesis suggests that surface deformation during the earthquake was accommodated by a combination of discrete fault slip and distributed folding. Based on these data it is possible that similar folding, which occurs throughout North Canterbury, was also achieved by flexural slip.

The N-S striking and steeply-dipping sinistral normal faults at The Waiau Wall represent the most spectacular surface ruptures during the 2016 earthquake south of Kaikōura (Fig 3.6 & 4.6). This rupture produced slip on a fault that displaces Cenozoic strata at a maximum of 800 m, and has likely accommodated many Late Cenozoic earthquakes, although the timing of these displacements cannot be determined from local stratigraphic relationships. Despite the indications of previous earthquakes from bedrock stratigraphy, there is little topographic relief on the upthrown western side of the fault, and there is little correlation between uplift during the earthquake and topography (Fig 3.9). This lack of correlation suggests that fault displacement rates are lower than the rates of erosion.

Strands of the Humps Fault (HF) have been mapped in northern parts of the study area. These faults strike ENE (sub-parallel faults of the HF extend farther east), dip moderate to steeply NW (~45-68°) and carry oblique dextral reverse displacements. The most important fault of the HF in the study cuts across the headwall of the Leader Landslide where it juxtaposes Torlesse basement over Greta Siltstone across a fault plane oriented at ~250/39°N (Fig 3.2E). Locally at the trench site (Chapter 5) the fault is strand of the HF swings in strike ~45° to become bedding-parallel. This fault suggests that bedding-plane and HF faults are hardlinked and kinematically working together.

6.3 Fault kinematics and regional strain

The kinematics of the faults in the study area were analysed using displacements of the ground surface and striations on fault planes. These results together with the geometric information from Chapter 3 were used to develop a schematic model of faulting (Fig 4.10). Surface displacements measured from the 2016 rupture scarps are highly variable on the SLF (Fig 4.2), with maximum displacement on The Waiau Wall. These variations in displacement reflect a number of factors including the strike and dip of faulting and the extent to which is distributed or confined to a single slip surface (Chapter 4).

Slip on bedding-parallel/sub-parallel faults occurs on weak bedding planes in Cretaceous-Cenozoic strata, and are interpreted to accommodate flexural-slip folding. These faults exhibit low-angle dips, and can be broadly characterized as thrusts/oblique thrusts. Bedding-parallel or sub-parallel faults along the SLF individually exhibited less displacement, and displayed a higher ratio of vertical to horizontal displacement than the steeply-dipping structures (e.g., The Waiau Wall fault; Table 4.1). These thrusts have a varying amounts of sinistral slip (excluding the reverse dextral South Leader Road Fault) and V:H ratios of 10:3 (the South Leader Road Fault) to nearly 1:1 (Pumphouse Fault). Nevertheless, the average S_1 for these faults is approximately ~91°, which compares favourably with the regional Principal Horizontal Shortening (PHS) (~120° ± 19°; Nicol *et al.,* 2018), and the maximum horizontal compressive stress of 115° ±15° from earthquakes (Sibson *et al.,* 2011;2012). The PHS and slip vectors on these bedding-parallel faults is nearly perpendicular to fold hinges (Fig 3.10 & 4.10).

Slip on the N-S steeply-dipping is oblique sinistral and down to the east. Movement occurred on a fault with as much as 800 m of total vertical displacement and may reactivate or use a steep N-S basement fabric (Fig 3.8). These steeply-dipping structures (The Waiau Wall) displayed the highest amount of vertical and sinistral displacement (3.5 and 3m, respectively; Fig 4.2). Despite a predominance of sinistral motion, the stereonets portray a predominantly dip-slip sense (Fig 4.7A), resulting from an exaggerated vertical displacement. The Wall highlights the problems with the kinematic model, and is the most inconsistent with respect to the regional trends.

Faults in the north of the study area that strike ENE and carry oblique dextral reverse slip are part of the HF. The Leader River Trench fault is part of the HF and has a V:H ratio of 2:1 and displayed reverse dextral motion. This fault swings in strike by ~45° to become bedding-parallel, demonstrating that the HF and bedding-parallel faults are in places linked and working together kinematically (i.e. slip was transferred from the HF to bedding planes in the Cenozoic sequence).

Vertical displacements at The Waiau Wall and part of the Quarry Fault are elevated due to local gravitationally-induced slip on these faults. Inferred gravitational slip is supported by striations on The Wall fault plane (Fig 4.6; 4.7), which record an initial phase of strike-slip followed by mostly dip-slip. The change in orientation of striae is inferred to reflect initial

tectonic slip produced by the earthquake followed by slip dominated by a gravitational overprint, which might account for up to 2 m of the total vertical displacement. Gravitational processes also appear to have utilized the Quarry fault, which is sub-parallel to bedding and in the quarry has a normal oblique displacement associated with locally fissure formation. Here the bedding plane appears to be accommodating slope failure into an adjacent deeply incised valley (Fig 4.11).

The orientations of the principal strain axes for surface rupturing faults in the study area are broadly consistent with the regional principal horizontal shortening of ~100-140°. For example, the S_1 value reported for Leader River Trench fault is 117°, and consistent with both the PHS and maximum compressive stress for dextral strike-slip faults (Nicol and Wise, 1992; Sibson *et al.,* 2011). Therefore, the kinematics of the earthquake are consistent with contemporary GPS and geological timescale deformation.

6.4 Paleoseismicity

Aerial photographs from NZ Aerial Mapping (NZAM 1950), satellite photographs from 2015 (Zekkos *et al.,* in review), InSAR analyses, geomorphological mapping, and a natural trench were all examined to constrain the paleoseismic history of the HF and SLF in the study area.

The Leader River scoured a 2016 rupture on a Late Quaternary terrace (referred to as QT6 for this study) following breach of the landslide dam formed immediately upstream of the Leader Landslide. The resulting natural trench cut through the entire sequence of Late Quaternary cover beds up to several metres thick at a location where the rupture displaced a terrace riser and the fault changes strike by up to ~45°. For these reasons, the interplay between stratigraphy, topography and the fault were difficult to interpret (Fig 5.4), which meant that the timing, number and size of fault displacements was equivocal. Preliminary interpretations of the trench log indicate 2-4 events on the HF in the trench log, including the 2016 event. The interpretation of events depends largely on whether colluvium material mapped in the log formed in response to terrace degradation or fault movement. There are no direct dates to confirm the ages of terraces in the study area, however the high terrace of Qt10 (Last Glacial Maxima surface) is inferred to be ~18 ka (Rattenbury *et al.,* 2006; Fig 5.1). If this assumed age is correct, and rates of river down-cutting have been constant in the Holocene, the terrace surface Qt6 should be mid Holocene in age (~5 ka). This would suggest an event every 2.5-5 ka. The initial results of the Leader River Trench compare well

with ongoing investigations along the western segment for the HF, which suggest maximum recurrence intervals of 5-7ka. Interpretations on the trench log are consistent with pre-earthquake imagery which suggest pre-existing tectonic warps on the Qt10 surface at the locations of 2016 ruptures (Fig 5.10). These tectonic warps formed along the HF. No such pre-earthquake fault scarps have been identified along the SLF suggesting that this fault is probably less active than the HF and may not have ruptured during the Holocene.

6.5 Areas for future research

This study has revealed many preliminary insights about the deformation style, kinematics, and paleoseismicity of the SLF and HF faults in the study area. This is likely to be the first of many studies that will allow us to understand better the southern ruptures from the 2016 event, and the regional tectonics of North Canterbury. Numerous questions remain unresolved in the present study and could be the focus of future work.

1) There are limited outcrop exposures at Woodchester, however this study could benefit from additional field-mapping in areas that are harder to access, such as the steep incised stream beds. Many of the contacts produced in figures 3.4, 3.7, and 3.8 are inferred. Additionally, detailed analyses of fractures, bedding and other pre-existing fabric in the Torlesse at Woodchester Station may help us to understand why The Wall is so steep, and if it is indeed influenced by Torlesse fabric. In addition, there is still work that could be done ensuring that the present mapping and structural data are included regional compilations designed to understand the regional context of the thesis conclusions.
2) Mapping of subsurface strata and fault-zone architecture has the potential to add significantly to our understanding of the rupture geometries and kinematics. Geophysical techniques such as Ground Penetrating Radar (GPR) or shallow seismic reflection surveys are cost effective and could be easily deployed on flat river terraces.
3) The tectonics of the 2016 rupture are locally complicated by deep seated gravitational failures which are diagnosed in this thesis using the magnitudes and sense of slip on surface ruptures. Detailed analysis of these failures is beyond the scope of this work, however, is it clear that these failures are an important aspect of the ground response to seismic shaking. Using the available LiDAR in conjunction with detailed field mapping, it may be possible map out the headwall scarps and pressure ridges in detail and to estimate the magnitude of slip on the faults and bedding planes. Such studies

may provide a basis for more accurate estimates of gravitational versus tectonic slip on the Quarry and Wall faults.

4) Finally, there is still much work to do to characterize the paleoseismic activity of the faults in the study area. The Leader River Trench was more a fortuitous exposure than a paleoseismic trench, and multiple trenches need to be excavated along the SLF before event horizons can be clearly constrained for the entire fault segment. Additionally, dates of the river terraces need to be constrained to place the pre 2016 ruptures in a chronological context. Paleoseismic investigations may also benefit from further analyses using DEMs derived from historic satellite imagery or ortho-photos (see Zekkos *et al.,* in review). By differencing the DEMs from historic imagery with LiDAR following the 2016, pre-existing structures that are not visible to the naked eye may be uncovered, and may aid in the decision of where to excavate trenches.

REFERENCES

Abe, K. (1981) 'Magnitudes of large shallow earthquakes from 1904-1980', *Physics of the Earth and Planetary Interiors*, 27, pp. 72–92.

Allum, J. A. E. (1966) *Photogeology and regional mapping*. Oxford: Pergamon Press.

Anderson, E. M. (1951) *The dynamics of faulting and dyke formation with applications to Britain*. 2d edn. Oliver and Boyd.

Bai, Y., Lay, T., Cheung K. F., and Ye. L., (2017) 'Two regions of seafloor deformation generated the tsunami for the 13 November 2016, Kaikoura, New Zealand earthquake', *Geophysical Research Letters*, 44(13), pp. 6597–6606. doi: 10.1002/2017GL073717.

Baljinnyam, I. (1993) 'Ruptures of major earthquakes and active deformation in Mongolia and its surroundings', *Geological Society of America*, 181, 181.

Barnes, P. M. (1996) 'Active folding of Pleistocene unconformities on the edge of the Australian-Pacific plate boundary zone, offshore North Canterbury, New Zealand', *Tectonics*, 15(3), pp. 623–640. doi: 10.1029/95TC03249.

Barnes, P. M., De Lépinay, B. M., Collot, J. Y., Delteil, J., and Audru, J. C. (1998) 'Strain partitioning in the transition area between oblique subduction and continental collision, Hikurangi margin, New Zealand', *Tectonics*, 17(4), pp. 534–557. doi: 10.1029/98TC00974.

Barrell, D. J. A. and Townsend, D. B. (2012) *General Distribution and characteristics of active faults and folds in the Hurunui District, North Canterbury*. GNS Consultancy Report 2012/113; Environment Canterbury Report R12/39.

Bayer, K. (2016) 'Cost of Kaikoura earthquake up to 3$ billion', *NZ Herald, National*. Available at: http://www.newstalkzb.co.nz/news/national/cost-of-kaikoura-earthquake-up-to-3-billion/.

Beavan, J., Tregoning, P., Bevis, M., Kato, T., and Meertens., C. (2002) 'Motion and rigidity of the Pacific Plate and implications for plate boundary deformation', *Journal of Geophysical Research: Solid Earth*, 107(B10). Available at: 10.1029/2001JB000282.

Beavan, J. and Haines, J. (2001) 'Contemporary horizontal velocity and strain rate fields of the Pacific-Australian plate boundary zone through', 106, pp. 741–770.

Begg, G. J. (2002) 'Geology of the Wairarapa area': Institute of Geological & Nuclear Sciences scale 1:250,000 geological map. Lower Hutt, New Zealand.

Benson, G. M., Oliver, P. A. and Mossley, K. A. (2013) *An Introduction to Geological Structures & Maps*. 8th edn. New York, NY: Routledge.

Brough, Thomas. Masters Student (Geology). Personal Communication, April 2018.

Browne, G. H. and Field, B. D. (1985) *The Lithostratigraphy of Late Cretaceous to Early Pleistocene Rocks of Northern Canterbury, New Zealand*.

Buchanan, J. (1868) *Kaikoura district. New Zealand Geological Survery report of geological explorations* 4: 24-41.

Bull, W. B. (1991) *Geomorphic responses to climate change*. New York, NY: Oxford University Press.

Chu, H. J., Tseng, R. A., and Wang, C. K. (2014) 'Identifying LiDAR sample uncertainty on terrain features from DEM simulation', *Geomorphology*. Elsevier B.V., 204, pp. 325–333. doi: 10.1016/j.geomorph.2013.08.016.

Clark, K. J., Nissen, E. K., Howarth, J. D., Hamling I. J., Mountjoy, J. J., Ries, W. F., Jones, K., Goldstein, S., Villamor, P., Hreinsdóttir, S., Litchfield, N. J., Mueller, C., Berryman, K. R., and Strong, D. T. (2017) 'Highly variable coastal deformation in the 2016 MW7.8 Kaikōura earthquake reflects rupture complexity along a transpressional plate boundary', *Earth and Planetary Science Letters*. Elsevier B.V., 474, pp. 334–344. doi: 10.1016/j.epsl.2017.06.048.

Coe, A. L. (2013) *Geological Field Techniques*. 1st edn. Blackwell Publishing Ltd.

Cowan, H. A. (1989) 'An Evaluation of the Late Quaternary Displacements and Seismic Hazard Associated with The Hope and Kakapo Faults, Amuri District, North Canterbury'. Master of Science (Geology). University of Canterbury.

Cowan, H. A. (1992) 'Structure, seismicity and tectonics of the Porter's Pass-Amberley fault zone, North Canterbury, New Zealand'. Doctor of Philosophy (Geology). University of Canterbury.

Demets, C., Gordon, R. G. and Argus, D. F. (2010) 'Geologically current plate motions', *Geophysical Journal International*, 181(1), pp. 1–80. doi: 10.1111/j.1365-246X.2009.04491.x.

Van Dissen, R. and Yeats, R. S. (1991) 'Hope Fault, Jordan thrust, and uplift of the Seaward Kaikoura Range, New Zealand', *Geology*, 19(4), p. 393. doi: 10.1130/0091-7613(1991)019<0393:HFJTAU>2.3.CO;2.

Donath, F. A. (1961) 'Experimental Study of Shear Failur in Anisotropic Rocks', *GSA Bulletin*, 72(6), pp. 985–989.

Duputel, Z. and Rivera, L. (2017) 'Long-period analysis of the 2016 Kaikoura earthquake', *Physics of the Earth and Planetary Interiors*. Elsevier B.V., 265, pp. 62–66. doi: 10.1016/j.pepi.2017.02.004.

Eberhart-Phillips, D. and Bannister, S. (2010) '3-D imaging of Marlborough, New Zealand, subducted plate and strike-slip fault systems', *Geophysical Journal International*, 182(1), pp. 73–96. doi: 10.1111/j.1365-246X.2010.04621.x.

Finlay, H. J. (1946) 'The microsfaunas of the Oxford Chalk and Eyre River Beds', *Transactions of the Royal Society of New Zealand*, (76), pp. 237–245.

Fletcher, J. M., Oskin, M. E. and Teran, O. J. (2016) 'The role of a keystone fault in triggering the complex El Mayor-Cucapah earthquake rupture', *Nature Geosci*, 9(4), pp. 303–307. doi: 10.1038/NGEO2660.

Fossen, H. (2016) *Structural Geology*. 2nd edn. Cambridge University Press.

Fu, B., Awata, Y., Du, J., Ninomiya, Y., and He, W. (2005) 'Complex geometry and segmentation of the surface rupture associated with the 14 November 2001 great Kunlun earthquake, northern Tibet, China', *Tectonophysics*, 407(1–2), pp. 43–63. doi: 10.1016/j.tecto.2005.07.002.

Furlong, K. P. and Herman, M. (2017) 'Reconciling the deformational dichotomy of the 2016 Mw 7.8 Kaikoura New Zealand earthquake', *Geophysical Research Letters*, 44(13), pp. 6788–6791. doi: 10.1002/2017GL074365.

Fyfe, H. E. (1936) *Fyfe Kaikoura maps 1-50. Unpublished maps.* Institute of Geological & Nuclear Sciences. Lower Hutt, New Zealand.

Geiser, P. A. and Boyer, S. E. (1989) 'Construction of geological cross sections: Techniques, assumptions and methods', *Geology*, 17(4). doi: 10.1130/0091-7613(1989)017<0373:COGCST>2.3.CO;2.

Gray, M. (2018) 'The Leader co-seismic landslide; characterisation, failure mechanics, and the rold of fault rupture'. Professional Masters (Engineering Geology). University of Canterbury.

Gregg, D. (1964) Sheet 18 Hurunui Geological map of New Zealand 1:250000. *NZ Department of Scientific and Industrial Research,* Wellington, New Zealand.

Guralnik, B., Ankjærgaard, C., Jain, M., Murray, A., Müller, A., Wälle, M., Lowick, S. E., Presuuer, F., Rhodes, E. J., Wu, T.S., Matthew, G., and Herman, F. (2015) 'OSL-thermochronometry using bedrock quartz: A note of caution', *Quaternary Geochronology*, 25, pp. 37–48. doi: 10.1016/j.quageo.2014.09.001.

Hamling, I. J., Hreinsdóttir, S., Clark, K., Elliot, J., Liang, C., Fielding, E., Litchfield, N. J., Villamor, P., Wallace, L., Wring, T. J., D'Anastasio, E., Bannister, S., Burbidge, D., Denys, P., Gentle, P., Howarth, J., Mueller, C., Palmer, N., Pearson, C., Power, N., Barnes, P. M., Barrel, D. J. A., Van Dissen, R., Little, T., Nicol, A., Pettinga, J., Rowland, J., and Stirling, M., (2017) 'Complex multifault rupture during the 2016 Mw 7.8 Kaikōura earthquake, New Zealand', *Science*, 356(6334). doi: 10.1126/science.aam7194.

Hoare, B. (2017) 'Shallow GPR Imaging of the 2016 Kaikoura Earthquake Ruptures'. Professional Masters (Engineering Geology). University of Canterbury.

Hollingsworth, J., Ye, L. and Avouac, J. P. (2017) 'Dynamically triggered slip on a splay fault in the Mw7.8, 2016 Kaikoura (New Zealand) earthquake', *Geophysical Research Letters*, 44(8), pp. 3517–3525. doi: 10.1002/2016GL072228.

Jarrard, R. D. (1986) 'Terrane motion by strike-slip faulting of forearc slivers', *Geology*, pp. 780–783.

Jiwen, W. U., Xuemeng, H. and Furen, X. I. E. (2017) 'Deformation of the Most Recent Co-seismic Surface Ruptures Along the Garzê – Yushu Fault Zone (Dangjiang Segment) and Tectonic Implications For the Tibetan Plateau', 91(2).

Johnson, K. M. (2018) 'Growth of Fault-Cored Anticlines by Flexural Slip Folding: Analysis by Boundary Element Modeling', *Journal of Geophysical Research: Solid Earth*, (2013), pp. 2426–2447. doi: 10.1002/2017JB014867.

Kaiser, A., Fry, B., Holden, C., Litchfield, L. J., Gerstenberger, M., D'Anastasio, E., Horspool, N., McVerry, G., Ristau, J., Bannister, S., Christohphersen, A., Clark, K., Power, W., Rhoades, D., Massey, C., Hamling, I. J., Wallace, L., Mountjoy, J. J., Kaneko, Y., Benites, R., Van Houtte, C., and Dellow, S. (2017) 'The 2016 Kaikōura, New Zealand, Earthquake: Preliminary Seismological Report', *Seismological Research Letters*, 88(3), pp. 727–739. doi: 10.1785/0220170018.

Kanamori, H. and Anderson, D. L. (1975) 'Theoretical Basis of Some Empirical Relations in Seismology', *Bulletin of the Seismological Society of America*, 65(5), pp. 1073–1095.

Kars, R. H., Reimann, T. and Wallinga, J. (2014) 'Are feldspar SAR protocols appropriate for post-IR IRSL dating?', *Quaternary Geochronology*. Elsevier B.V, 22, pp. 126–136. doi: 10.1016/j.quageo.2014.04.001.

Kelly, Rebecca. Landowner of Woodchester Station. Personal Communication, March 2017.

Kearse, J., Little, T., Van Dissen, R., Landgridge, R., Mountjoy, J. J., Ries, W., Villamor, P., Clark, K., Benson, A., Lamarche, G., Hill, M., and Hemphill-Haley, M. (2018) 'Onshore to Offshore Ground-Surface and Seabed Rupture of the Jordan – Kekerengu – Needles Fault Network during the 2016 M w 7 . 8 Kaikoura Earthquake , New Zealand' *Bulletin of the Seismological Society of America*. doi: 10.1785/0120170304.

Khajavi, Narges. Post Doctorial Fellow (Geology), and Pettinga, Jarg. Professor (Geology). Personal Communication, March, 2017

King, G. E., Sanderson, D. C. W., Robinson, A. J., and Finch, A. A. (2014) 'Understanding processes of sediment bleaching in glacial settings using a portable OSL reader', *Boreas, An International Journal of Quaternary Research*. doi: 10.1111/bor.12078.

Langridge, R. M., Rowland, J. R., Villamor, P., Mountjoy, J. J., Townsend, D. B., Nissen, E., Madugo, C., Ries, W., Gasston, C., Hall, B., Canva, A., Hatem, A. E., and Hamling, I. J. (2016) 'The New Zealand Active Faults Database', *New Zealand Journal of Geology and Geophysics*, 59(1), pp. 86–96. doi: 10.1080/00288306.2015.1112818.

Langridge, R. M., Rowland, J. V and Villamor, P. (2018) 'Bulletin of the Seismological Society of America Co-seismic rupture and preliminary slip estimates for the Papatea fault and its role in', *Bulletin of the Seismological Society of America*.

Lin, A., Ouchi, T., Chen, A., and Maruyama, T. (2001) 'Co-seismic displacements, folding and shortening structures along the chelungpu surface rupture zone occurred during the 1999 Chi-Chi (Taiwan) earhtquake', *Tectonophysics*, 330(3–4), pp. 225–244. doi: 10.1016/S0040-

1951(00)00230-4.

Lin, A. and Nishikawa, M. (2007) 'Coseismic lateral offsets of surface rupture zone produced by the 2001 Mw7.8 Kunlun earthquake, Tibet from the IKONOS and QuickBird imagery', *International Journal of Remote Sensing*, 28(11), pp. 2431–2445. doi: 10.1080/01431160600647233.

Litchfield, N. J. (1995) 'Structure and Tectonic Geomorphology of the Lowry Peaks Range-Waikari Valley District, New Zealand '. Master of Science (Geology). University of Canterbury

Litchfield, N. J., Campbell, J. K. and Nicol, A. (2003) 'Recognition of active reverse faults and folds in North Canterbury, New Zealand, using structural mapping and geomorphic analysis', *New Zealand Journal of Geology and Geophysics*, 46(4), pp. 563–579. doi: 10.1080/00288306.2003.9515030.

Litchfield, N. J., Van Dissen, R., Sutherland, R., Barnes, P. M., Cox, S. C., Norris, R., Beavan, R. J., Langridge, R., Villamor, P., Berryman, K., Stirling, M., Nicol, A., Nodder, s., Lamarche, G., Barrell, D. J. A., Pettinga, J., Little, T., Pondard, N., Mountjoy, J. J., and Clark, K. (2014) 'A model of active faulting in New Zealand', *New Zealand Journal of Geology and Geophysics*. Taylor & Francis, 57(1), pp. 32–56. doi: 10.1080/00288306.2013.854256.

Litchfield, N. J., Villamor, P., Van Dissen, R., Nicol, A., Barnes, P. M., Barrell, D. J. A., PEttinga, J., Langridge, R., Little, T., Mountjoy, J. J., Ries, W., Rowland, R. J., Fenton, C., Stirling, M., Kearse, J., Berryman, K. J., Cochran, U. A., Clark, K., Hemphill-Haley, M., Khajavi, N., Jones, K. E., Archibald, G., Upton, P., Asher, C., Benson, A., Cox. S. C., Gasston, C., Hale, D., Hall, B., Hatem, A. E., Heron, D. W., Howarth, J., Kane, T. J., Lamarche, G., Lawson, S., Lukovic, B., McColl, S. T., Madugo, C., Manousakis, J., Noble, D., Pedley, K., Sauer, K., Stahl, T., Strong, D. T., Townsend, D. T., Toy, V., Williams, J., Woelz, S., and Zinke, R. (2018) 'Surface Rupture of Multiple Crustal Faults in the Mw 7.8 2016 Kaikōura Earthquake, New Zealand', *Bulletin of the Seismological Society of America*.

Mason, B. H. (1949) 'The geology of the Mandamus-Pahau District, North Canterbury', *Transactions of the Royal Society of New Zealand*, 77, pp. 403–428.

Massey, C., Massey, C., Townsend, D., Rathje, E., Allstadt, K. E., Lukovic, B., Kaneko, Y., Bradley, B., Wartman, J., Jibson, R. W., Petley, D. N., Horspool, N., Hamling, I., Carey, J., Cox, S., Davidson, J., Dellow, S., Godt, J. W., Holden, C., Jones, K., Kaiser, A., Little, M., Lyndsell, B., McColl, S., Morgenstern, R., Rengers, F. K., Rhoades, D., Rosser, B., Strong, D., Singeisen, C., and Villeneuve, M. (2018) 'Landslides Triggered by the 14 November 2016 Mw 7.8 Kaikoura Earthquake, New Zealand', *Bulletin of the Seismological Society of America*, XX(Xx). doi: 10.1785/0120170305.

McAlpin, J. (2009) *Paleoseismology*. 2nd edn. Academic Press.

McCaffrey, R. (1992) 'Oblique plate convergence, slip vectors, and forearc deformation', *Journal of Geophysical Research: Solid Earth*, 97(6).

McMorran, T. J. (1991) 'The Hope Fault at Hossack Station east of Hanmer Basin, North

Canterbury'. Master of Science (Engineering Geology). University of Canterbury

Miller, D. J. and Dunne, T. (1996) 'Topographic perturbations of regional stresses and consequent bedrock fracturing', *Journal of Geophysical Research: Solid Earth*, 101(B11), pp. 25523–25536. doi: 10.1029/96JB02531.

Mould, R. (1992) 'Structure and Kinematics of Late Cenozoic Deformation along the Western Margin of the Culverden Basin , North Canterbury , New Zealand . By'.

Nicol, A. and Wise, D. (1992) 'Paleostress adjacent to the Alpine fault of New Zealand: Fault, Vein, and Styolite data from the Doctors Dome area', *Journal of Geophysical Research*, 97, pp. 17685–17692. doi: 10.1029/92JB01201.

Nicol, A. (1991) 'Structural styles and kinematics of deformation on the edge of New Zealand plate boundary zone, mid-Waipara region, North Canterbury', p. 171. Doctor of Philosophy (Geology). University of Canterbury

Nicol, A., Khajavi, N., Pettinga, J.R., Fenton, C., Stahl, T., Bannister, S., Pedley, K., Hyland-Brook, N., Bushell, T., Hamling, I., Ristau, J., Noble, D., and McColl, S. T. (2018) 'Preliminary geometry, slip and kinematics of fault ruptures during 1 the 2016 MW 7.8 Kaikōura Earthquake in the North Canterbury region of New Zealand', *Bulletin of the Seismological Society of America*. doi: 10.1785/0120170329.

Nicol, A., Alloway, B. and Tonkin, P. (1994) 'Rates of deformation, uplift, and landscape development associated with active folding in the Waipara area of North Canterbury, New Zealand', *Tectonics*, 13(6), pp. 1327–1344. doi: 10.1029/94TC01502.

Nicol, A. and Nathan, S. (2001) 'Folding and the formation of bedding-parallel faults on the western limb of Grey Valley Syncline near Blackball, New Zealand', *New Zealand Journal of Geology and Geophysics*, 44(1), pp. 127–135. doi: 10.1080/00288306.2001.9514929.

Noble, D. P. (2011) 'Tectonic geomorphology and paleoseismicity of the Northern Esk Fault, North Canterbury, New Zealand'. Master of Science (Geology). University of Canterbury

Noh, M. J. and Howat, I. M. (2015) 'Automated stereo-photogrammetric DEM generation at high latitudes: Surface Extraction with TIN-based Search-space Minimization (SETSM) validation and demonstration over glaciated regions', *GIScience and Remote Sensing*. Taylor & Francis, 52(2), pp. 198–217. doi: 10.1080/15481603.2015.1008621.

Noh, M. J. and Howat, I. M. (2017) 'The Surface Extraction from TIN based Search-space Minimization (SETSM) algorithm', *ISPRS Journal of Photogrammetry and Remote Sensing*. International Society for Photogrammetry and Remote Sensing, Inc. (ISPRS), 129, pp. 55–76. doi: 10.1016/j.isprsjprs.2017.04.019.

Peacock, D. C. P. and Sanderson, D. J. (1992) 'Effects of layering and anisotropy on fault geometry', *Journal of the Geological Society*, 149(5), pp. 793–802. doi: 10.1144/gsjgs.149.5.0793.

Pettinga, J. R. Yetton, M. D., Van Dissen, R., and Downes, G. (2001) 'Earthquake source identification and characterisation for the Canterbury region, South Island, New Zealand', *Bulletin of the New Zealand Society for Earthquake Engineering*, pp. 282–317.

Philip, H. and Meghraoui, M. (1983) 'Structural Analysis and Interpretation of the Surface Deformations of the El Asnam Earthquake of October 10, 1980', *October*, 2(1), pp. 17–49.

Powers, W. E. (1962) *Terraces of the Hurunui River, New Zealand*. Northwestern University.

Preusser, F., Ramseyer, K. and Schlüchter, C. (2006) 'Characterisation of low OSL intensity quartz from the New Zealand Alps', *Radiation Measurements*, 41(7–8), pp. 871–877. doi: 10.1016/j.radmeas.2006.04.019.

Quigley, M., Van Dissen, R., Litchfield, N.J., Villamor, P., Duffy, B., Barrell, D., Furlong, K., Stahl, T., Bilderback, E., Noble, D. (2012) 'Surface rupture during the 2010 Mw7.1 darfield(canterbury) earthquake: Implications for fault rupture dynamics and seismic-hazard analysis', *Geology*, 40(1), pp. 55–58. doi: 10.1130/G32528.1.

Rattenbury, M. S., Townsend, D. B. and Johnston, M. R. (2006) 'Geology of the Kaikoura area', Institute & Geological and Nuclear Sciences 1:250,000 Geological Map. Lower Hutt, New Zealand

Reyners, M. and Cowan, H. (1993) 'The transition from subduction to continental collision; crustal structure in the North Canterbury Region, New Zealand', *Geophysical Journal International*, 115(3), pp. 1124–1136. doi: 10.1111/j.1365-246X.1993.tb01514.x.

Rhodes, E. J. (2015) 'Dating sediments using potassium feldspar single-grain IRSL: Initial methodological considerations', *Quaternary International*. Elsevier Ltd, 362, pp. 14–22. doi: 10.1016/j.quaint.2014.12.012.

Rhodes, E. J. and Pownall, L. (1994) 'Zeroing of the OSL signal in quartz from young glaciofluvial sediments', *Radiation Measurements*, 23(2–3), pp. 581–585.

Rodgers, D. W. and Little, T. A. (2006) 'World's largest coseismic strike-slip offset: The 1855 rupture of the Wairarapa Fault, New Zealand, and implications for displacement/length scaling of continental earthquakes', *Journal of Geophysical Research: Solid Earth*, 111(12), pp. 1–19. doi: 10.1029/2005JB004065.

Scholz, C. H. (2002) *The Mechanics of Eathquakes and Faulting*. 2nd edn. Cambridge: Cambridge University Press.

Scholz, C. H., Aviles, C. and Wesnousky, S. (1986) 'Scaling differences between large intraplate and interplate earthquakes', *Bulletin of the Seismological Society of America*, 76(1), pp. 65–70.

Shean, D. E., Oleg, A., Moratto, Z. M., Smith, B. E., Joughin, I. R., Porter, C. and Morin, P. (2016) 'An automated, open-source pipeline for mass production of digital elevation models (DEMs) from very-high-resolution commercial stereo satellite imagery', *ISPRS Journal of Photogrammetry and Remote Sensing*. International Society for Photogrammetry and Remote Sensing, Inc. (ISPRS), 116, pp. 101–117. doi: 10.1016/j.isprsjprs.2016.03.012.

Sibson, R., Ghisetti, F. and Ristau, J. (2011) 'Stress Control of an Evolving Strike-Slip Fault System during the 2010-2011 Canterbury, New Zealand, Earthquake Sequence', *Seismological Research Letters*, 82(6), pp. 824–832. doi: 10.1785/gssrl.82.6.824.

Sibson, R. H., Ghisetti, F. C. and Crookbain, R. A. (2012) 'Andersonian wrench faulting in a regional stress field during the 2010 – 2011 Canterbury , New Zealand , earthquake sequence', pp. 7–18.

Sieh, K. E. (1978) 'Slip along the San Andreas fault associated with the great 1857 earthquake', *Bulletin of the Seismological Society of America*, 68(5), p. 1421.

Sieh, K. E. and Jahns, R. H. (1984) 'Holocene activity of the San Andreas fault at Wallace Creek, California Holocene activity of the San Andreas fault at Wallace Creek, California', *Geological Society of America Bulletin*, (8), pp. 883–896. doi: 10.1130/0016-7606(1984)95<883.

Smith, B. W., Rhodes, E.J., Stokes, S., Spooner, N.A., and Aitken, M.J. (1990) 'Optical dating of sediments: Initial quartz results from Oxford', *Archaeometry*, 32(1), pp. 19–31. doi: 10.1111/J1475-4754.1990.TB01078.X.

Smith, J. (2017) 'Differentiating gravitational and tectonic features from the 2016 Kaikoura Earthquake: Development of a systematic process.'. Professional Masters (Engineering Geology). University of Canterbury.

Speight, R. (1918) 'Structure and Glacial Features of the Hurunui Valley.', *Transactions of the New Zealand Institute*, (50), pp. 93–105.

Srivastava, P., Bhakuni, S. S., Luirei, K., and Misra, D. K. (2008) 'Morpho-sedimentary records at the Brahmaputra River exit, NE Himalaya: climate–tectonic interplay during the Late Pleistocene–Holocene', *Journal of Quaternary Science*, 24(2), pp. 175–188. doi: 10.1002/jqs.1190.

Stein, R. S. and King, G. C. P. (1984) 'Seismic Potential Revealed by Surface Folding : 1983 Coalinga , California , Earthquake Author (s): Ross S . Stein and Geoffrey C . P . King Published by : American Association for the Advancement of Science Stable URL : http://www.jstor.org/stable/1692', 224(4651), pp. 869–872.

Stein, R. S. and Yeats, R. S. (1989) 'Hidden Earthquakes', *Scientific American*, 260(6), p. 48.
Stirling, M. *et al.* (2013) 'Selection of earthquake scaling relationships for seismic-hazard analysis', *Bulletin of the Seismological Society of America*, 103(6), pp. 2993–3011. doi: 10.1785/0120130052.

Stirling, M. W., Litchfield, N. J., Villamor, P., Van Dissen, R. J., Nicol, A., Pettinga, J., Barnes, P., Langridge, R. M., Little, T., Barrell, D. J. A., Mountjoy, J., Ries, W. F., Rowland, J., Fenton, C., Hamling, I., Asher, C., Barrier, A., Benson, A., Bischoff, A., Borella, J., Carne, R., Cochran, U. A., Cockroft, M., Cox, S. C., Duke, G., Fenton, F., Gasston, C., Grimshaw, C., Hale, D., Hall, B., Hao, K. X., Hatem, A., Hemphill-Haley, M., Heron, D. W., Howarth, J., Juniper, Z., Kane, T., Kearse, J., Khajavi, N., Lamarche, G., Lawson, S., Lukovic, B., Madugo, C., Manousakis, I., McColl, S., Noble, D., Pedley, K., Sauer, K., Stah,

T., Strong, D. T., Townsend, D. B., Toy, V., Villeneuve, M., Wandres, A., Williams, J., Woelz, S., and Zinke, R. (2017) 'The Mw7.8 2016 Kaikōura earthquake: Surface fault rupture and seismic hazard context', *Bulletin of the New Zealand Society for Earthquake Engineering*, 50(2), pp. 73–84.

Suggate, R. S. (1957) 'The geology of Reefton subdivision.' *New Zealand Geological Survey Bulletin 56.*

Tchalenko, J. S. and Ambraseys, N. N. (1970) 'Structural Analysis of the Dasht-e-Bayaz (Iran) Earthquake Fractures', *GSA Bulletin*, 81(1), pp. 41–70. doi: https://doi.org/10.1130/0016-7606(1970)81[41:SAOTDB]2.0.CO;2.

Walcott, R. (1978) 'Present tectonics and late Cenozoic evolution of New Zealand', *Geophysical Journal of the Royal Astronomical Society*, 52(May), pp. 137–165.

Walcott, R. I. (1998) 'Modes of oblique compression: Late cenozoic tectonics of the South Island of New Zealand', *Reviews of Geophysics*, 36(1), pp. 1–26. doi: 10.1029/97RG03084.

Wallace, L. M., Beavan, J., McCaffrey, R., Berryman, K., and Denys, P. (2007) 'Balancing the plate motion budget in the South Island, New Zealand using GPS, geological and seismological datas', *Geophysical Journal International*, 168(1), pp. 332–352. doi: 10.1111/j.1365-246X.2006.03183.x.

Wallace, L. M., Barnes, P., Beavan, J., Van Dissen, R., Litchfield, N., Mountjoy, J., Langridge, R., Lamarche, G., and Pondard, N. (2012) 'The kinematics of a transition from subduction to strike-slip: An example from the central New Zealand plate boundary', *Journal of Geophysical Research: Solid Earth*, 117(2). doi: 10.1029/2011JB008640.

Wang, T., Wei, S., Shi, X., Qiu, Q., Li, L., Peng, D., Weldon, R. J. and Barbot, S. (2018) 'The 2016 Kaikōura earthquake: Simultaneous rupture of the subduction interface and overlying faults', *Earth and Planetary Science Letters*. Elsevier B.V., 482, pp. 44–51. doi: 10.1016/j.epsl.2017.10.056.

Warren, G. (1995) 'Geology of the Parnassus area'. Institute of Geological & Nuclear Sciences 1:50 000 geological map. 1 sheet +36p. Lower Hutt, New Zealand.

Wesnousky, S. G. (2008) 'Displacement and geometrical characteristics of earthquake surface ruptures: Issues and implications for seismic-hazard analysis and the process of earthquake rupture', *Bulletin of the Seismological Society of America*. doi: 10.1785/0120070111.

Wilson, D. D. (1963) 'The Geology of the Waipara Subdivison', *New Zealand Geological Survey Bulletin 64*.

Xu, X., Chen, W., Ma, W., Yu, G., and Chen, G. (2002) 'Surface rupture of the Kunlunshan earthquake (M_s 8.1), northern Tibetan plateau, China', *Seismol. Res. Lett*, 73(November), pp. 884–892. doi: 10.1785/gssrl.73.6.884.

Yetton, M. D. (1998) 'Progress in understanding the paleoseismicity of the central and northern Alpine Fault, Westland, New Zealand', *New Zealand Journal of Geology and Geophysics*, 41(4), pp. 475–483. doi: 10.1080/00288306.1998.9514824.

Zekkos, D., Clark, M., Willis, M., Athanasopoulos-Zekkos, A., Manousakis, J., Knoper, L Stahl, T., Massey, C., Archibald, G., Greenwood, W., and Medwedeff, W. (2018) '3D Models of the Leader Valley Using Satellite & UAV Imagery Following the 2016 Kaikoura Earthquake', *U.S. National Conference On Earthquake Engineering*.

APPENDICES

APPENDIX A: Map of Surrounding Townships

Figure A1: Map depicting townships surround Woodchester Station (shown in the black box) and the location of the 2016 event epicentre. Map supplied by NZ topo;

APPENDIX B: Fault Displacement data

Table B1: Spreadsheet containing raw data for figure 4.2

Fault Length (km)	(cm)	(cm)	H_Disp (cm)	Sense	Side up
0.02	20	5	0	reverse	West
0.05	75	15		reverse	west
0.19	90	10		reverse (Dextral?)	west
0.207	45	15		reverse (Dextral?)	west
0.26	80	10	8	Reverse (Dextral?)	west
0.45	90	10		reverse dextral (?)	west
0.46	96	10		reverse dextral?	west
0.68	110	10		thrust	west
1.04	22	10			northwest
1.06	33	10	5	Sinistral Reverse	northwest
1.16	34	10	16	Sinistral Reverse	northwest
2.25	131	10		sinitral reverse	EAST
2.26	144	10			EAST
2.27	123	10		sinistral reverse	EAST
2.28	122	15		sinistral reverse	east side up
2.31	50	15			east side up
2.32	80	12		sinistral reverse	east side up
2.36	50	10	12		
2.72	0	0	70		east side up
2.82	0	0	50		east side up
2.89	23	5	23		east side up
2.89	70	10			west up
3.05	100	10			west up
3.14	50	5			
3.15	17	5		sinistral reverse	west up

3.15	40	5		sinistral reverse	west up
3.31	50	5	70	sinistral reverse	west up
3.49	30	5	120		east up
3.59			234	sinistral reverse	
3.82			75	sinistral reverse	east up
3.86	200	20		sinistral reverse	east up
3.87	100	10	220	sinistral reverse	west
3.93	40	5		sinistral reverse	west up
3.96			225	sinistral reverse	West up
4.02	200	20		sinistral reverse	east up
4.06	200	20			east up
4.06	10	2			west up
4.06	65	5		sinistral reverse	west up
4.12			200	sinistral reverse	west up
4.13	165	20	213	sinitral reverse	west up
4.16	310	10	210	sinistral reverse	west up
4.19	310	10	210	sinistral reverse	west up
4.19	10	2	6		west up
4.194	340	5		normal/lef-lateral	west up
4.2	240	10	10	normal left-lateral	west up
4.24	340	5		normal left-lateral	west up
4.31	240	10		normal left lateral	west up
4.34	130	10		normal left-lateral	west up
4.34	100	10		normal left-lateral	west up
4.35			320	normal left-lateral	west up
4.36	195	10	160	normal left-lateral	west up
4.37			305	normal left lateral	west up
4.4			140	notmal left lateral	west up
4.41			140	normal left lateral	west up
4.46	170	10	165	reverse left-lateral	west up

				reverse left-lateral-preluding horrible	
4.46	50	15	80	splay	west up
4.52	20	5	12	left-lateral	west up
4.53	14	3	8	reverse left-lateral	west up
4.54	20	3	12	reverse left-lateral	west up
4.62			110	reverse left lateral	west up
4.63	60	3		reverse	west up
4.78	14	5	16	reverse left lateral	west up
4.79	10	3	20	reverse left lateral	west up
4.8	18	3	18	reverse left-lateral DISPLACEMENTS; FID 7	westup
4.8	70	10		reverse left-lateral DISPLACEMENTS; FID 9	
4.9	10	2			
5	50	2		FID 24 displacements	
5.03	20	10		reverse SOUTHLEADER FID 10	
5.1	30	10		reverse	
5.19	18	3		reverse SOUTHLEADER FID 12	
5.23	40	10	20	left-lateral reverse MAY 4 POINTS; FID 2	
5.23	20	5		LEFT LATERAL REVERSE	
5.26	40	10		LEFT LATERAL REVERSE	

5.27	25	2		LEFT LATERAL REVERSE
5.27			39	
5.3	40	5	10	left-lateral reverse SOUTH LEADER fid 44
5.32	17	5	14	left-later reverse south leader FID 15
5.35	20	5	17	left-lateral reverse south leader FID 14
5.4			35	left-lateral reverse south leader FID 42
5.4	150	20	110	normal left-lateral SOUTH LEADER FID 35
5.53	150	20		normal left-lateral SOUTH LEADER fid 36
5.55	30	5		reverse left-lateral may 4th FID 1
5.6	20	0		reverse left-lateral south leader FID 41
5.6	20	5		reverse left-lateral MAY 4TH fid 0
5.8	20	5	7	reverse-left lateral southr leader FID 43
5.8	110	10	50	normal left-lateral south leader FID 37

				normal left lateral SOUTH LEADER FID	
5.85	100	10		38	
5.76	50	5		normal left lateral SOUTHER LEADER FID 40	
6.6	14	5		LEFT-LATERL REVERSE	
6.66	53	6		left lateral reverse MAY 4TH fid 1	east up
6.73	44	6		left lateral reverse MAY 5 FID 7	east up
6.75	44	7		left-lateral reverse MAY 5 FID 6	east up
6.75	42	2		LEFT LATERAL REVERSE MAP 5 FID 2	east up
6.75	30	5		LEFT LATERAL REVERSE- PHOTO	east up
6.75	56	5		LEFT LATERAL REVERSE- MAY 5 FID 4	east up
6.751			14	left lateral reverse may 5 fid 3	east up
6.76	80	10		left-lateral reverse PHOTO	east up
6.76	30	10		LEFT LATERAL REVERSE PHOTO	east up

APPENDIX C: Rake Calculation Spread Sheet

Table C1: Spreadsheet for calculating rake angle when displacements and fault orientation is known. Created by Narges Khajavi and Andy Nicol

Slip Sense	Strike slip	Uncertaint	Vertical	Uncertai_1	Strike & Dip	Striations	Rake Angle
Reverse dextral	0.15	0	1.2	0	032/80 NW	R:70-78 SW	84.94888
Thrust Dextral	0.08	0	0.9	0	237/45NW		86.4035
Dextral normal?	0.2	0	0.15	0.05	047/80 SE		36.97482
Left-lateral reverse	0.7	0.1	0.3	0.1	338/85E		23.2778
Reverse left-lateral	2.5	0	2.5	0.05	351/83E	TP: 035/58	45.10924
Reverse	0.01	0	0.6	0	198/60W		89.1731
Reverse	0.45	0.8	0.2	0	290/70NE		25.31266
Reverse left-lateral	0	0	3.4	0	345/80E	TP: 031/60	
Reverse left-lateral	0	0	2.4	0.1	350/81E	TP: 032/62	
Reverse left-lateral	1.6	0	1.95	0.05	359/75E	TP: 029/52	51.9515
Dextral Reverse	1	0	0.45	0	222/73 NW		25.50631
Reverse Dextral	1	0	1.5	0	062/71 SE		58.16177
Dextral Reverse	0	0	0.3	0	321/64 NE		
Thrust	0.01	0	0.8	0.1	240/24 NW		89.2905
Thrust	0.01	0	1	0	240/40 NW		89.4324
Reverse	0.01	0	0.6	0	180/55W		89.05403
Reverse	0.01	0	0.4	0	230/60W		88.58119
Thrust Dextral	0.08	0	0.75	0.15	220/25 NW		83.96747

Humps west 1	2	0.4	080/75S	082/11	11.41289
Humps west 2	2	0.769231	080/75S	085/21	21.21674
Humps east	2	4	055/60NW		63.6476
Leader	2	2.8	020/70W		54.71408
Conway-Charwell	0.3	1	075/80N		73.44693
Stone Jug	2	1.212121	165/85E		31.4552

APPENDIX D: Raw Trench Logs

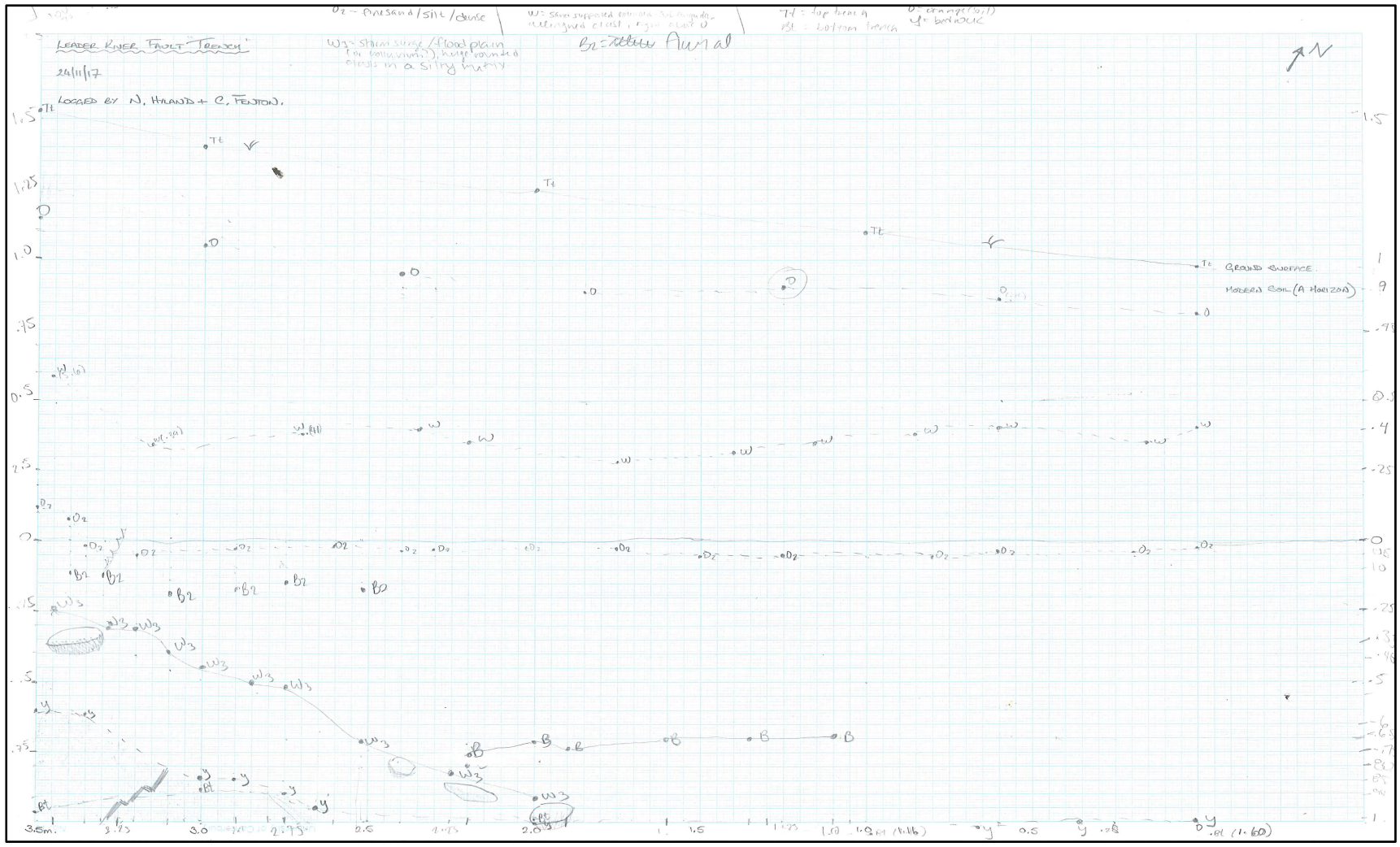

Figure D1: Raw log for 0-3.5m (right, undisturbed stratigraphy) for Fig 5.4

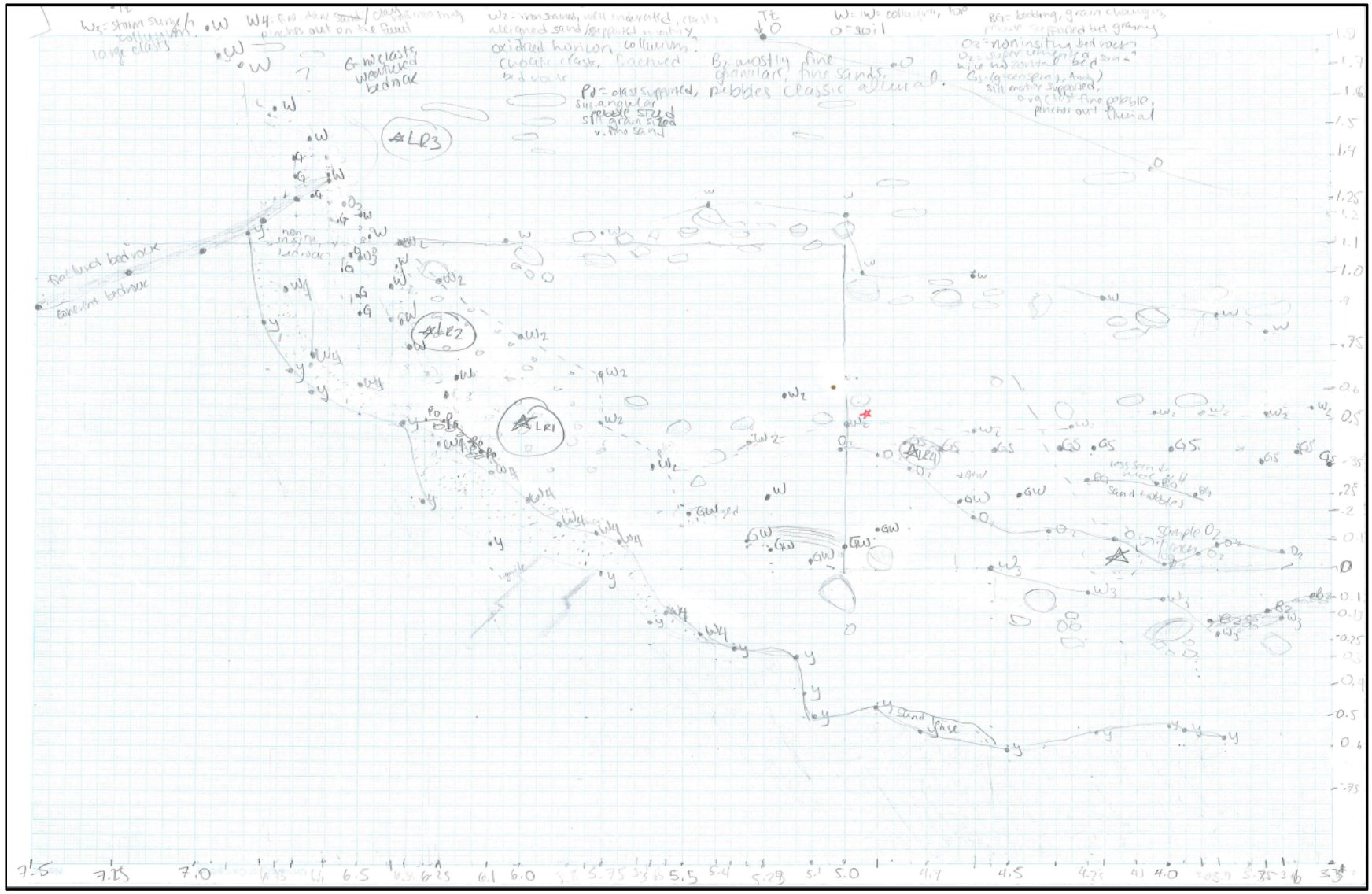

Figure D2: Raw log for 3.5- 7.5m (left, disturbed stratigraphy) for Fig 5.4

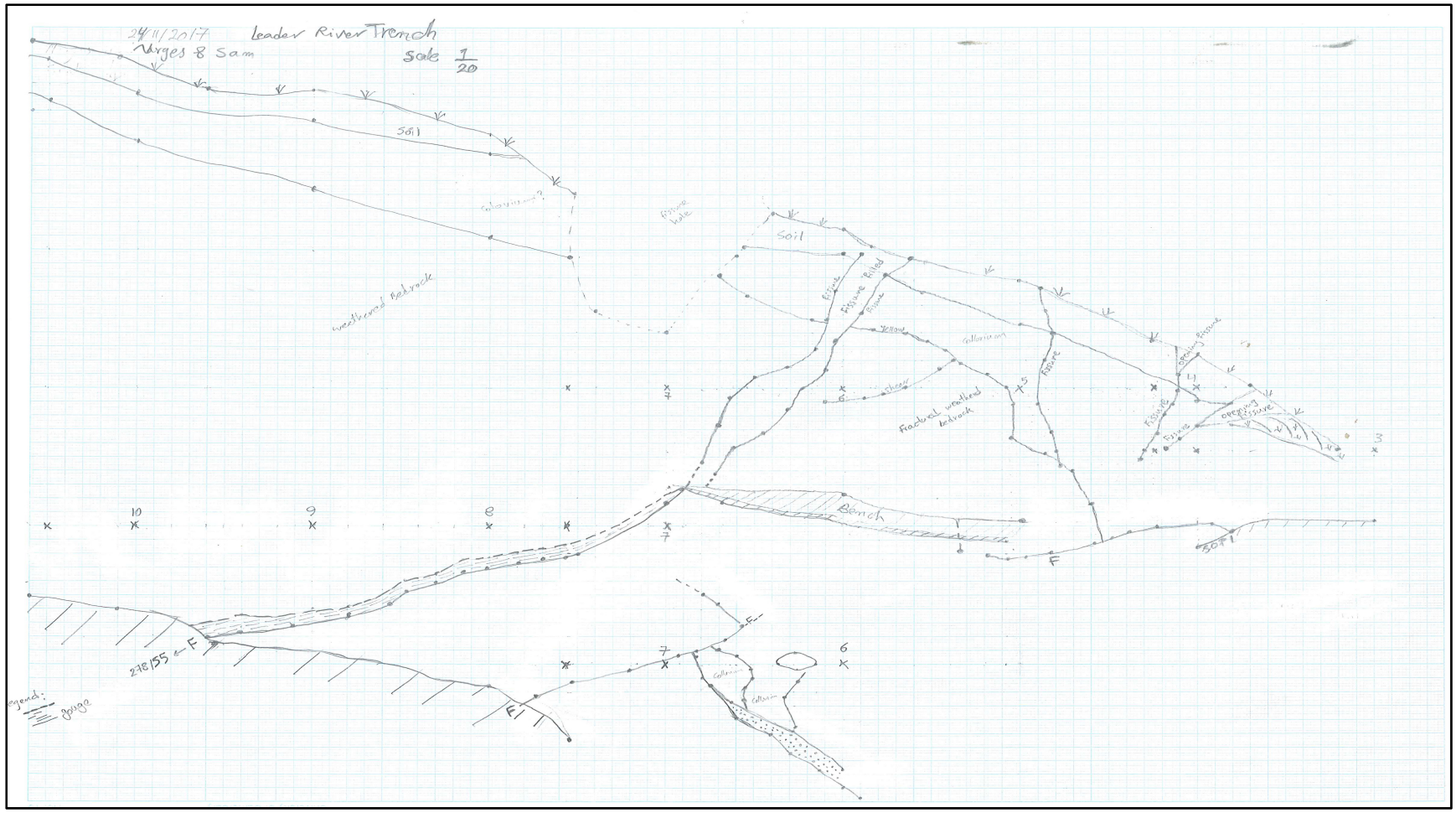
24/11/2017 Leader River Trench
Nyges & Sam
Scale 1/20
Soil
weathered bedrock
Soil
Fracture Filled
Fracture
Fracture
Fracture

APPENDIX E: OSL Dating Lab Report

Report No. 6/18

Luminescence Dating Technical Report

Luminescence Dating Laboratory
School of Geography, Environment and Earth Sciences
Victoria University of Wellington
Wellington New
Zealand

Reported by: Ms. Ningsheng Wang
Date of Issue: 06-04-2018
Contact: Room 414
Cotton Building
Victoria University of Wellington
Ph: (04) 463 6127

CONTENTS

1. SUMMARY

Tow samples (Field code: LR4 and LR5) were submitted for luminescence dating by Natalie Hyland-Brook, Department of Geology, University of Canterbury. The laboratory codes of the samples are WLL1289 and WLL1290 respectively.

The fine grain (4-11µm) preparation technique was used. The blue luminescence was measured during infrared stimulation of fine grain feldspar. The luminescence ages were determined by Single Aliquot Regenerative method (SAR). The dose rate was determined on the basis of ICP-MS.

2. SAMPLE PREPARATION

The sample preparation consisted of two parts:

(i) Preparation for measurement of equivalent dose (equivalent to the paleodose) (ii) Preparation for measurement of dose rate

Part 1: The Preparation for Measurement of Equivalent Dose (D_e)

1. Chemical Treatment

Samples had their outer surfaces removed. Of this removed outer scrapings, 100g was weighed and dried in an oven in preparation for gamma spectrometer analysis. A plastic cube was then filled with remaining scrapings in preparation for water content measuring.

"Fresh" sample material, that had outer surfaces removed earlier (unexposed light sample material), was treated in 10% HCl. This was carried out overnight until all carbonate was removed by the reaction. Following this treatment the sample was further reacted overnight with 10% H_2O_2 in order to remove organic matter.

The next step involved 200ml CBD* solution being added to the sample for 12 hours to remove iron oxide coatings. Note, after every chemical treatment procedure distilled water was used to wash the sample several times.

*CBD solution: 71g sodium citrate, 8.5 g sodium bicarbonate, and 2g sodium dithionate per litre of distilled water

2. Fine Grain Technique (4-11µm)

After chemical treatment, calgon solution (1g sodium hexametaphosphate per litre distilled water) was added to make thick slurry. This slurry was placed into an ultrasonic bath and

mechanically agitated for an hour. The sample was then placed into a 1L measuring cylinder, filled with a certain amount of distilled water to separate out the 4-11μm grains according to Stokes' Law.

The 4-11μm grains were then rinsed with ethanol and acetone and a suspension of these grains were then deposited evenly onto 70 aluminium disks.

Part 2: The Preparation of Measurement of Dose Rate

The dry, ground and homogenised sample materials were submitted to the Geochemistry Laboratory, Victoria University of Wellington for the determination of ^{238}U, ^{232}Th and ^{40}K contents by ICP-MS

3. MEASUREMENTS

Luminescence age was determined by two factors: the equivalent dose (D_e) and the dose rate.
Equivalent dose: obtained from the lab equivalents to the paleodose absorbed by samples during the burial time in the natural environment since their last exposure to the light. Dose rate: amount dose received by the sample each year.

Part 1: Determination of Equivalent Dose (D_e)

D_e was obtained by using SAR.

Single Aliquot Regenerative Method (SAR)

The Single Aliquot Regenerative Method (SAR) was used to determine the equivalent doses. This technique is described by Murray and Wintle (2000).

For the SAR method, a number of aliquots (disks) were subjected to a repetitive cycle of irradiation, preheating and measurement. Firstly, natural shining down curves was measured after preheating. Then shining down curves were measured for the next four or five cycles for different beta doses. Then from the variety of shining down curves, a luminescence growth curve (β induced luminescence versus added dose) was established. This was used to determine the equivalent dose (equivalent to the palaeodose). The measurement for the aliquots resulted in a variety of equivalent doses, so called dose distribution. D_e given in the report were used the arithmetic mean of the data.

In order to correct potential sensitivity changes from cycle to cycle, the luminescence response to a test dose was measured after preheat between cycles.

The blue luminescence of 8 or 12 aliquots of the sample were measured at 50^0C for 100s using a Riso TL-DA-20 reader with infrared diodes at 880nm used to deliver a stimulated beam. Blue luminescence centre about 410nm from feldspar was then detected by an EMI 9235QA photomultiplier fixed behind two filters consisting of a Schott BG39 and Kopp5-58. Beta irradiation were done on the Riso TL-DA-20
^{90}Sr/Y β irradiator, calibrated against ^{60}Co gamma source, SFU, Vancouver, Canada with about 3% uncertainty. Preheat and cut heat temperature was 260 ºC for 10 seconds.

Luminescence growth curve (β induced luminescence intensity versus added dose) was constructed by using the initial the first a few seconds of the shine down curves and subtracting the average of the last 20 seconds, along with the so called late light which was thought to be a mixture of background and hardly bleachable components. Interpolation of this growth curve to the dose axis was yielded the equivalent dose D_e which was used as a paleodose. The measurements of 8 or 12 aliquots obtained 8 or 12 D_e's, the D_e's were accepted within max recapture ratio 10%. Recycling ratio has to increase to 40%. Due to the high recycling ratio, the experiment of the recovering a given dose was tested and the value of the given dose can be recovered, so D_e is considered to be reliable. D_e used for the age determination was used for the arithmetic means of the data. A dose recovery test and a zero dose were checked no anomalies.
Fading was checked, no fading tendency was observed.

a-value a-value is measured by comparing the luminescence induced by alpha irradiation with that induced by beta or gamma irradiation. The a-value was for dose rate calculation. For this study, a- value was estimated.

Part 2: Determination of Dose Rate

Dose rate consisted of two parts.

(i) Dose rate from sample's burial environment (ii) Dose rate from cosmic rays.

(i) Dose rate from burial environment

Dose rate from sample's burial environment was determined by radionuclide contents of ^{238}U, ^{232}Th and ^{40}K, and water content.

Determination of Contents of ^{238}U, ^{232}Th and ^{40}K by the Thermo Finnigan Element 2 ICP-MS

Contents of ^{238}U, ^{232}Th and ^{40}K were measured at the Geochemical Laboratory, Victoria University of Wellington. It was assumed that these samples are homogenise and radionuclide are equilibrium. The dose rate calculation was based on the activity concentration of the nuclides ^{238}U, ^{232}Th and ^{40}K, and using dose rate conversion factors published by Guérin, G., Mercier, N., Adamiec, G. (2011).

Measurement of Water Contents

Water content was measured as weight of water divided by dry weight of the sample taking into account a 25% uncertainty.

(ii) Dose rate from cosmic rays

Dose rate from cosmic rays were determined by the depth of sample below the surface along with its longitude, latitude and altitude, convention formula and factors published by Prescott, J.R. & Hutton, J.T. (1994).

4. RESULTS

Table 1 Cosmic dose rates

Table 2 Water contents, radionuclide contents

Table 3 a- Values, equivalent doses, dose rates and luminescence ages

Table 1: Cosmic Dose Rates

Laboratory Code	Depth Below the Surface(m)	Cosmic Dose Rate (Gy/ka)	Field Code
WLL1289	0.46	0.2031±0.010	LR4
WLL1290	1.45	0.1770±0.0088	LR5

Table 2: Water Contents, Radionuclide Contents

Laboratory Code	Water Content (%)	^{238}U(ppm)	^{232}Th(ppm)	K(%)	Field Code
WLL1289	15	1.72±0.01	6.97±0.03	1.84±0.08	LR4
WLL1290	15.5	2.11±0.02	8.20±0.04	2.20±0.02	LR5

Table 3: a-Values, Equivalent Doses, Dose Rates and Luminescence Ages

Laboratory Code	a-value	D_e(Gy)	Dose Rate(Gy/ka)	**Luminescence Age(ka)**	Field Code
WLL1289	0.06±0.02	143.22±1.01	3.09±0.19	**46.4±2.9**	LR4
WLL1290	0.06±0.02	157.53±1.22	3.61±0.21	**43.6±2.6**	LR5

*a-value was estimated.

5. REFERENCES

Guérin, G., Mercier, N., Adamiec, G. 2011: Dose- rate conversion factors: update. Ancient TL, Vol.29, No.1, 5-8.

Murray, A.S. & Wintle, A.G. 2000: Luminescence dating of quartz using an improved single aliquot regenerative dose protocol. Radiation Measurements 32, 57-73.

Prescott, J.R. & Hutton, J.T. 1994: Cosmic ray contributions to dose rates for luminescence and ESR dating: Large depths and long-term time variations.
Radiation Measurements. Vol.23,Nos.2/3, 497-500.

APPENDIX F: Agisoft Drone Performance Report

Agisoft PhotoScan

Processing Report

14 May 2018

Survey Data

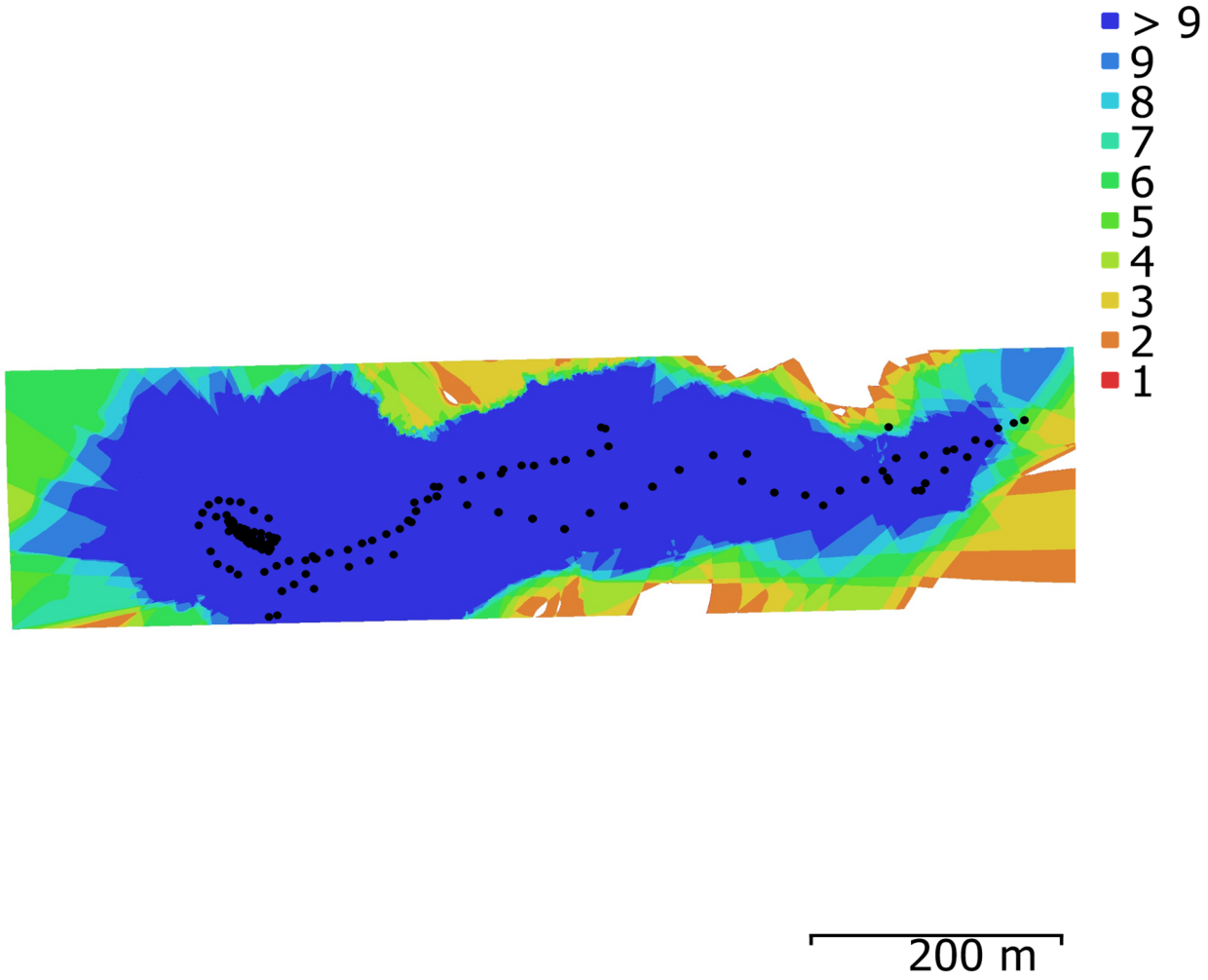

Fig. 1. Camera locations and image overlap.

Number of images:	227
Flying altitude:	51 m
Ground resolution:	1.24 cm/pix
Coverage area:	0.18 km²

Camera stations:	227
Tie points:	223,929
Projections:	792,590
Reprojection error:	0.659 pix

Camera Model	Resolution	Focal Length	Pixel Size	Precalibrated
FC6310 (8.8 mm)	5472 x 3648	8.8 mm	2.41 x 2.41 µm	No

Table 1. Cameras.

Camera Calibration

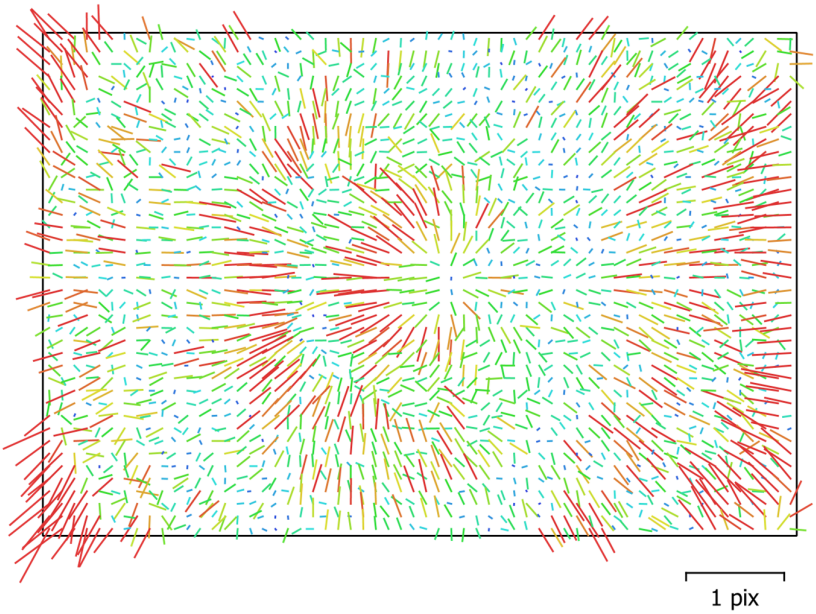

Fig. 2. Image residuals for FC6310 (8.8 mm).

FC6310 (8.8 mm)

227 images

Type	Resolution	Focal Length	Pixel Size
Frame	**5472 x 3648**	**8.8 mm**	**2.41 x 2.41 µm**

	Value	Error	F	Cx	Cy	K1	K2	K3	P1	P2
B1	**0.197066**									
B2	**-0.304461**									
F	**3648.77**	0.068	1.00	0.10	-0.74	-0.12	0.18	-0.16	0.09	-0.36
Cx	**6.45378**	0.083		1.00	-0.10	0.02	-0.00	0.00	0.96	-0.13
Cy	**10.6313**	0.08			1.00	-0.13	0.03	-0.02	-0.09	0.77
K1	**-0.00154873**	5.3e-05				1.00	-0.96	0.91	0.02	-0.13
K2	**-0.0102607**	0.00016					1.00	-0.98	-0.00	0.03
K3	**0.0110462**	0.00014						1.00	0.00	-0.03
P1	**0.0017712**	6.8e-06							1.00	-0.13
P2	**-2.06747e-05**	5.4e-06								1.00

Table 2. Calibration coefficients and correlation matrix.

Camera Locations

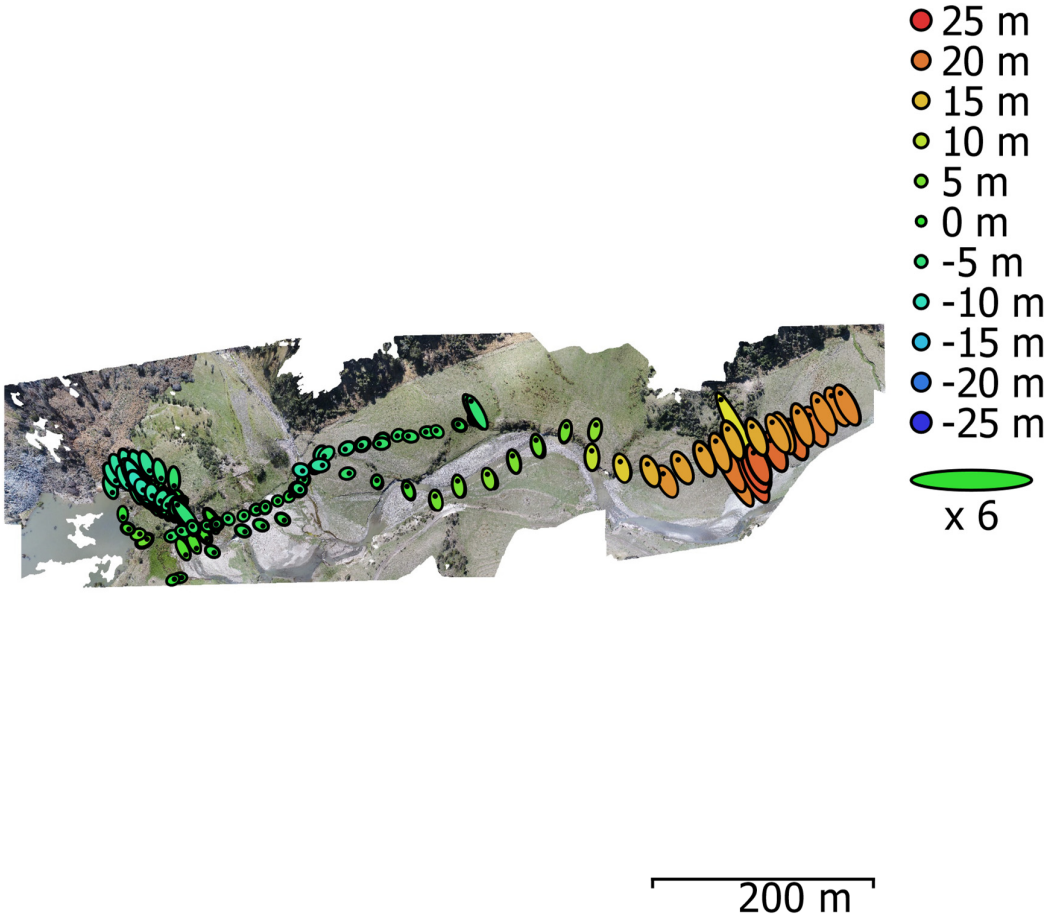

Fig. 3. Camera locations and error estimates.
Z error is represented by ellipse color. X,Y errors are represented by ellipse shape.
Estimated camera locations are marked with a black dot.

X error (m)	Y error (m)	Z error (m)	XY error (m)	Total error (m)
1.39925	2.5993	8.36985	2.95199	8.87517

Table 3. Average camera location error.
X - Easting, Y - Northing, Z - Altitude.

Camera Orientations

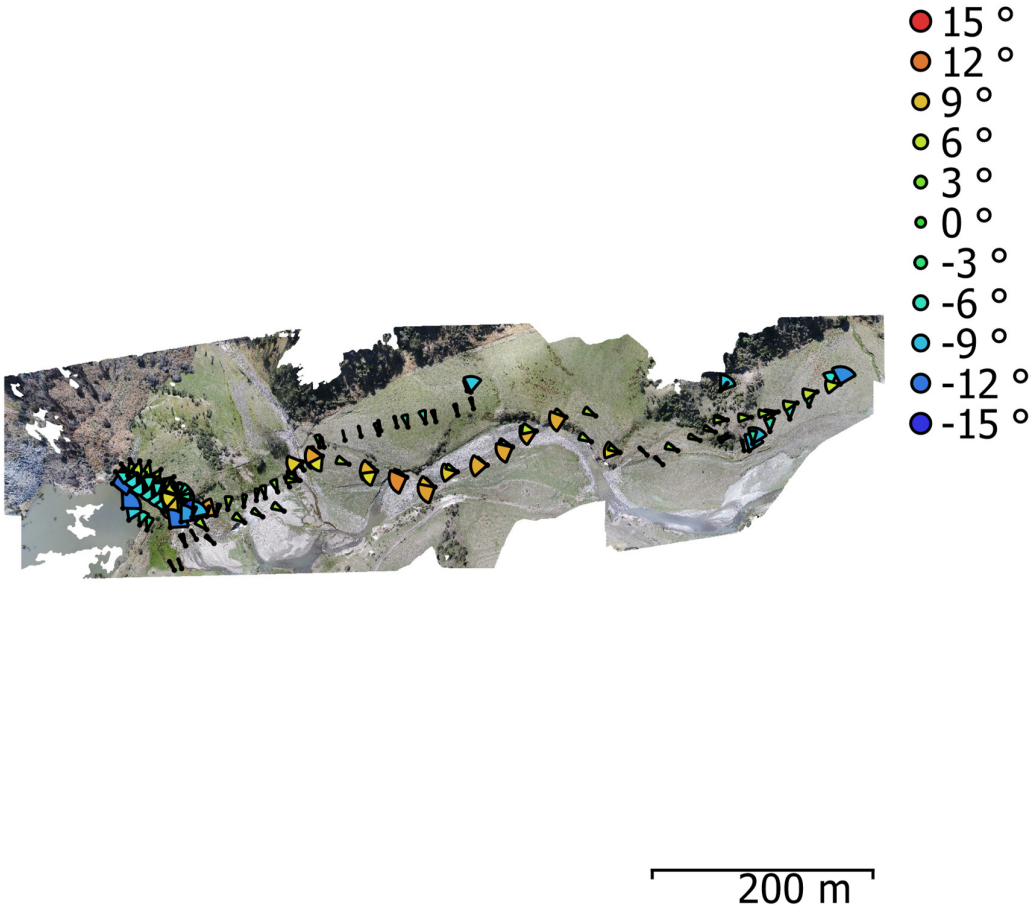

Fig. 4. Camera orientations and error estimates.
Arcs represent yaw error estimates.

Yaw error (°)	Pitch error (°)	Roll error (°)	Total error (°)
5.2625	37.5184	13.5053	40.2209

Table 4. Average camera rotation error.

Digital Elevation Model

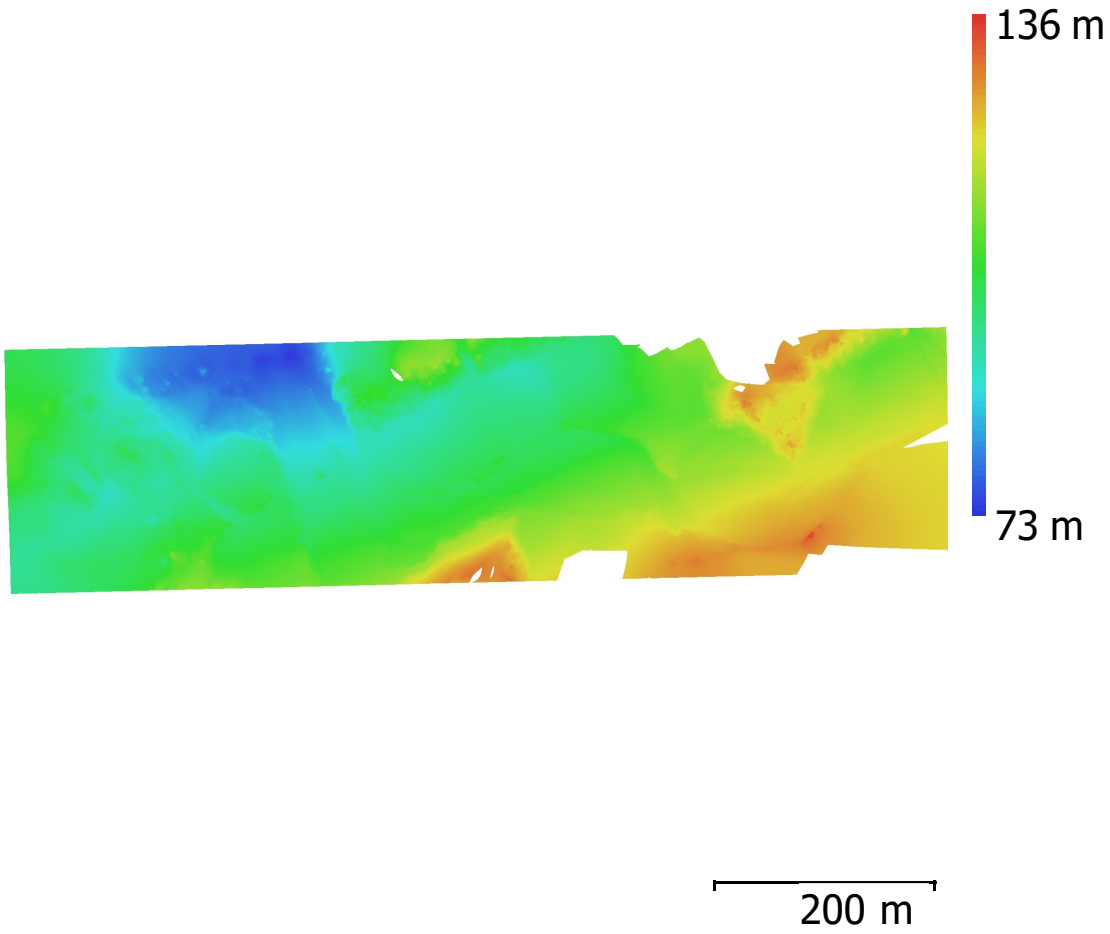

Fig. 5. Reconstructed digital elevation model.

Resolution:	4.97 cm/pix
Point density:	405 points/m²

Processing Parameters

General	
Cameras	227
Aligned cameras	227
Coordinate system	NZGD2000 / New Zealand Transverse Mercator 2000 (EPSG::2193)
Rotation angles	Yaw, Pitch, Roll
Point Cloud	
Points	223,929 of 254,704
RMS reprojection error	0.158091 (0.658737 pix)
Max reprojection error	0.573078 (33.4362 pix)
Mean key point size	3.3857 pix
Point colors	3 bands, uint8
Key points	No
Average tie point multiplicity	3.71411
Alignment parameters	
Accuracy	High
Generic preselection	Yes

Reference preselection	Yes
Key point limit	40,000
Tie point limit	4,000
Adaptive camera model fitting	Yes
Matching time	8 minutes 34 seconds
Alignment time	2 minutes 22 seconds
Optimization parameters	
Parameters	f, cx, cy, k1-k3, p1, p2
Optimization time	4 seconds
Depth Maps	
Count	227
Reconstruction parameters	
Quality	Medium
Filtering mode	Moderate
Processing time	20 minutes 30 seconds
Dense Point Cloud	
Points	39,848,532
Point colors	3 bands, uint8
Reconstruction parameters	
Quality	Medium
Depth filtering	Moderate
Depth maps generation time	20 minutes 30 seconds
Dense cloud generation time	41 minutes 35 seconds
Model	
Faces	2,649,709
Vertices	1,332,967
Vertex colors	3 bands, uint8
Texture	4,096 x 4,096, 4 bands, uint8
Reconstruction parameters	
Surface type	Arbitrary
Source data	Dense
Interpolation	Enabled
Quality	Medium
Depth filtering	Moderate
Face count	2,649,709
Processing time	48 minutes 36 seconds
Texturing parameters	
Blending mode	Mosaic
Texture size	4,096 x 4,096
Enable color correction	No
Enable hole filling	Yes
UV mapping time	8 minutes 29 seconds
Blending time	3 minutes 32 seconds
DEM	
Size	17,343 x 4,870
Coordinate system	NZGD2000 / New Zealand Transverse Mercator 2000 (EPSG::2193)
Reconstruction parameters	
Source data	Dense cloud
Interpolation	Enabled
Processing time	2 minutes 12 seconds
Orthomosaic	
Size	42,750 x 12,182
Coordinate system	WGS 84 (EPSG::4326)
Colors	3 bands, uint8
Reconstruction parameters	
Blending mode	Mosaic
Surface	Mesh

Enable color correction	No
Enable hole filling	Yes
Processing time	9 minutes 59 seconds
Software	
Version	1.4.2 build 6205
Platform	Windows 64